ABSTRACT

Title of Dissertation: FIRST PRINCIPLES COMPUTATIONAL DESIGN OF SOLID IONIC CONDUCTORS THROUGH ION SUBSTITUTION

Qiang Bai, Doctor of Philosophy, 2019

Dissertation directed by: Associate Professor Yifei Mo, Department of Materials Science and Engineering

Solid ionic conductors are key components of energy storage and conversion devices. To achieve high efficiency in these energy devices, solid ionic conductors should demonstrate high ionic or electronic conductivity. While pristine materials often suffer from poor conductivity, substituting ions in materials can tailor their electronic and ionic transport to fulfill requirements of transport properties in energy devices. In this dissertation, I applied first-principles computational techniques to elucidate the effect of ion substitution on electronic and ionic transport properties of solid materials. Therefore, three representative materials $SrCeO_3$, $La_{2-x-y}Sr_{x+y}LiH_{1-x+y}O_{3-y}$, and Li_6KTaO_6 are investigated as model systems to elucidate how ion substitution can affect the transport of electron, anion, and cation, respectively.

I studied $SrCeO_3$ as a model material to uncover the effects of B-site dopants on electronic transport. Based on theoretical calculations, I confirmed a polaron mechanism, including polaron formation and hopping, contributed to the electronic conductivity of $SrCeO_3$. I found different dopants exhibit distinct capabilities for

localizing electron polarons, and therefore result in different electronic conductivities in doped $SrCeO_3$. The study demonstrated the capabilities of first principles computation to design new materials with desired polaron formation and migration.

I studied $La_{2-x-y}Sr_{x+y}LiH_{1-x+y}O_{3-y}$ oxyhydrides as a model material to investigate H^- diffusion mechanism in a mixed anion system and its relationship with the cation substitution of Sr^{2+} to La^{3+}. I found the substitution of Sr^{2+} to La^{3+} can alter the H^- diffusion mechanism from 2D to 3D pathways. Increasing H^- vacancies through Sr^{2+} to La^{3+} substitution can also expedite the H^- conductivity of the oxyhydrides. Based on the new understanding, a number of promising dopants in Sr_2LiH_3O were predicted to enhance H^- transport.

Fast Li-ion conductor materials as solid electrolytes are crucial for the development of all-solid-state Li-ion batteries. I systematically studied Li^+ diffusion mechanisms in Li_6KTaO_6 predicted by our computational study. I found that different carrier defects such as Li vacancies or interstitials can induce distinct Li^+ transport mechanisms. In addition, I developed a computational workflow to predict a wide range of materials in a prototype structure. By employing the workflow, I computationally predicted a group of Li superionic conductors with good stabilities by substituting the Li_6KTaO_6 structure.

FIRST PRINCIPLES COMPUTATIONAL DESIGN OF SOLID IONIC CONDUCTORS THROUGH ION SUBSTITUTION

by

Qiang Bai

Dissertation submitted to the Faculty of the Graduate School of the
University of Maryland, College Park, in partial fulfillment
of the requirements for the degree of
Doctor of Philosophy
2019

Advisory Committee:
Professor Yifei Mo, Chair
Professor Liangbing Hu
Professor Lourdes G. Salamanca-Riba
Professor Peter W. Chung
Professor Chunsheng Wang, Dean's representative

Acknowledgements

First, I would like to thank my advisor, Dr. Yifei Mo, for his great guidance and comprehensive support through my graduate study. In the last four years, he gave me lots of guidance on research areas and I am deeply impressed by his insightful vision. The four-year study advised by him constitutes the valuable period of my life.

I would also like to thank my committee members, i.e., Dr. Liangbing Hu, Dr. Chunsheng Wang, Dr. Peter W. Chung and Dr. Lourdes G. Salamanca-Riba. They contributed lots of valuable suggestions on this dissertation.

I want to thank my lab mates, especially Dr. Xingfeng He and Dr. Yizhou Zhu. I appreciate the help from other group members, i.e., Yunsheng Liu, Adelaide MeiChun Nolan, Md Shafiqul, Shuo Wang and Dr. Menghao Yang. I wish you all the best in the future.

I want to thank my friends to support my study, e.g., Mr. Hao Meng, Ms. Siyue Wu, Ms. Zhuo Chen, Dr. Yubing Zhou, Dr. Jian Gao, Mr. Zhe Luo, Ms. Jingyun Yang, Dr. Yi-Jiun Lin, Mr. George Thomas, and Mr. Tianhang Xu. I want to express my special thanks to Mr. Wenhao Ye for the pleasure he gave me. It is my pleasure to have you as my friends.

Finally and most importantly, I want to thank my parents, my grandparents, my uncle, my aunt and other relatives for their unconditional love and support. It is my honor to have your support.

To be honest, pursing Ph.D. may be the most regrettable decision in my life till now. I deeply understand that getting a Ph.D. offer does not necessarily mean a happy ending but another challenging journey, just like professing your love/ propose

to her. Sometimes, I felt it is Ph.D. students' privilege to complain about their ultra-high pressure and workload. However, I changed my mind especially when I visited Chinese Internet giants such as ByteDance, Tencent and etc. Even though I truly disagree the spirit of work-life balance in those Chinese companies, I appreciate people who work hard to change their lives. I hope I am lucky enough to avoid that type of style, and enjoy my energetic, happy and unique life.

Table of Contents

Acknowledgements ii
Table of Contents iv
Chapter 1: Introduction 1
1.1. Electrical transport properties in solid ion conductors 1
1.2. Effect of cation dopants on electronic transport in MIECs 3
1.3. Effect of cation substitution on anion conduction 5
1.3. Effect of dopants on cation conduction 7
1.4. Dissertation overview 9
Chapter 2: Computational Methods 11
2.1. Density functional theory (DFT) calculations 11
2.2. Phase stabilities of materials 11
2.3. Ion migration pathway and energy barrier 12
2.4. Molecular dynamics simulations 13
Chapter 3: Effect of cation dopants on electronic transport in $SrCeO_3$ perovskite 16
3.1. Introduction 16
3.2. Methods 19
3.3. Results 23
3.4. Discussion 43
3.5. Conclusions 46
Chapter 4: Effect of cation substitution on hydride-ion transport in the new oxyhydrides 47
4.1. Introduction 47
4.2. Methods 50
4.3. Results 54
4.4. Discussion 68
4.5. Conclusions 70
Chapter 5: Effect of carrier defects on Li-ion diffusion in Li_6KTaO_6 71
5.1. Introduction 71
5.2. Methods 74
5.3. Results 76
5.4. Discussion 89
5.5. Conclusions 91
Chapter 6: Conclusions and Future Work 93
6.1. Conclusions 93
6.2. Future work 94
Publications, Patents, and Presentations 96
Publications 96
Patents in Application 97
Presentations 98
Appendices 100
Appendix A 100
Appendix B 106
Appendix C 115
Bibliography 119

Chapter 1: Introduction*

1.1. Electrical transport properties in solid ion conductors

Increased reliance on intermittent renewable energy sources needs reliable energy conversion and storage technologies.[1, 2] Solid ion conductors are important components in energy conversion and storage devices, such as fuel cells, lithium ion batteries (LIBs), and gas sensors.[3-5] Electrical properties, such as electronic and ionic conductivity, of solid ion conductors can influence the performance of energy devices. For example, solid electrolytes in fuel cells should demonstrate facile ionic conduction to reduce internal resistance. Electrode materials in LIBs need both high electronic and ionic conductivity to achieve high power rate and energy efficiency. Thus, it is of great scientific interest to design and discover novel materials with promising electrical properties.

Solid ion conductors can be classified into electronic conductors, ionic conductors, and mixed ionic and electronic conductors (MIECs) based on the conducting species.[3, 6] Pristine solid ion conductors without dopants often suffer from low electronic conductivities or ionic conductivities, which cannot satisfy the requirements of electrochemical devices.[4, 7] Therefore, modifying materials for improved conducting properties is critical for their applications. Chemical substitution of materials can effectively improve their electronic or ionic conductivities.[8, 9] For example, the electronic conductivity of undoped $SrCeO_3$ as 0.3

---

* Some text of introduction is adapted from my published papers:
Q. Bai, Y. Zhu, X. He, E. Wachsman, Y. Mo, First Principles Hybrid Functional Study of Small Polarons in Doped $SrCeO_3$ Perovskite: Towards Computational Design of Materials with Tailored Polaron, ***Ionics*** 24 (2018) (4) 1139.
Q. Bai, X. He. Y. Zhu, Y. Mo, "First-Principles Study of Oxyhydride H^- Ion Conductors: Towards Facile Anion Conduction in Oxide-Based Materials", ***ACS Applied Energy Materials*** 1 (2018) (4) 1626.

mS/cm at 1073 K can be increased to 8 mS/cm due to doping Yb at Ce sites.[10] Tuning composition of Li_3OCl to $Li_3OCl_{0.75}Br_{0.25}$ can improve Li^+ conductivity from 0.005 to 0.4 mS/cm.[11, 12] Thus, to aid the design of better solid ion conductors, it is important to understand the effects of ion substitution on electronic and ionic transport in solid materials.

The effects of dopants on electronic conducting properties have been studied for a long time.[13] Small concentrations of extrinsic dopants (e.g., N or P) in Si can tremendously change its electronic property to be n- or p-type semiconductors.[14] Such enhancements can be explained by electronic carriers created upon doping. Dopants effects on electronic conductivity have different mechanisms in other materials, and are still being explored. For example, while introducing some dopants such as Eu and Yb at Ce sites in $SrCeO_3$ can enhance its electronic conductivity, other dopants such as Gd or Sc fail to improve the electronic transport.[10, 15] It is not fully understood that why certain dopants have better capability to enhance the electronic conductivity. Since increasing electronic conductivity of solid ion conductor materials is desired for many applications, e.g., electrodes in batteries or permeation membranes for gas separation, the lack of understanding impedes the discovery of new dopants for further improving these materials. The computational capability to identify and predict the effect of dopants on electronic conduction in solids is important.

In addition to electronic conductivity, ion substitution can influence ionic transport in materials.[2, 4, 16, 17] For example, without the incorporation of Y to create more O vacancies, ZrO_2 has low O^{2-} conductivity and cannot serve as a solid

electrolyte in fuel cells.[18] Doping Zr at Ta sites in $LiTaSiO_5$ can result in a high Li^+ conductivity of 6.3 mS/cm at 300 K, while the original $LiTaSiO_5$ has a limited conductivity of 7.6×10^{-7} mS/cm at 300 K.[19] Since high ionic conductivity is required for solid electrolytes (SEs) in batteries or fuel cells, investigating the effects of ion substitution on anion and cation diffusion is important for the development of energy storage and conversion devices.

First principles atomistic modeling can provide a unique understanding of the effect of ion substitution on electronic and ionic transport of solid conductors. The detailed analyses at the electronic and atomic scale are difficult to directly characterize in experiments. The understanding of dopants effects on electrical properties of solids can further guide the optimization of materials. In this dissertation, I will use computational modeling to investigate electronic, anion or cation transport mechanism in three representative materials, i.e., $SrCeO_3$, $La_{2-x-y}Sr_{x+y}LiH_{1-x+y}O_{3-y}$ and Li_6KTaO_6, under ion substitution. Based on this new understanding, I will also design new materials with promising properties using first principles computational techniques.

1.2. Effect of cation dopants on electronic transport in MIECs

The Paris Agreement[20] strongly motivates the transition from carbon intensive fossil fuels to a clean hydrogen economy. H_2 separation technology, which enables pure H_2 to be acquired from mixed gases, is an essential component of the hydrogen economy. Electrochemical ceramic membranes based on cerates, titanates, and zirconates are regarded as promising components for H_2 separation (Fig. 1.1).[6,

[21] The separation membranes should be MEICs, meaning that they should allow the simultaneous transport of protons and electrons.[7] The H_2 permeation rate (J_{H_2}) can be described by the Wagner equation[22] as:

$$J_{\mathrm{H2}} \propto \frac{\sigma_H \times \sigma_e}{\sigma_H + \sigma_e} \qquad \text{Eq. 1}$$

where σ_H and σ_e refer to the proton and electronic conductivity respectively. Thus, to have a high H_2 permeation rate, a material needs high protonic and electronic conductivities.

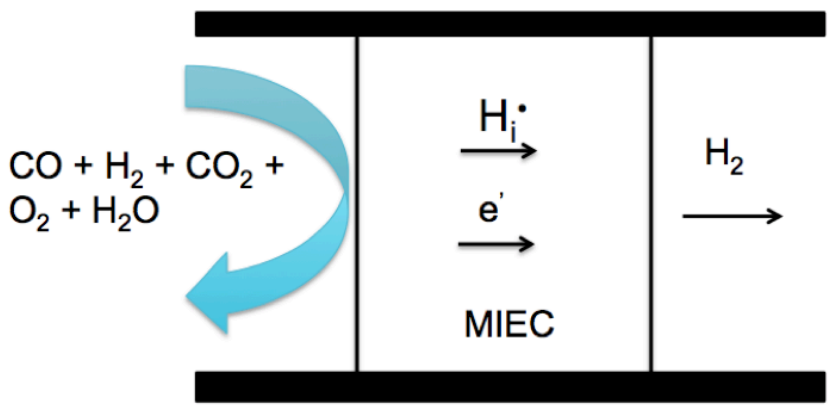

Figure 1.1. Schematic of H_2 separation using MIECs as membranes, where pure H_2 can be acquired from the mixed gas.

$SrCeO_3$, which has a perovskite structure, has been proposed as a promising candidate membrane material.[22, 23] While undoped $SrCeO_3$ exhibits low proton and electronic conductivities, $SrCeO_3$ doped with aliovalent dopants (e.g., Gd, Y, Sc, Eu and Yb) at Ce sites demonstrated high protonic conductivity in experiments.[24-29] However, enhanced electronic conductivity can only be achieved in $SrCeO_3$ doped

with certain dopants (i.e., Eu and Yb).[24, 29] The enhanced electronic transport in $SrCeO_3$ has often been attributed to the charge transfer among B-site cations.[10] For example, the charge that can transfer among multivalent cations (e.g., $Ce^{4+/3+}$ or $Eu^{3+/2+}$) would contribute to the electronic conductivity, which corresponds to the polaron formation and hopping mechanism. A polaron is a quasiparticle formed by localized excess charge, such as electrons or holes, and its local lattice deformation.[30, 31] A polaron can transfer within the lattice with the transference of local lattice distortion, contributing to the electronic conductivity.[32]

However, there is limited experimental or theoretical evidence to support the polaron mechanism in $SrCeO_3$ to enhance the electronic conductivity. The role of dopants on polaron formation and migration are still to be explored. Thus, it is of great scientific interest to understand why certain dopants have better capabilities to increase electronic conductivities than others. Based on the understanding, we can select dopants to more efficiently tailor the electronic transport of materials. The study of dopants effects on electronic conductivities in $SrCeO_3$ can provide insight for the design of electrode materials in batteries and fuel cells.

1.3. Effect of cation substitution on anion conduction

In addition to good electronic transport, materials in energy storage and conversion devices should exhibit excellent ionic conduction. For example, fast anion conductors (e.g., O^{2-}, F^-, H^-) play an important role in electrochemical applications, such as solid-state batteries and fuel cells.[5, 33, 34] Hydride ions (H^-) are attractive charge carriers with a low standard redox potential of H_2/H^- (-2.2 eV), indicating high

voltage and energy densities.[35] In contrast to protons (H^+), H^- are exceedingly rare and only exist in few compounds such as metal hydrides (e.g., BaH_2 and CaH_2) and some oxyhydrides (e.g., $LaSrCoO_2H_{0.7}$, $12CaO\bullet7Al_2O_3$ and $BaTiO_{3-x}H_x$).[36-39] Recently, the conduction of H^- in a new $La_{2-x-y}Sr_{x+y}LiH_{1-x+y}O_{3-y}$ oxyhydride has been realized in experiments. $La_{2-x-y}Sr_{x+y}LiH_{1-x+y}O_{3-y}$ exhibited a high H^- conductivity of 0.12 mS/cm at 573 K in experiments, which is comparable with other protonic and oxygen conductors.[5, 40] The new oxyhydride has been successfully used as an electrolyte in the all-solid-state cell with an open circuit voltage of 0.28 V.[5, 40] The discovery of the oxyhydride opens a promising avenue for exploring efficient electrochemical solid devices based on H^- conduction.

It has been reported that the H^- conductivity increases when Sr^{2+} substitutes La^{3+} from La_2LiHO_3 (y = 0), $LaSrLiH_2O_2$ (y = 1) to Sr_2LiH_3O (y = 2).[5] In addition, increasing H^- vacancies x in anion sublattice by the substitution of Sr^{2+} to La^{3+} can improve conductivities of the oxyhydrides, as $La_{0.6}Sr_{1.4}LiH_{1.6}O_2$ exhibits the highest conductivity.[5] These experimental observations strongly indicate the H^- diffusion mechanism is highly dependent on cation substitution. An in-depth understanding of the effect of cation substitution on anion conduction can facilitate the discovery of new anion conductors.

1.3. Effect of dopants on cation conduction

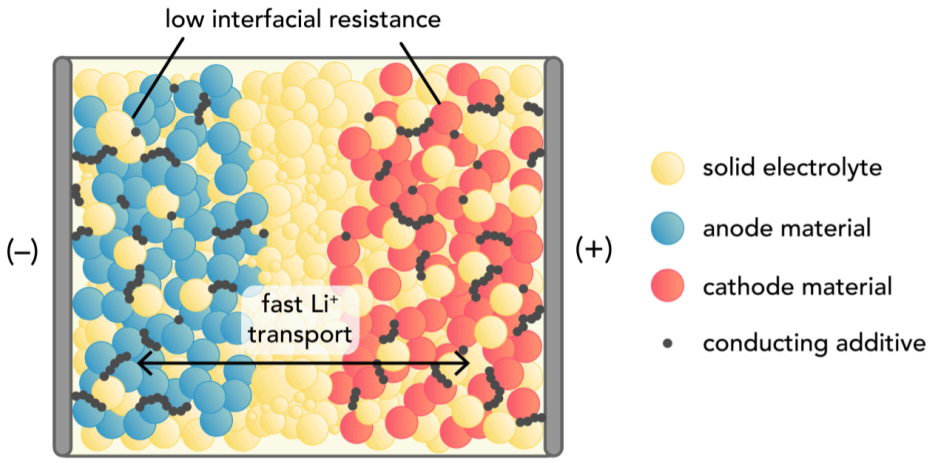

Figure 1.2. Schematic picture of all-solid-state Li-ion batteries (ASLIBs) using solid electrolytes (SEs) with high Li^+ conductivity. Reproduced with permission.[41] Copyright 2018 Elsevier.

In addition to fast anion conductors, materials that demonstrate facile cation diffusion such as Li^+, Na^+ and Mg^{2+} are important components in energy conversion systems.[2, 42, 43] In particular, exhibiting high Li^+ conductivity is important for a solid-state material as an electrolyte in all-solid-state Li-ion batteries (ASLIBs).[44] ASLIB with solid electrolytes (SEs) may replace current Li-ion batteries (LIBs) using organic liquid electrolytes (Fig. 1.2), because ASLIBs outperform organic LIBs with enhanced thermal stability, wide operating temperature range, improved packing efficiency and potential high energy density with Li metal as anodes.[19, 45] SEs are crucial components in ASLIBs and must satisfy multiple essential requirements to be

used in energy conversion systems, e.g., high Li^+ conductivity, excellent electrochemical stability and good mechanical strength. Thanks to the previous research on Li SEs, significant progress has been achieved by identifying several Li superionic conductors (SICs) with excellent room temperature (RT) conductivities (σ_{Li+} > 0.1 mS/cm), including garnet $Li_7La_3Zr_2O_{12}$ (LLZO), NASICON $Li_{1.3}Al_{0.4}Ti_{1.7}(PO_4)_3$ (LATP), $Li_{10}GeP_2S_{12}$ (LGPS).[45-49] Despite these advances, some of them suffer from various limitations such as poor stability and high costing during the processing.[41, 50, 51] Those issues highlight the critical need to design and search for new Li SICs exhibiting excellent properties.

While some SICs can achieve high Li^+ conductivity as pristine compositions, e.g., $Li_7P_3S_{11}$,[52] Li_3YCl_6 and Li_3YBr_6,[53] superionic conduction in many materials should be activated by aliovalent doping to introduce extrinsic carrier defects, i.e., Li^+ vacancies or interstitials. For example, $Li_{1.9}Cd_{1.05}Cl_4$ with Li^+ vacancies by Cd^{2+} substitution demonstrated a higher conductivity of 10 mS/cm at 473 K than that of 5 mS/cm for perfect Li_2CdCl_4.[54] In addition to vacancies, introducing interstitials in $LiTaSiO_5$ through Zr^{4+} doping can boost the conductivity from 7.6×10^{-7} mS/cm at 300 K to 6.3 mS/cm.[19] Thus, extrinsic carrier defects introduced by aliovalent doping plays an important role in enhancing Li^+ conductivity.

It is noted that the introduction of vacancies or interstitials has different effects for different materials. For example, $Li_{1.7}Zn_{0.65}PS_4$ with lithium interstitials in $LiZnPS_4$ exhibited an ionic conductivity of 0.13 mS/cm at room temperature (RT) in experiments, which was four orders of magnitude higher than that of $LiZnPS_4$ with vacancies.[55] In contrast to $LiZnPS_4$, $Li_{2.9}OCl_{0.9}$ with vacancies in Li_3OCl_3 exhibited

the higher conductivity of 0.85 mS/cm than that of 2×10^{-4} mS/cm of $Li_{3.1}O_{1.1}Cl_{0.9}$ with interstitials at RT.[12] Given the different effects of vacancies and interstitials on conductivities in different materials, it is necessary to understand why certain extrinsic carrier defects can activate superionic conduction in materials by aliovalent doping. In this dissertation, I will use Li_6KTaO_6 as a prototype material to uncover the Li^+ transport mechanism as a function of different carrier defects.

1.4. Dissertation overview

The dissertation consists of six chapters.

Chapter 1 gives an introduction about the effect of ion substation on electronic and ionic transport in solid conductors. Therefore, the representative materials $SrCeO_3$, $La_{2-x-y}Sr_{x+y}LiH_{1-x+y}O_{3-y}$, and Li_6KTaO_6 and their ion substitution effects on electronic, anion, and cation transport, respectively are briefly introduced.

Chapter 2 briefly introduces the computational methods used in this dissertation. Part of this chapter was published in ***Advanced Energy Materials***.[2]

Chapter 3 presents the distinctive behaviors of different dopants in localizing polarons to increase electronic conductivity. In addition, new promising dopants are predicted to further increase electronic conductivity. This chapter was published in ***Ionics***.[7]

Chapter 4 presents the effect of cation substation on H^- transport in the oxyhydrides $La_{2-x-y}Sr_{x+y}LiH_{1-x+y}O_{3-y}$. Upon Sr^{2+} substituting La^{3+}, H^- diffusion exhibits a transition from two-dimensional (2D) to 3D transport, as the composition changes from $LaSrLiH_2O_2$ to Sr_2LiH_3O. In addition, new promising dopants were predicted to

increase H^- conductivity in Sr_2LiH_3O by creating more H^- vacancies. This chapter was published in ***ACS Applied Energy Materials***.[4]

Chapter 5 presents different Li^+ transport mechanism induced by different cation substitution (i.e., Ba^{2+} and Zr^{4+}) and extrinsic carrier defects (i.e., V_{Li} and Li_i) in Li_6KTaO_6. Li_6KTaO_6 were demonstrated as a promising SE in ASLIBs with excellent electrochemical stabilities and high Li^+ conductivity after Zr^{4+}.

Chapter 6 presents the main conclusions of the dissertation and potential future research related to the dissertation.

Chapter 2: Computational Methods†

2.1. Density functional theory (DFT) calculations

All DFT calculations in this dissertation were performed within the projector augmented-wave (PAW)[56] using the Vienna *Ab initio* Simulation Package (VASP).[57] The Perdew-Burke-Ernzerhof (PBE) generalized-gradient approximation (GGA) functional was used to calculate total energies of materials.[58] We adopted the convergence parameters from the *Materials Project*[59] in the spin-polarized static DFT calculations, which guarantee the total energies converged to 1 meV per atom. Because the GGA-PBE functional tends to underestimate band gaps of materials, the screened hybrid Heyd-Scuseria-Ernzerhof (HSE06)[60, 61] were used to calculate band gaps of solid materials. We calculated phonon dispersion of materials using a finite displacement approach implemented in Phonopy code[62] with the PBEsol functional.[63]

2.2. Phase stabilities of materials

We constructed compositional phase diagrams to evaluate phase stabilities of materials.[41, 64] We constructed the convex hull from total energies of all compounds, which belong to compositional space of the investigated phase (Fig. 2.1). Then, the phase equilibria and corresponding decomposition energies of the investigated phase can be decided from the phase diagram. The energy above the hull (ΔE) is the absolute value of the decomposition energies. A compound with $\Delta E = 0$ is

---

† Part of this chapter has been published in
Q. Bai, L. Yang, H. Chen, Y. Mo, "Computational Studies of Electrode Materials in Sodium-Ion Batteries", ***Advanced Energy Materials*** 8 (2018) (17) 1702998.

thermodynamically stable. Materials with large ΔE suffer from a strong driving force to decompose and are likely to be difficult to synthesize.

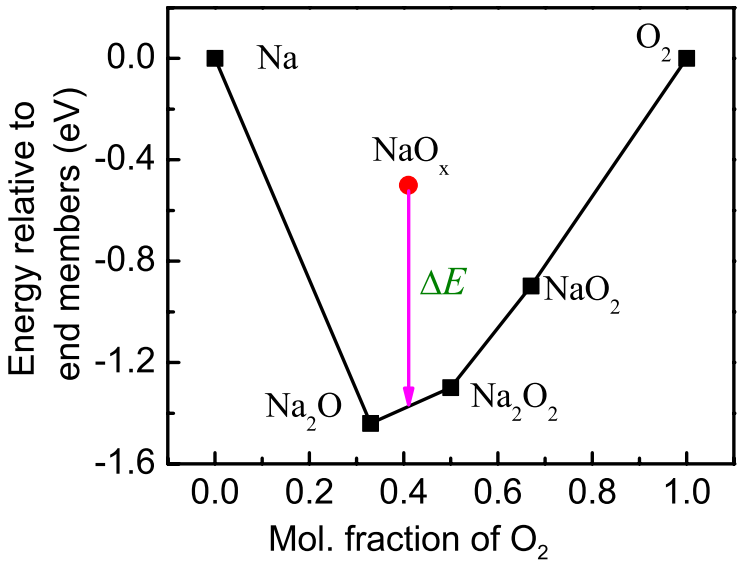

Figure 2.1. Schematic convex hull in Na-O_2 system. The phase equilibria and ΔE of NaO_x can be obtained from the convex hull.

2.3. Ion migration pathway and energy barrier

In this dissertation, we used the nudged elastic band (NEB) method[65, 66] to study atomistic diffusion mechanisms. NEB calculations are performed on a particular ion-migration pathway from the initial to the final equilibrium site. NEB calculations require initial guesses of these atomistic migration mechanisms as input. Based on the initial guesses of the migration mechanism, NEB calculations can identify the lowest-energy migration pathway, the energy profile along the pathway, the transition state, and the migration energy barrier. The climbing-image NEB method[67] (CI-NEB) incorporates a modification of NEB method to obtain the

highest image at the saddle point and thus obtain a more accurate estimation of transition state and migration energy barrier. The construction of NEB calculations may be difficult for studying the complex diffusion mechanism in many materials. While one can construct NEB calculations for all possible ion diffusion pathways, it is difficult to guess a priori whether a diffusion mode would actually happen and which diffusion mode is dominant. For studying materials with complex diffusion mechanisms, NEB calculations are greatly complemented by MD simulations.

2.4. Molecular dynamics simulations

Molecular dynamics (MD) simulations[17, 66] model the real-time Newtonian dynamics of all atoms in the materials, and thus fully capture the diffusion of ions. By tracking the real-time trajectories and displacements of ions in MD simulations, the rate of diffusion over time can be quantified by the mean square displacement

$$< [\Delta r(t)]^2 >= \frac{1}{N}\sum_i < [r_i(t+t_0) - r_i(t_0)]^2 >, \qquad \text{Eq. 2}$$

where N is the total number of mobile ions and $r_i(t)$ corresponds to the displacement of the i-th mobile ion at the time t. The arrow bracket represents the average over different starting time t_0. The self diffusivity D^* of mobile ions can be obtained as [66, 68]

$$D^* = \frac{1}{2dt} < [\Delta r(t)]^2 >, \qquad \text{Eq. 3}$$

where d is the dimension of the lattice for diffusion. The ionic conductivity σ is estimated based on the Nernst-Einstein equation[17, 66]:

$$\sigma = \frac{Ne^2}{V\,k_{\mathrm{B}}T} D, \qquad \text{Eq. 4}$$

where N is the total number of mobile ions, V is the volume of the simulation cell, e is the Na-ion charge, and T is the temperature. In a material where the hopping of different ions is independent from each other, the self-diffusion diffusivity D^* obtained from MD simulations can be used to evaluate the ionic conductivity. Otherwise, the correlation factor of ion diffusion should be considered.[17, 69]

In addition, MD simulations are performed at multiple temperatures to obtain the diffusivities and ionic conductivities at multiple temperatures, similar to experimental measurements. If the same diffusion mechanism holds over the temperature range, the diffusivity follows the Arrhenius relation:

$$D(T) = D_0 e^{-\frac{E_a}{k_B T}}, \qquad \text{Eq. 5}$$

where E_a is the activation energy. In MD simulations, the activation energy for the overall ion transport is obtained by fitting to Arrhenius relation. In addition, the diffusivity and corresponding conductivity at other temperatures can be estimated by extrapolating Arrhenius relation.

NEB calculations and MD simulations can be performed using either DFT methods[70, 71] or classical potentials (also known as force fields).[72, 73] NEB calculations are mostly performed using DFT methods, which provide more reliable potential energy surface and more accurate migration energy barrier.[70, 71, 74] While MD simulations were traditionally performed using classical potentials,[72] *ab initio* MD (AIMD) simulations based on DFT to calculate the interatomic interactions have recently gained great successes in quantifying diffusional properties and in identifying diffusion mechanisms.[70, 75, 76] However, given the significantly higher computational cost of AIMD simulations than classical MD simulations, AIMD

simulations are often limited to a small system size of a few hundred atoms and a short time scale (~10-100 ps).[66] As a result, AIMD simulations have to be performed at elevated temperatures (usually > 600 K) and can only be performed on materials with high ionic conductivity. AIMD simulation and NEB calculation are highly complementary for studying diffusional properties as shown in this dissertation.

Chapter 3: Effect of cation dopants on electronic transport in $SrCeO_3$ perovskite[‡]

3.1. Introduction

The grand challenge of climate change motivates the transition from carbon-intensive fossil fuel to hydrogen fuel as a zero-emission, abundant energy source [77]. The technology of H_2 separation is essential for the production, storage, and utilization of hydrogen fuel, such as in hydrogen fuel cells [78, 79], hydrogen sensors [80], and membrane reactors for natural gas conversion [81, 82]. Electrochemical ceramic membrane is a promising technology for H_2 separation [83, 84]. These ceramic membrane materials based on cerate, titanate and zirconate perovskites can achieve high protonic conductivity and high hydrogen permeability [83, 85, 86]. Doped $SrCeO_3$ perovskite materials have been demonstrated as promising materials for H_2 separation membranes with negligible oxygen permeability [27-29]. In particular, Eu- and Yb-doped $SrCeO_3$ achieves a high overall H_2 flux [28, 87].

The outstanding H_2 separation performance of $SrCeO_3$ perovskite materials are achieved by designing the materials with various dopants, which tailor defect equilibria, protonic conductivity, and electronic transport. Doping aliovalent acceptors, such as Gd [85], Y [88], and Sc [85, 89] at B sites, has been used to increase oxygen vacancy concentration and to facilitate proton incorporation, giving rise to

---

[‡] This chapter has been published in
Q. Bai, Y. Zhu, X. He, E. Wachsman, Y. Mo, "First Principles Hybrid Functional Study of Small Polarons in Doped $SrCeO_3$ Perovskite: Towards Computational Design of Materials with Tailored Polaron", ***Ionics*** 24 (2018) (4) 1139.

higher protonic conductivity. In addition, high H_2 flux requires simultaneous transport of protons and electrons [26, 90]. While high protonic conductivity can be achieved in $SrCeO_3$ with various accepter dopants, low electronic conductivity often limits overall H_2 flux for hydrogen separation [24, 27, 87]. To enhance electronic conductivity in $SrCeO_3$ for high H_2 flux, multivalent dopants, such as Eu [26, 28, 29] and Yb [24, 27, 87, 91], were investigated. Eu- and Yb-doped $SrCeO_3$ exhibited higher electronic conductivities and H_2 permeation rates than those of pure and other doped $SrCeO_3$ [24-26, 87, 89, 92].

$SrCeO_3$ is a wide band gap material, and the electronic conductivity in doped $SrCeO_3$ is often attributed to the charge transfer among B-site cations. For example, the charge transfer among $Ce^{4+/3+}$ and other multivalent dopants such as $Yb^{3+/2+}$ may contribute to the electronic transport [24]. The mechanism of polaron formation and hopping was also proposed to explain the high electronic conductivity of $SrCeO_3$ doped by Eu, which has two oxidation states +2 and +3 [26, 28, 29, 92]. Recently, Swift *et al.* performed first principles hybrid functional calculations in $SrCeO_3$ and confirmed the existence of electron polarons on Ce sites [16]. However, it is still not clear why certain dopants have better capabilities to increase electronic conductivity than other dopants in $SrCeO_3$. Direct experimental characterization and theoretical computation of polarons in these materials are limited, and the role of dopants in the formation and migration of the small polarons is still not clear. A direct comparison between the polaron formation and energetics of different doped materials is needed. The lack of understanding about dopant effects on polarons limits further design and development of hydrogen membrane materials. To understand the effects of dopants on increasing

electronic conductivity, we performed a systematic theoretical investigation on the formation and migration of polarons in these doped materials to reveal polaron mechanism under different doping.

In addition, there is urgent need of computational methods and theoretical understanding for guiding materials doping to tailor functional properties. Designing materials through doping to enhance electronic conductivity is of great interest in the development of electrode materials for batteries and fuel cells [32, 93]. However, selecting performance-enhancing dopants for materials design has been largely based on human intuition, empirical data, and trial-and-error experiments. Few design principles exist to guide such materials design. As motivated by the Materials Genome Initiative [94] to develop new materials faster, first principles computation techniques have been demonstrated in designing and predicting novel materials with new doping and compositions to achieve improved ionic conductivity, stability, and other properties [95-99]. To the best of our knowledge, the computation techniques for designing doped materials with different polaronic behavior are to be developed.

In this chapter, we performed first principles hybrid functional calculations to study polaron formation and migration in $SrCeO_3$ with various dopants. We considered B-site dopants, such as Gd, Y, Sc, Yb, and Eu, which were reported in previous experiments of doped $SrCeO_3$ [85, 92]. These dopants with +3 valence states and similar ionic radii as the host Ce^{4+} cation were used to substitute Ce^{4+} and to incorporate O vacancies into $SrCeO_3$ [85, 92]. The reported increased electronic conductivity of some dopants such as Eu and Yb compared to others were largely attributed to their multivalence nature and the charge transfer among them [26, 87]. We

also considered new dopants exhibiting multivalence in prior experiments [100-103], such as Pr, Nd, and Cr, to explore their potential capabilities to form polaron and to enhance electronic conductivity. These dopants may also be potential B-site dopants and were reported in prior experiments [100-103] to have multivalence, which may potentially increase electronic conductivity. Our theoretical calculations demonstrated and confirmed the existence of polarons on certain dopants and supported the polaron hopping mechanism in enhancing electronic conductivity from previous experiments [24]. Using $SrCeO_3$ as an example, our study demonstrated first principles computation techniques in studying dopant effects on polaron formation and migration in materials. Our computation scheme is generally applicable to design new materials with tailored polaron formation and with enhanced functional properties.

3.2. Methods

3.2.1. First principles computation

All density functional theory (DFT) calculations were performed within the projector augmented-wave approach (PAW) [56] using the Vienna *Ab initio* Simulation Package (VASP) [57]. The chosen PAW potentials treat the following electrons of elements as valence electrons, i.e., Ce: $5s^2 5p^6 4f^1 5d^1 6s^2$, O: $2s^2 2p^4$, Sr: $4s^2 4p^6 5s^2$, Gd: $5s^2 5p^6 4f^7 5d^1 6s^2$, Y: $4s^2 4p^6 4d^1 5s^2$, Sc: $3s^2 3p^6 3d^1 4s^2$, Eu: $5s^2 5p^6 4f^7 6s^2$, Yb: $5s^2 5p^6 4f^{14} 6s^2$, Pr: $5s^2 5p^6 4f^3 6s^2$, Nd: $5s^2 5p^6 4f^4 6s^2$ and Cr: $3p^6 3d^5 4s^1$. All calculations were first performed using the Perdew–Burke–Ernzerhof (PBE) functional [58] within the generalized-gradient approximation (GGA) and then using the screened hybrid Heyd-Scuseria-Ernzerhof (HSE06) functional [60, 104]. The GGA-PBE functional tends

to over delocalize electrons and underestimate band gap [105]. The hybrid functional, which mixes a fraction of nonlocal Hartree-Fock exchange, has been demonstrated to provide more accurate energies and band gaps of solid materials [106-108]. In particular, the hybrid functional has been successfully used to describe polaron formation in many oxides, such as Li_2O_2 [30], $LiMnPO_4$ [109] and $BaCeO_3$ [110], where the GGA functional may unphysically delocalize the electron. Therefore, we choose HSE06 hybrid functional for the $SrCeO_3$ material system in this study. We adopted standard parameters [61], such as the mixture fraction α = 0.25 of the exact Hartree-Fock exchange with GGA and the screened parameter ω = 0.2 $Å^{-1}$. Different mixing fraction α = 0.40 was also tested for polaron formation and migration in this study and no qualitative difference in the results was observed unless specifically noted. The calculations for pure and doped $SrCeO_3$ were based on supercells with 2×2×1 unit cells with 16 formula units of $SrCeO_3$. The computation parameters were consistent with the Materials Project [59]. We used a plane-wave cutoff of 520 eV for all calculations to achieve the energy convergence to 1 meV per atom. A single gamma point was used for HSE calculations given the large supercell size. The same *k*-grid mesh with HSE06 functional used in the previous $SrCeO_3$ calculations yields good accuracy for defects formation energies and luminescence energies in $SrCeO_3$ [16].

3.2.2. Structure of doped $SrCeO_3$

To study oxygen off-stoichiometry under oxygen-poor conditions, $SrCeO_3$ supercells with two M dopants substituting Ce (M_{Ce}) and zero to two oxygen

vacancies (V_O), denoted as [19], $\{M_{Ce} + 1/2V_O\}$, and $\{M_{Ce} + V_O\}$, respectively, were constructed to model different ratios of dopants to oxygen vacancies. Due to the limited supercell size, the concentration of dopant M and oxygen vacancy is 12.5% on B sites and is 2.1% to 4.2% on O sites, respectively. The representative structure of each doped $SrCeO_3$ with corresponding oxygen vacancies was selected as the lowest GGA energy from 25 ordered configurations with minimal electrostatic energies. The phase diagram was constructed using the *pymatgen* [111].

3.2.3. Polaron formation and migration

We constructed supercells added with one or multiple extra electrons to model polaron formation. To localize the polaron in the calculations, the local lattice surrounding the dopant was distorted in several modes, such as stretching, shrinking, or rotating. To avoid potential artifact of geometric symmetry, various distortion modes were applied to intentionally break the local symmetry in the system, and the symmetry of DFT calculations was switched off. The energies of these calculations on structures with and without the local distortion were relaxed to static equilibrium, and the lowest energy structure was identified and further analyzed. For most dopants investigated, different distortion modes led to the same relaxed charge-localization state unless specified. The charge localization and the polaron formation were validated by the following analyses: (1) partial density of states (PDOS) of the doped structure [30, 32, 112-114], (2) lattice distortion around the dopant [30, 115], (3) magnetic moment of the dopant [93, 116] and (4) the spin density calculated as the difference between spin-up and spin-down electron charge density [16, 110, 115]. We also defined

differential spin density calculated as the difference between the spin densities of two charge states to show the charge localization on dopants. All energies in PDOS plots were referenced to the valence band maximum (VBM), and the calculated Fermi levels denoted by dash lines in the PDOS plots indicate the highest occupied state at 0 K. Using the standard scheme in the literature [117], the transition level $\varepsilon(q/q')$ between different charges q and q' of cation M was calculated as:

$$\epsilon(q/q') = \frac{E(M^q - E(M^{q'}) - (q'-q)\varepsilon_{\mathrm{VBM}})}{q'-q}, \qquad \text{Eq. 6}$$

where $E(M^q)$ is the total energy of the supercell with M^q, and ε_{VBM} is the energy of the VBM of the perfect supercell. It is known that a correction term is needed to account for the unphysical electrostatic interactions caused by the periodic images of charged defects [118]. Since the electrostatic interactions are Coulumb in nature, the energy correction scales with the reciprocal of the dielectric constant of the material [118]. In a previous computation study, corrections for charged defects in $BaCeO_3$ were calculated to be within a few tens of meV due to its high dielectric constant of 98 [110]. We expect a similar small energy correction in $SrCeO_3$, due to its high dielectric constant of 68 [119]. Therefore, we ignored the electrostatic energy correction for charged defect formation as in previous computation studies [120, 121].

In order to calculate polaron-hopping barriers, equilibrium configurations ($\{\mathbf{q_a}\}$ and $\{\mathbf{q_e}\}$), where an electron polaron localized on two adjacent B-site ions respectively, were constructed through the aforementioned lattice distortion. As in previous studies [30, 32, 93], the migration of the polaron was described by the transfer of the lattice distortion over a one-dimensional Born-Oppenheimer surface, with an energy maximum at a configuration between $\{\mathbf{q_a}\}$ and $\{\mathbf{q_e}\}$. To determine this

maximum, we computed energies for a set of configurations $\{\mathbf{q_x}\}$ linearly interpolated between $\{\mathbf{q_a}\}$ and $\{\mathbf{q_e}\}$, i.e., $\{\mathbf{q_x}\} = (1\text{-}x)\{\mathbf{q_a}\} + x\{\mathbf{q_e}\}$, where $0 < x < 1$. The same mixing parameter $\alpha = 0.25$ was used for these calculations except for Eu and Yb. In our calculation, two adjacent Eu (or Yb) dopants always shared partial electrons with the mixing parameter $\alpha = 0.25$, and we adjusted the mixing parameters α to 0.40 to form an electron polaron on adjacent Eu (or Yb) dopants for the polaron migration calculations. Changing the mixing parameter in the HSE functional does not change the nature of polaron formation as shown in our calculations and in previous studies [122].

3.3. Results

3.3.1. Phase stability

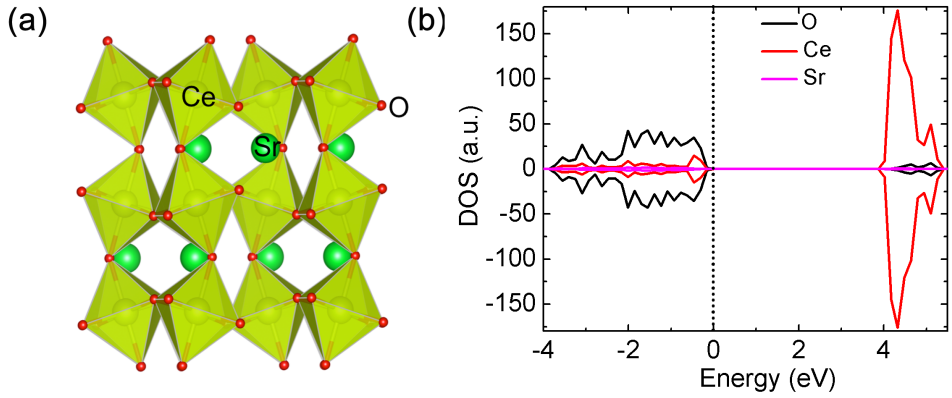

Figure 3.1. (a) Crystal structure of $SrCeO_3$ perovskite (Red: O; Green: Sr; Yellow: Ce; Octahedra: CeO_6). (b) PDOS of $SrCeO_3$. Vertical dash line indicates the calculated Fermi energy at 0 K.

$SrCeO_3$ has an orthorhombic perovskite structure (Fig. 3.1a) with titled CeO_6

octahedra. The lattice parameters of $SrCeO_3$ calculated using HSE06 functional are in good agreement with the experimental values (Table A1 in the Appendices) [123]. The band gap calculated using HSE06 is 4.32 eV (Fig. 3.1b), in agreement of the value of 4.33 eV from previous calculations [16]. Our calculated band gap value using HSE06 is within the range of experimental values, which are 3.5 eV measured by the electron energy-loss spectroscopy (EELS) and diffuse refection measurements [124] and 5-6 eV measured by the optical absorption [125]. The HSE06 hybrid functional calculation predicts a more accurate band-gap value than the GGA-PBE functional, which predicts a band gap of 2.24 eV.

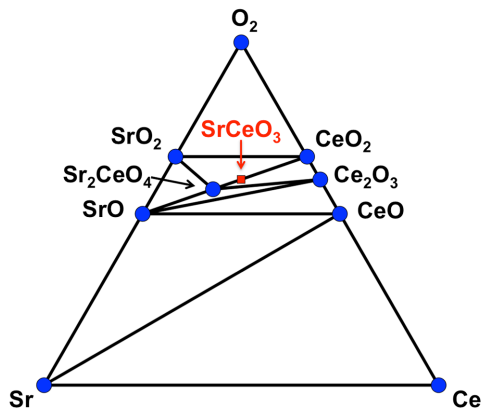

Figure 3.2. Phase diagram of Sr-Ce-O based on GGA energies at 0 K.

According to the Sr-Ce-O phase diagram based on GGA energies from the *Materials Project* [126] (Fig. 3.2), $SrCeO_3$ is slightly metastable at 0 K with an energy above hull [127] of 9 meV per atom and with phase equilibria consisting of Sr_2CeO_4 and CeO_2. As shown in the phase diagram (Fig. 3.2), the stability of $SrCeO_3$ is limited by SrO_2 and Ce_2O_3 under the oxygen-rich and oxygen-poor conditions, respectively. On the basis of HSE06 energies, $SrCeO_3$ has a wide stability region with respect to

oxygen chemical potential $\Delta\mu_O$ from -0.24 eV to -3.55 eV referenced to O_2 gas at 298.15 K and 1 atm. In experiments, $SrCeO_3$ membranes are demonstrated in a wide range of conditions from extremely low oxygen partial pressure of 10^{-20} atm to rich oxygen environment of 1.2 atm oxygen partial pressure [24, 29]. Therefore, our computation results are in agreement with the observed good stability of $SrCeO_3$ under a wide range of oxygen partial pressures.

3.3.2. Off-stoichiometry of doped $SrCeO_3$

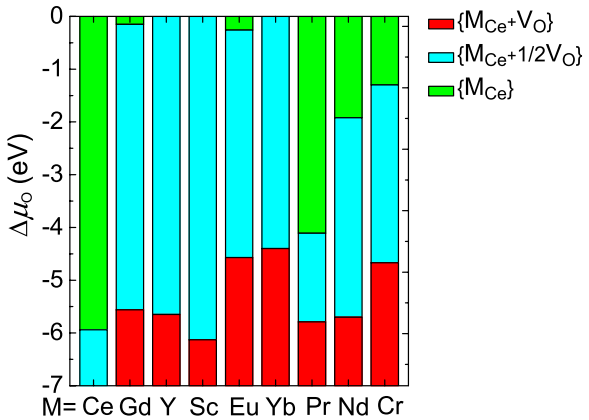

Figure 3.3. The most stable defect regions, $[M_{Ce}]$, $\{M_{Ce} + 1/2V_O\}$, and $\{M_{Ce} + V_O\}$ colored as green, blue, and red, respectively, in M-doped $SrCeO_3$ as a function of $\Delta\mu_O$.

It is known that the formation of oxygen vacancies is facilitated by acceptor doping at Ce sites [85]. Here, we studied the effects of different dopants on oxygen off-stoichiometry in $SrCeO_3$. Some of these B-site dopants were used in previous studies as acceptor doping to incorporate oxygen vacancies and hydrogen. For multivalent cation dopants, such as Eu, Pr and Cr, their oxidation states and corresponding O

vacancy compensation may vary with external oxygen environment. Therefore, different cation dopants may have different response to oxygen chemical potential. In this section, we try to qualitatively compare the trend of different dopants in incorporating O vacancies. We calculated the HSE energies of three different defect regions, i.e., [M_{Ce}], {M_{Ce} + 1/2 V_O}, and {M_{Ce} + V_O}, where M_{Ce} represents cations M substituting Ce sites (Fig. 3.3). The most energetically favorable region is shown in Fig. 3.3 as a function of oxygen chemical potential $\Delta\mu_O$. We used transitions of different regions to qualitatively evaluate the relative trends of different dopants on oxygen off-stoichiometry and their possible oxidation states, since such high defect concentration in the limited supercell model may not be physically achievable.

Pristine $SrCeO_3$ is dominated by [M_{Ce}] region for a wide range of $\Delta\mu_O$. This computation result is consistent with experimental observations that undoped $SrCeO_3$ does not exhibit stable electromotive force (emf) as electrolytes in the steam electrolysis cell due to lack of oxygen vacancies and low protonic conductivity [89] and that acceptor-doped $SrCeO_3$ (e.g. Yb- or Sc-doped) exhibit stable emf and decent proton conductivity [89, 128]. Therefore, acceptor doping is necessary to promote the formation of oxygen vacancies. Indeed, different dopants in $SrCeO_3$ exhibit very different response to oxygen-poor environments. Gd-, Y-, or Sc-doped $SrCeO_3$ is dominated by {M_{Ce} + 1/2V_O} region, suggesting a +3 oxidation state along with incorporated O vacancy per two dopants. The transition of Gd-, Y-, or Sc-doped $SrCeO_3$ to {M_{Ce} + V_O} only happens at extremely oxygen-poor conditions and may be difficult to physically achieve. By contrast, Eu- or Yb-doped $SrCeO_3$ exhibits easier transition from {M_{Ce} + 1/2V_O} region to {M_{Ce} + V_O} than Gd-, Y-, or Sc-

doped one. This trend indicates Eu and Yb dopants may potentially exhibit multiple oxidation states such as +2 and +3 at oxygen-poor conditions, which are the case of hydrogen separation. Pr- or Nd-doped $SrCeO_3$ exhibits the transition from $[M_{Ce}]$ to $\{M_{Ce} + 1/2V_O\}$ at significantly higher $\Delta\mu_O$ compared to aforementioned doped ones, indicating possible oxidation states of +3 and +4 in Pr and Nd dopants. Among all these dopants, Cr-doped $SrCeO_3$ shows the transition from $[M_{Ce}]$ to $\{M_{Ce} + 1/2V_O\}$ and from $\{M_{Ce} + 1/2V_O\}$ to $\{M_{Ce} + V_O\}$ at $\Delta\mu_O \approx -1.3$ eV and -4.7 eV, respectively, implying possible +4, +3 and +2 oxidation states of Cr. These computation results indicate that different dopants have different capabilities to induce oxygen vacancies as a function of oxygen partial pressure and may exhibit different oxidation states.

In addition, it should be noted that the actual oxidation states of dopants and their concentrations are a function of the doping level and other defects (e.g. cation defects, polarons, etc.). A comprehensive evaluation of all possible defect formation and compensation mechanisms to identify the exact oxidation states of dopants is beyond the scope of this work. Here we only considered the charge compensation of oxygen vacancies, which are expected to be the dominant charge compensation mechanism in the oxygen-poor operational condition of this material as hydrogen membranes [92]. Given we are comparing the formation energies at the same oxygen vacancy concentration, the relative trend among dopants should reflect their different tendencies to change oxidation states and to incorporate oxygen vacancies.

3.3.3. Pristine $SrCeO_3$

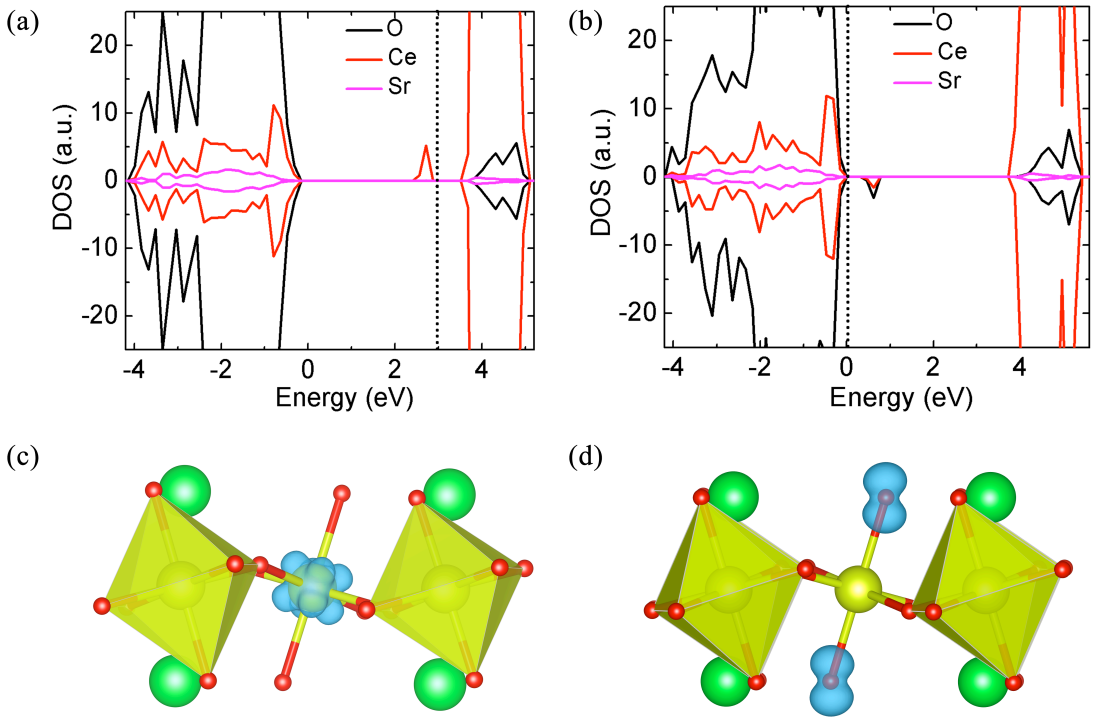

Figure 3.4. An electron polaron e_p localized on the Ce site as shown by PDOS (a) and spin density (c), and a hole polaron h_p localized on the CeO_6 polyhedron as shown by PDOS (b) and spin density (d). Vertical dash lines in PDOS plots indicate the calculated Fermi energy at 0 K. The isosurface of the spin density is 10% of the maximum.

To investigate the formation of electron polaron in pure $SrCeO_3$, we added an extra electron into pure $SrCeO_3$, and calculated the electronic structure of the charge localization states (Fig. 3.4ac). In comparison with the DOS of pure $SrCeO_3$ with no in-gap state (Fig. 3.1b), an occupied 4*f* state from Ce can be observed in the band gap below the calculated 0 K Fermi level (Fig. 3.4a), confirming the formation of electron polaron e_p on Ce cation. In addition, the spin density on the Ce site also suggests

charge localization (Fig. 3.4c), indicating a transition from Ce^{4+} to Ce^{3+}. The trapping of an electron polaron on the Ce site is also shown by the increase of average Ce-O bond length from 2.24 Å to 2.36 Å in the CeO_6 octahedron, as a result of decreased electrostatic attraction between Ce and O ions. Since $SrCeO_3$ is a wide band-gap material, the electronic conductivity of undoped $SrCeO_3$ (i.e., 2.82×10^{-4} S/cm at 1073 K) was attributed to the charge transfer between Ce ions [24]. Our computation results based on HSE06 functional directly confirm the electron polaron localization on Ce in $SrCeO_3$, whereas GGA functional fails to localize the electron.

By removing an electron from pure $SrCeO_3$, we found that the CeO_6 octahedron can trap a hole polaron h_p (Fig. 3.4d). The PDOS (Fig. 3.4b) also confirms an empty hole state above the calculated 0 K Fermi level. The charge localization is shown by the spin density localized on two apical oxygen ions. Our calculations always found the charge localization on two apical oxygen ions regardless of different unsymmetrical local lattice distortion modes tested. The hole polaron trapping is energetically more favorable (0.2 eV lower) than the delocalized hole state. Similar hole trapping at B-site MO_6 octahedron was previously reported in other perovskites such as $KNbO_3$ [129-131].

3.3.4. Polaron and oxygen vacancy in $SrCeO_3$

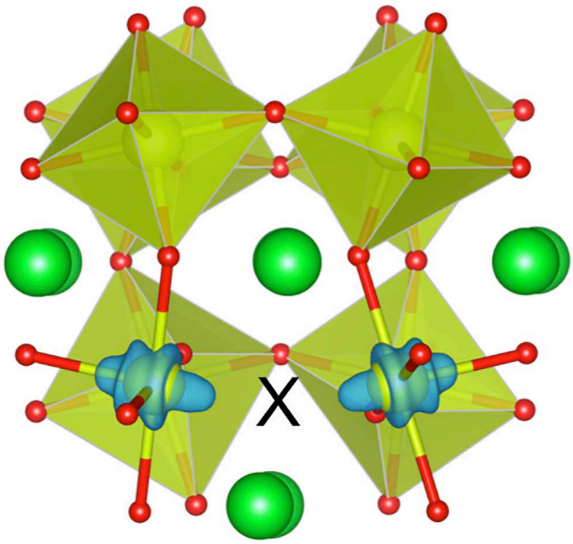

Figure 3.5. Oxygen vacancy $V_O^{\bullet\bullet}$ shown by the black cross with two electron polarons e_p localized on adjacent Ce ions as shown by spin density. The isosurface of the spin density is 10% of the maximum.

We investigated the polaron formation induced by intrinsic defects such as oxygen and cation vacancies. Two excess electrons introduced by an oxygen vacancy tend to localize on two adjacent Ce ions, forming a complex of $V_O^{\bullet\bullet}$ and two Ce-trapped electron polarons (Fig. 3.5**)**. This complex is likely more energetically favorable than the hypothetical state of localizing electrons on the oxygen vacancy, which cannot be stabilized in our calculations. In addition, holes introduced by a Sr or Ce vacancy (Fig. A1 and A2**)** are trapped by oxygen ions adjacent to the cation vacancy, similar to the hole localization in pure $SrCeO_3$ (Fig. 3.4d). Therefore, polarons in pure $SrCeO_3$ can also be introduced by various intrinsic defects. In the following subsections 3.3.3 to 3.3.6, the polaron formation in doped $SrCeO_3$ was

studied in the supercell with no cation or oxygen vacancy in order to show the intrinsic charge trapping capability of the dopant and to exclude the interaction between charge localization and other defects.

3.3.5. Polaron in Gd-doped $SrCeO_3$

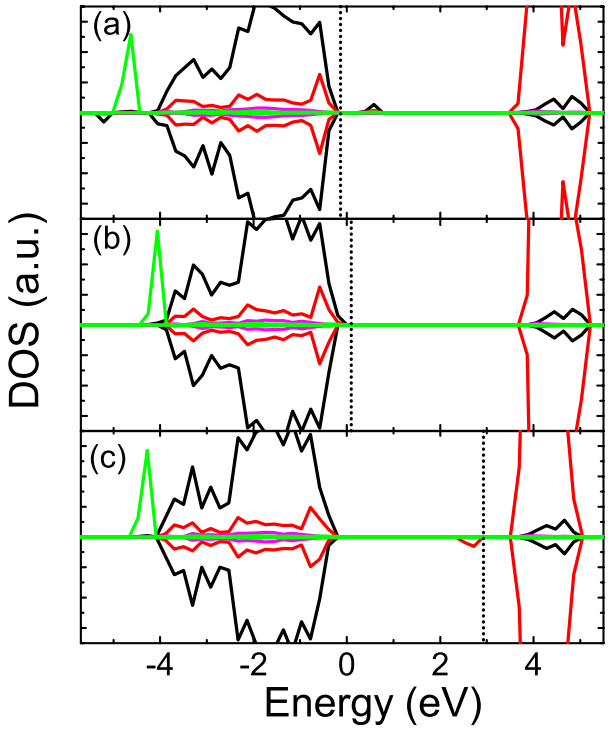

Figure 3.6. PDOS of Gd-doped $SrCeO_3$ with (a) Gd'_{Ce} and a hole polaron h_p localized on the GdO_6 octahedron, (b) Gd'_{Ce} , or (c) Gd'_{Ce} and an electron polaron e_p localized on Ce. (Red: Ce; Black: O; Purple: Sr; Green: Gd). Vertical dash lines indicate the calculated Fermi energy at 0 K.

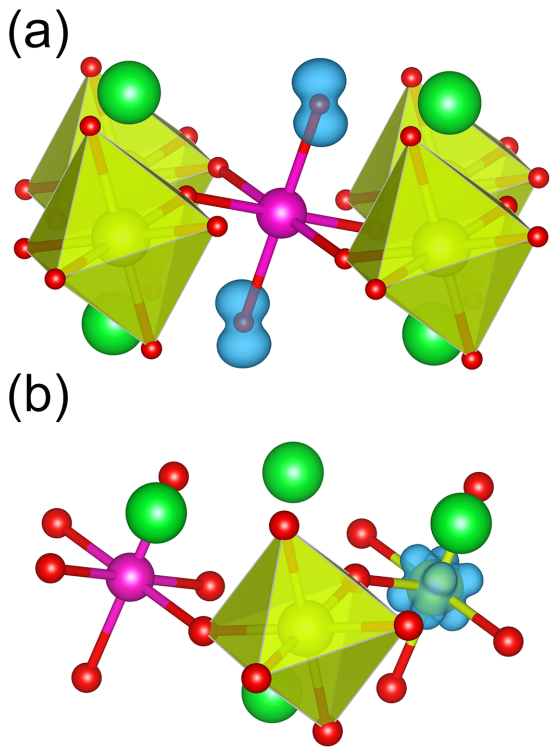

Figure 3.7. (a) A hole polaron h_p on the GdO_6 octahedron as shown by the differential spin density between Gd'_{Ce} and Gd'_{Ce} + h_p, and (b) an electron polaron e_p localized on the Ce site as shown by the differential spin density between Gd'_{Ce} + e_p and Gd'_{Ce}. The Gd dopant is shown in purple. The isosurfaces of the differential spin densities in blue and yellow correspond to 10% of the maximum and minimum, respectively.

In this section, we studied the Gd, Sc, and Y dopants, which are commonly shown as +3 dopant to incorporate oxygen vacancies into $SrCeO_3$ [85]. The PDOS of Gd-doped $SrCeO_3$ with Gd^{3+} oxidation state is shown in Fig. 3.6b. The calculated magnetic moment of 6.9 μ_B on Gd confirms its +3 oxidation state as Gd'_{Ce}. Similar to that on Ce (Fig. 3.4d), a hole polaron can be localized on the GdO_6 octahedron and

prefers to localize on two apical oxygen ions neighboring Gd (Fig. 3.7a). The PDOS of Gd-doped $SrCeO_3$ with a hole polaron shows an empty hole state of these apical O ions (Fig. 3.6a). Similar hole state attributed to oxygen ions neighboring Gd was previously reported in Gd-doped $BaCeO_3$ [116]. In addition, we also explored possible electron polaronic state of Gd by adding one electron into the system. The additional electron localizes on a Ce ion instead of Gd, as shown by Ce state in PDOS (Fig. 3.6c) and the differential spin density (Fig. 3.7b). Thus, Gd remains an oxidation state of +3 as Gd'_{Ce}. This result indicates the weaker electron trapping capability of the dopant than Ce cation. In addition, Sc and Y dopants in $SrCeO_3$ show similar behaviors as Gd (Fig. A3 and A4). Therefore, these +3 dopants induce oxygen vacancies into the material but lack the ability to form electron polarons.

3.3.6. Polaron in Eu-doped $SrCeO_3$

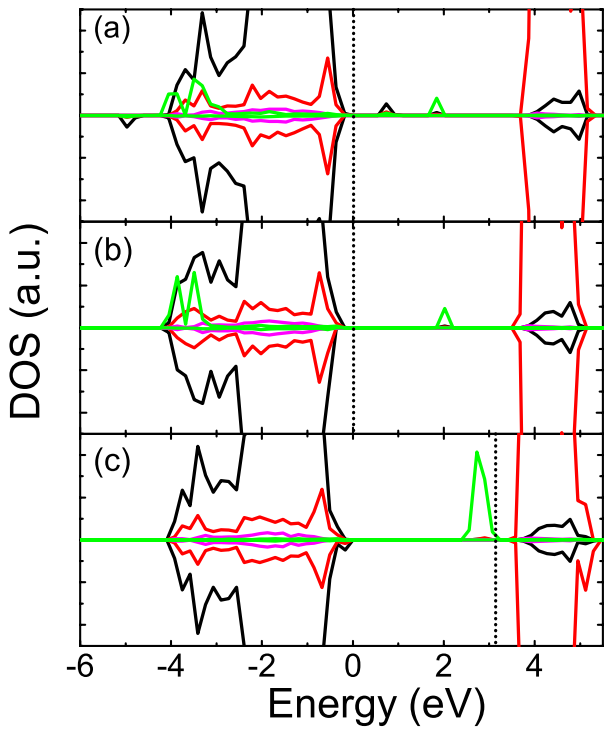

Figure 3.8. PDOS of Eu-doped $SrCeO_3$ with (a) Eu'_{Ce} and a hole polaron h_p on the EuO_6 octahedron, (b) Eu'_{Ce}, or (c) Eu''_{Ce}. (Red: Ce; Black: O; Purple: Sr; Green: Eu). Vertical dash lines indicate the calculated Fermi energy at 0 K.

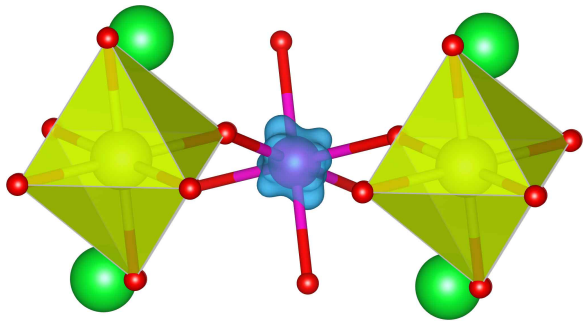

Figure 3.9. An electron polaron localized on the Eu site forming Eu''_{Ce} as shown by the differential spin density between Eu''_{Ce} and Eu'_{Ce}. The Eu dopant is shown in purple. The isosurfaces of the differential spin density in blue and yellow correspond

to 10% of the maximum and minimum, respectively.

The polaron formation and migration between $Eu^{3+/2+}$ in Eu-doped $SrCeO_3$ has been proposed as a mechanism in increasing electronic conductivity [26, 28, 29, 92]. Indeed, we confirm the formation of polarons induced by Eu dopant. In Eu-doped $SrCeO_3$ with Eu^{3+} [92], the PDOS shows an unoccupied Eu-contributed state in the gap above the calculated Fermi level (Fig. 3.8b). Similar to that in pure or Gd-doped $SrCeO_3$, the formation of a hole polaron h_p localized on the EuO_6 octahedron is shown by the empty hole state (Fig. 3.8a) mostly from O. In contrast to Gd, Sc, and Y dopants, Eu can trap an extra electron to form an electron polaron. Comparing to the unoccupied in-gap Eu state for Eu^{3+} (Fig. 3.8ab), the in-gap Eu state shifts towards the conduction band minimum (CBM), and is occupied as indicated by the calculated Fermi level (Fig. 3.8c). This valence change of Eu from 3+ to 2+ is also manifested by the magnetic moment change of Eu from 6.0 μ_B to 6.8 μ_B. In addition, the electron polaron on Eu (Fig. 3.9**)** distorts the local lattice, leading to an increase of average Eu-O bond length from 2.32 Å to 2.42 Å in the EuO_6 octahedron. Similar to Eu, Yb can trap an electron polaron by the transition from Yb^{3+} to Yb^{2+} (Fig. A5 and A6). Therefore, the ability to form electron polaron on Eu and Yb is consistent with their +3/+2 multivalence, which has been shown in section 3.2 as a function of oxygen environments. Such multivalence behaviors of Eu and Yb are absent in other +3 dopants, such as Gd, Sc, and Y (chapter 3.3.5). Our computation results confirm the polaron formation as a result of Eu in $SrCeO_3$, which is proposed as the mechanism for increased electronic conductivity in Eu-doped $SrCeO_3$ [28]. To further support the

polaron migration mechanism, the concentration of the polaron would be dependent on the actual condition of the materials as discussed section 3.4, and the migration of this polaron is evaluated in section 3.3.10. In prior experimental studies, the electronic conductivities of Eu- and Yb-doped $SrCeO_3$ were reported as high as ~1 × 10^{-3} S/cm at 1000-1200 K [24, 26, 87, 92], which was higher than those of pure, Y-doped, and Sc-doped $SrCeO_3$ [24, 25, 89].

3.3.7. Polaron in Pr-doped $SrCeO_3$

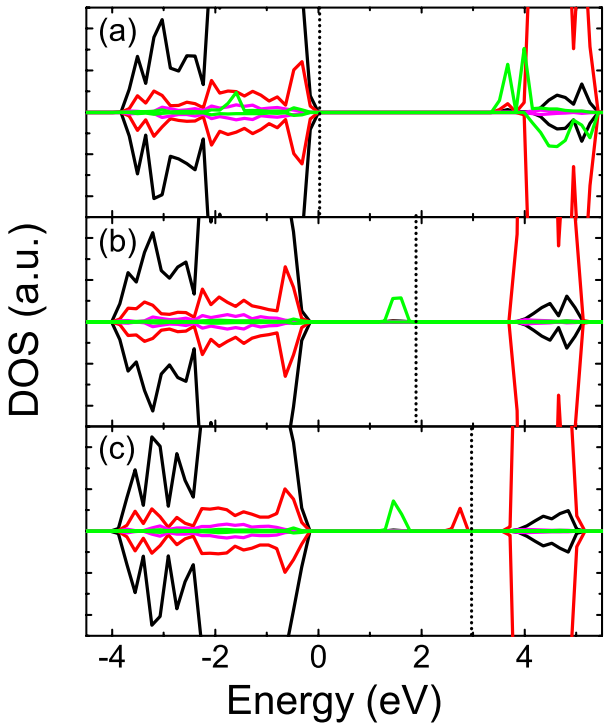

Figure 3.10. PDOS of Pr-doped $SrCeO_3$ with (a) $Pr_{Ce}^{\times}$, (b) Pr_{Ce}', or (c) Pr_{Ce}' with an electron polaron e_p localized on a Ce ion. (Red: Ce; Black: O; Purple: Sr; Green: Pr). Vertical dash lines indicate the calculated Fermi energy at 0 K.

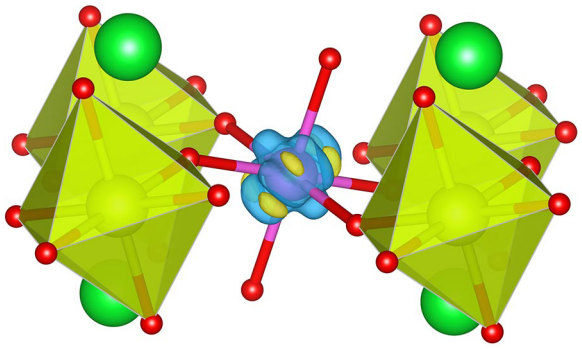

Figure 3.11. An electron polaron localized on the Pr site forming Pr'_{Ce} as shown by the differential spin density between Pr'_{Ce} and $Pr^{\times}_{Ce}$. The Pr dopant is shown in purple. The isosurfaces of the differential spin density in blue and yellow correspond to 20% of the maximum and minimum, respectively.

We studied the polaron formation in $SrCeO_3$ doped by Pr, which has +3/+4 multivalence oxidation states [101]. The actual oxidation state of Pr in the materials is dependent on the specific condition of the materials (section 3.3.2). In the defect-free charge-neutral supercell model, Pr has an oxidation state of +4 and a magnetic moment of 1.2 μ_B. We found that an excess electron (Fig. 3.11) can localize on Pr ion turning its oxidation state from +4 to +3, as shown by the change in PDOS (Fig. 3.10ab) and the increase of Pr magnetic moment from 1.2 μ_B to 2.0 μ_B. The localized electron polaron also distorts the local lattice and increases the average Pr-O bond length from 2.23 Å to 2.34 Å in the PrO_6 octahedron. Another extra electron added into the system would localize on a Ce ion instead of the Pr ion (Fig. 3.10c), suggesting that Pr^{2+} is energetically less favorable than Ce^{3+}. Similarly, Nd dopant can exhibit a transition between Nd^{4+} / Nd^{3+} (Fig. A7 and Fig. A8). Nd with oxidation state +4 was observed in a few materials [100, 102], and Nd dopant with +4 may be

possibly formed in $SrCeO_3$ at certain conditions. In physical materials, Pr dopant may have the dominant oxidation state of either +4 or +3 depending on the specific conditions of the material. The charge may be trapped on Pr for either case, and the migration of the formed polarons contributes to the electronic conductivity. In preliminary experiments [132], the electronic conductivity and the H_2 permeation rate of $SrCe_{0.8}Pr_{0.2}O_{3-\delta}$ was reported to increase compared to those of Y-doped $SrCeO_3$ [25]. Therefore, our computation results are supported by the preliminary experiments observing enhanced electronic conductivity in Pr-doped $SrCeO_3$ [132].

3.3.8. Polaron in Cr-doped $SrCeO_3$

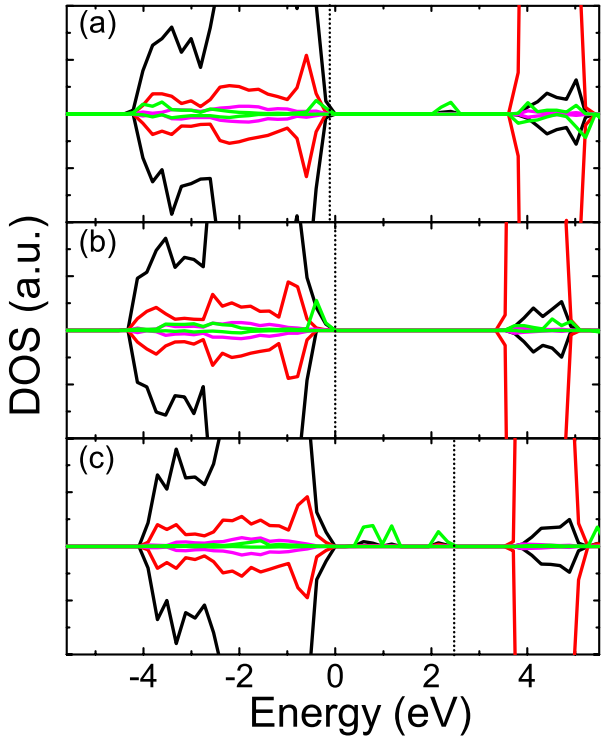

Figure 3.12. PDOS of Cr-doped $SrCeO_3$ with (a) $Cr_{Ce}^{\times}$, (b) Cr_{Ce}', or (c) Cr_{Ce}''. (Red: Ce; Black: O; Purple: Sr; Green: Cr). Vertical dash lines indicate the calculated Fermi

energy at 0 K.

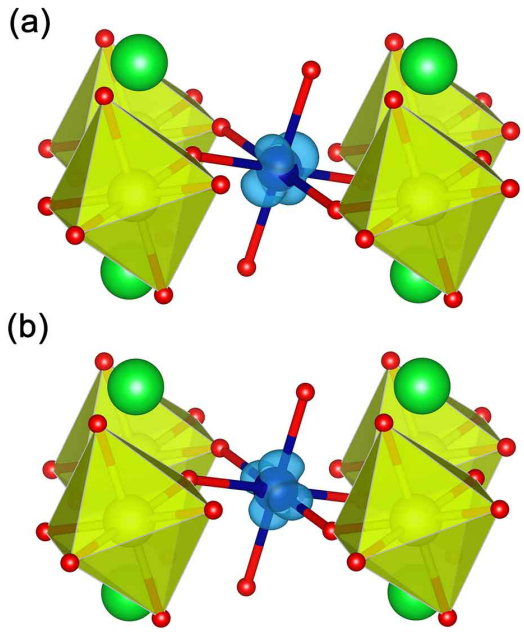

Figure 3.13. Electron polarons localized on the Cr site as shown by the differential spin densities (a) between Cr'_{Ce} and $Cr^{\times}_{Ce}$ and (b) between Cr''_{Ce} and Cr'_{Ce}. Cr dopant is shown in blue. The isosurfaces of the differential spin densities in blue and yellow correspond to 10% of the maximum and minimum, respectively.

We studied the polaron formation in Cr-doped $SrCeO_3$, as +2/+3/+4 multivalent Cr may be a potential dopant to trap polarons. In the defect-free charge-neutral supercell model, Cr ion in $SrCeO_3$ has an oxidation state +4 ($Cr^{\times}_{Ce}$) with a magnetic moment of 2.1 μ_B. An unoccupied in-gap Cr state (Fig. 3.12a) implies the ability to capture an extra electron. Indeed, $Cr^{\times}_{Ce}$ can trap an extra electron and become Cr'_{Ce} (Fig. 3.13a), as shown by the change in PDOS (Fig. 3.12b). This Cr'_{Ce} state is also manifested by the increase of Cr magnetic moment to 2.9 μ_B and the

increase of the average Cr-O bond length in the CrO_6 octahedron from 2.01 Å to 2.14 Å. In contrast to all other dopants we studied, Cr'_{Ce} can further trap one additional electron to become Cr''_{Ce} (Fig. 3.13b), which is confirmed by the PDOS (Fig. 3.12c) and by the increase of the average Cr-O bond length to 2.32 Å. However, the Cr''_{Ce} state is energetically less favorable (0.65 eV higher) than localizing the electron to Ce forming e_p. Our computation results suggest the ability of Cr dopant to form polarons and to potentially increase electronic conductivity in $SrCeO_3$. These computation results are in agreement with preliminary experimental measurements [132], where the electronic conductivity of $SrCe_{0.9}Cr_{0.1}O_{3-\delta}$ was reported higher than those of pure, Y-doped, and Sc-doped $SrCeO_3$.

3.3.9 Transition level

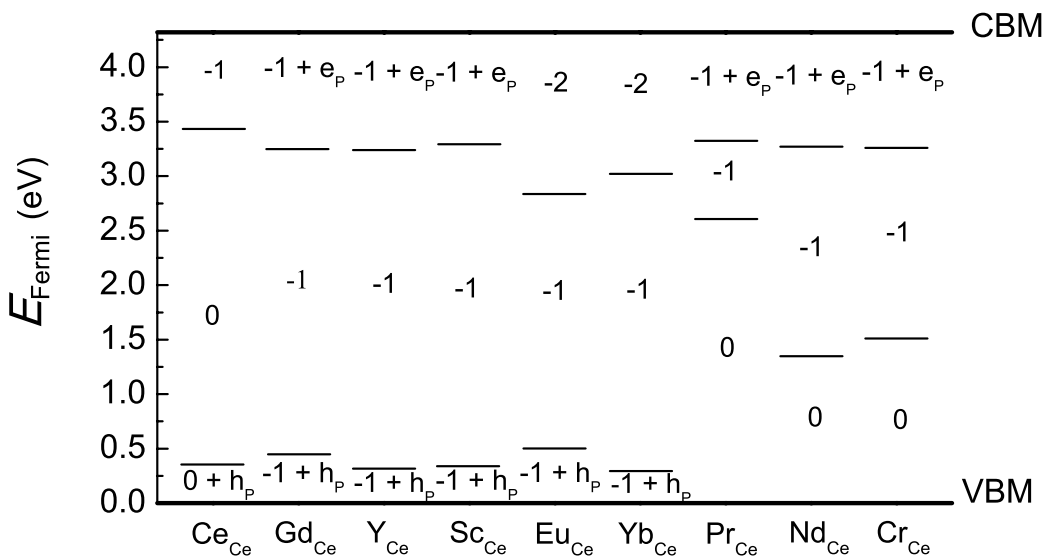

Figure 3.14. Transition levels between different charge states of different dopants in $SrCeO_3$. The number is the actual charge state of M_{Ce}, e_p is an electron polaron

localized on Ce, and h_p is a hole polaron localized on the B-site cation oxygen octahedron CeO_6 or MO_6.

The polaronic states induced by various dopants in $SrCeO_3$ change according to the physical conditions of the material. We calculated transition levels of dopants between charge states as a function of the Fermi level (Fig. 3.14 and Table A2). The transition level between Ce^{4+} to Ce^{3+} by trapping an electron polaron is close to the CBM at 3.43 eV. Other dopants, such as Gd, Y, Sc, Pr, Nd, and Cr, show similar transition level from -1 to $-1+e_p$ as Ce. Among all these dopants, Eu and Yb can show transitions from -1 to -2 charge at significantly lower transition energies of 2.84 and 3.02 eV, respectively. For transitions from $-1+h_p$ states to -1 states, Gd, Y, Sc, Eu, and Yb exhibit transitions at < 0.5 eV close to the VBM, similar to Ce's transition from $0+h_p$ to charge neutral state (0). However, Pr, Nd and Cr exhibit transitions from 0 to -1 charge at significantly higher energies of 2.61, 1.35 and 1.51 eV, respectively. Therefore, different dopants exhibit highly different charge trapping and polaron formation behaviors and energetics, which would lead to different defect equilibria and polaron concentrations. The formation energies of polarons depend on the Fermi level of the doped materials. The actual Fermi level depends on the doping concentration and the equilibria of various defects in the materials at specific conditions. Since the computation of the actual Fermi level is beyond the scope of this work, its impact on the polaron concentration and related properties is elaborated in Discussion 3.4.

3.3.10. Polaron migration barriers

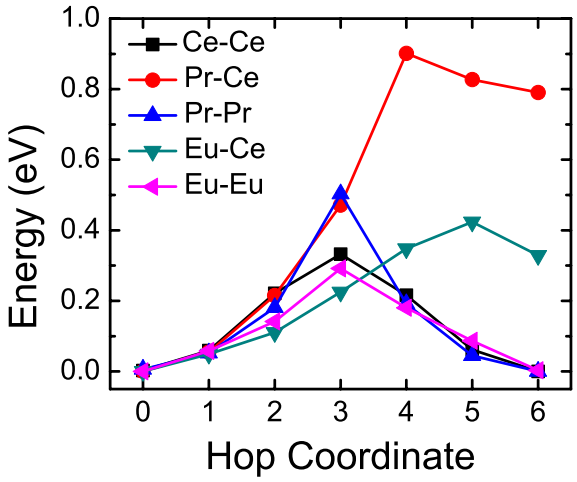

Figure 3.15. Energy profiles for the migrations of polarons in pure and doped $SrCeO_3$.

In addition to the formation and concentration of polarons, the mobility of polarons is also crucial for charge transport. We calculated the polaron-hopping barriers between two adjacent B-site ions through the static self-consistent calculations along the migration path (section 3.2.3). In pure $SrCeO_3$, the migration barrier between two adjacent Ce ions is 0.33 eV (Fig. 3.15), illustrating relatively mobile electron polarons in $SrCeO_3$. Therefore, the computation confirmed the charge hopping between $Ce^{4+/3+}$ contributing to electron conductivity of $SrCeO_3$ [24].

For doped $SrCeO_3$, polaron hopping happens between two adjacent dopants (M-M) and between a dopant and Ce (M-Ce). Migration barriers of Pr-Pr and Eu-Eu are 0.50 eV and 0.29 eV, respectively. In addition, migration barriers of Pr-Ce and Eu-Ce were 0.90 eV and 0.42 eV, respectively. These high polaron-hopping barriers of M-Ce result from the energy difference between the equilibrium polaronic states,

as the polaron localized on dopants has lower energy than one localized on Ce. This is consistent with our results that Eu and Pr dopants have stronger capabilities to trap electrons. In addition, the polarons formed on other dopants have similar migration barriers as Eu and Pr (Table A3). The low migration barriers of electron polarons in pure or doped $SrCeO_3$ support the polaron mechanism for electronic conductivity in $SrCeO_3$ [24, 132].

3.4. Discussion

For active polaron mechanism contributing to electronic charge transport, the good mobility of polaron and decent concentration of polaron carriers are needed. Our computation predicted low energy barriers for the polaron migration and identified the formation of various polaronic states in pure and doped $SrCeO_3$, supporting both essential factors for polaronic charge transport. The $SrCeO_3$ hydrogen permeation membranes operate at low oxygen partial pressures and are known to exhibit n-type conduction, where electronic conductivity is significantly higher than hole conductivity [25, 26, 87, 92]. Therefore, the band conduction mechanism in enhancing electronic conductivity is excluded, as these dopants are acceptors. Given the calculated low migration barrier for polarons, the easy formation of polarons to achieve decent concentration is the key factor for increasing electronic conductivity. The formation energy of polaron is a function of the actual Fermi level depending on external conditions such as oxygen and hydrogen partial pressures, and so is the concentration of polaron carriers for charge transport. In experiments, the electronic conductivity of Eu- or Yb-doped $SrCeO_3$ was higher than that of pure or

Gd-, Y-, Sc-doped $SrCeO_3$ under low oxygen partial pressures [24-26, 87, 89, 92]. The increase of electronic conductivity results from electron polarons induced by Eu and Yb dopants in $SrCeO_3$. Given distinctive polaronic behaviors and the lower polaronic transition levels of Eu and Yb compared with those of Gd, Y and Sc as shown in our computation results, higher concentrations of polarons in Eu- or Yb-doped $SrCeO_3$ may be achieved when the actual Fermi level is close to the transition levels of Eu and Yb's polaronic states. Therefore, our computation results support the higher concentration of polarons as active charge carriers for higher electronic conductivity in Eu- and Yb-doped $SrCeO_3$. The higher polaron concentration in Eu- or Yb-doped $SrCeO_3$ dominates the conductivity enhancements. In contrast, other dopants such as Gd, Y, and Sc lack such polaron trapping capability. Instead, these B-site dopants may impede the polaron hopping paths between Ce ions, and therefore their electronic conductivities were similar to that of undoped $SrCeO_3$ as shown in the experiments [24, 25, 89]. For new dopants, Pr exhibits strong charge trapping capability and a similar transition level as Eu, and is expected to achieve an increased concentration of polarons under similar conditions. The effect of Pr doping on enhancing electronic conductivity was confirmed by preliminary experiments [132], which validate our computation predictions. Our calculation results for all dopants are in agreement with experiments.

In addition, our computational study provides theoretical basis of dopant-induced polaron behavior for the electronic transport increase in certain doped $SrCeO_3$. To the best of our knowledge, our study is the first to reveal the different polaronic behavior of different dopants on electronic transport. In summary, our

computation shows that the doping elements with single fixed valence state generally have poor capability to trap charge and to localize polarons. The doping elements with multivalence nature in general have better capabilities to form polarons as previously expected. However, the actual behavior of dopants varies greatly from element to element, and the polaron formation energy and transition levels would be important to determine which dopants would outperform others at specific conditions. For example, while Ce and Pr both show +4/+3 transition, the transition level of Ce may be further away from the actual Fermi level, leading to lower polaron concentration and polaron-induced charge transport. For the operational conditions of H_2 membranes, our computation agrees with experimental observations that Eu, Yb, and Pr dopants showed good performance. Our achieved understanding and demonstrated computation scheme for predicting new dopants are important for future materials development for enhancing electronic conductivity and overall hydrogen flux in ceramic hydrogen separation membranes.

Our study demonstrated the first principles hybrid functional computation in studying different polaronic states on various dopants and in predicting new dopants for enhanced properties. The computation techniques based on hybrid functional demonstrated in this study provide a general scheme for designing new materials with different polaron formation through doping. Engineering polaronic states through doping is a general design strategy to tailor materials properties. Similar to $SrCeO_3$ membrane studied here, doping in other materials such as electrodes for batteries and fuel cells may also activate polaron mechanism and increase electronic conductivity, which is crucial for the electrochemical performance. Our computation approach

demonstrated in this study has the potential to accelerate the selection of dopants for the materials optimization.

3.5. Conclusions

Using *ab initio* calculations based on hybrid functional, we demonstrated and confirmed polaron formation and migration in $SrCeO_3$ perovskite. Our computational study reveals that different dopants in $SrCeO_3$ exhibit highly different polaron formation behaviors and energetics. Electron polarons migrate with low barriers and good mobility between B-site ions in some doped $SrCeO_3$. Our study provides the theoretical basis to support the polaron migration mechanism for increasing electronic conductivity in some doped $SrCeO_3$, and the computation scheme was applied to predict new dopants. The demonstrated computation scheme provides a generally applicable approach to designing materials with tailored polaron formation and enhanced functional properties.

Chapter 4: Effect of cation substitution on hydride-ion transport in the new oxyhydrides[§]

4.1. Introduction

Ion-conducting materials with different mobile ion species are crucial components of electrochemical energy storage systems. Currently, most battery systems, e.g., alkaline batteries,[133, 134] Li-ion batteries,[42, 43] Na-ion batteries,[135] are based on mobile cation ions, such as Li^+, Na^+, etc. Recently, new battery systems based on mobile anions have attracted interest.[5, 40, 136] In particular, hydride ion may potentially be an attractive charge carrier for electrochemical energy storage, since the high standard redox potential of H_2/H^- (-2.3 V) may lead to high voltage and high energy density.[137] Compared to proton (H^+) conductors widely known in oxide materials,[7, 138, 139] hydride ion (H^-) conductor is rare and only known in a few metal hydrides[36, 140, 141] and oxyhydrides.[38, 140, 142-145] A recent breakthrough study discovered new $La_{2-x-y}Sr_{x+y}LiH_{1-x+y}O_{3-y}$ ($0 \leq x \leq 1$, $0 \leq y \leq 2$, $0 \leq x+y \leq 2$) oxyhydrides and demonstrated an exceptionally high H^- conductivity of 0.12 mS/cm at 573 K in this materials system.[5, 40] The discovery of the oxyhydrides opens a promising direction for electrochemical solid-state energy storage devices based on H^- conduction.

[§] This chapter has been published in
Q. Bai, X. He. Y. Zhu, Y. Mo, "First-Principles Study of Oxyhydride H^- Ion Conductors: Towards Facile Anion Conduction in Oxide-Based Materials", ***ACS Applied Energy Materials*** 1 (2018) (4) 1626.

The newly discovered hydride-ion conductor oxyhydride family, $La_{2-x-y}Sr_{x+y}LiH_{1-x+y}O_{3-y}$, has a K_2NiF_4-type (A_2BX_4) structure (Fig. 4.1), where La/Sr occupy the A sites, Li occupy the B sites and O/H occupy the X sites.[5] The $La_{2-x-y}Sr_{x+y}LiH_{1-x+y}O_{3-y}$ composition can be understood as the solid solutions of La_2LiHO_3 (x = 0, y = 0) and Sr_2LiH_3O (x = 0, y = 2) with the mixing ratio 1-y/2 : y/2, and x indicates the A-site Sr-to-La substitution to create H^- vacancies with concentration x.[5] It is reported that H^- conductivity increases with increasing the number of H^- (y) from La_2LiHO_3 ($x = y = 0$), $LaSrLiH_2O_2$ (x = 0, y = 1) to Sr_2LiH_3O (x = 0, y = 2).[5] In addition, the configuration of H^- and O^{2-} sublattice shows site preferences in different compositions with respect to y (Fig. 4.1). For example, H^- prefer to occupy axial sites than apical sites on LiX_6 octahedra (Fig. 4.1). The site preference in anion sublattice is a unique structural feature of this material and is known to significantly impact H^- diffusion mechanism. In addition, $La_{2-x-y}Sr_{x+y}LiH_{1-x+y}O_{3-y}$ oxyhydrides significantly outperform pervious oxyhydride materials in H^- conduction, such as the perovskites ($ATiO_{3-x}H_x$, A: Ca, Sr, Ba)[144, 146-151]. It is important to understand why $La_{2-x-y}Sr_{x+y}LiH_{1-x+y}O_{3-y}$ oxyhydrides based on K_2NiF_4 structures can significantly outperform other structures in H^- ion conduction. Understanding the structural feature and diffusion in these novel materials and their outstanding performances would be crucial for the discovery of new anion conductor materials.

First principles atomistic modeling can provide unique understanding into the diffusion mechanism of H^- in the oxyhydrides and its dependence on the anion sublattices in the structures at various compositions. The enhanced understanding of the structure-diffusion relationship from the atomistic-scale in these new H^-

conductors would guide the design of these materials for increased ionic conductivity and novel oxide-based anion conductors in general. In this chapter, we first investigated the structural origin of H^- and O^{2-} anion sublattices in the $La_{2-x-y}Sr_{x+y}LiH_{1-x+y}O_{3-y}$ oxyhydrides (section 4.3.1-4.3.2), we then elucidated the H^- diffusion mechanism in different anion sublattices due to cation substitution (section 4.3.3-4.3.4). In addition, we computationally predicted newly doped oxyhydrides with improved H^- conductivity and reasonable stability (section 4.3.5). In section 4.4, we discussed the origin of K_2NiF_4-type structure as a promising structure for anion conduction and proposed general guidance for designing new anion conductors based on oxides.

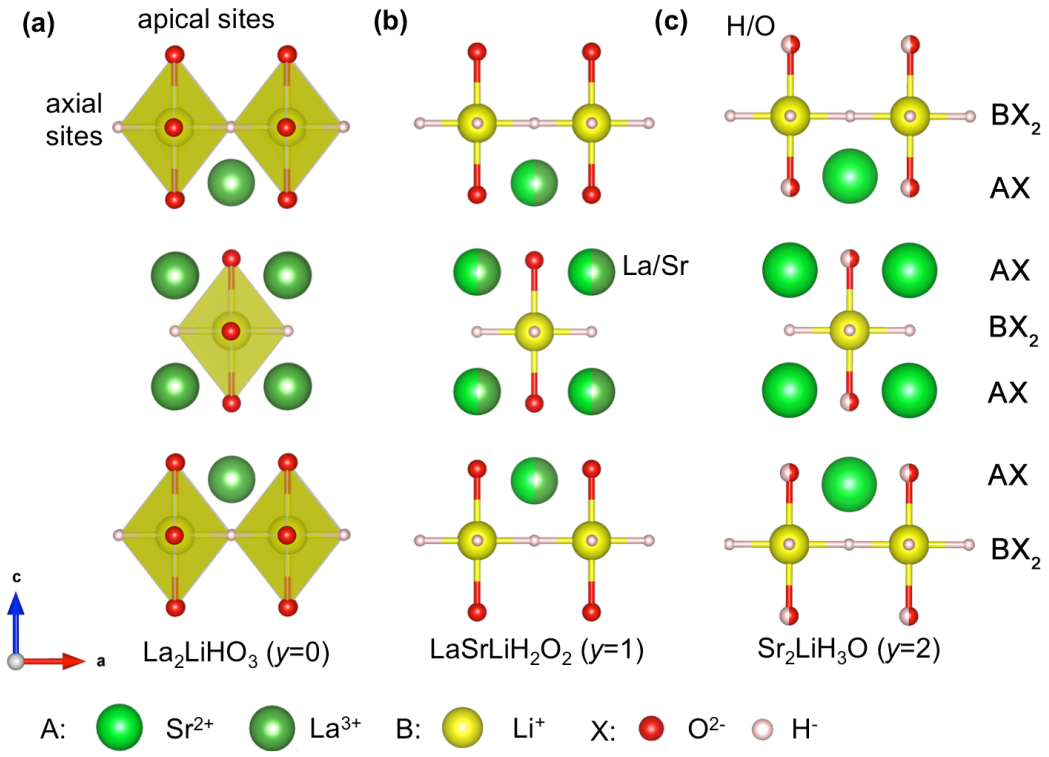

Figure 4.1. K_2NiF_4-type unit cells of (a) La_2LiHO_3, (b) $LaSrLiH_2O_2$ and (c) Sr_2LiH_3O with a formula unit of A_2BX_4 (A = La, Sr; B = Li; X = H, O). Sr^{2+} and/or La^{3+} co-occupy the A sites. Li^+ occupy the B sites to form LiX_6 octahedra. X sites can be categorized into apical sites and axial sites. La_2LiHO_3 is an ordered orthorhombic structure, $LaSrLiH_2O_2$ has the tetragonal phase with the disordered A-site sublattices of La/Sr, and Sr_2LiH_3O has the tetragonal phase with disordering of H/O at apical sites.

4.2. Methods

All density functional theory (DFT) calculations were performed using the projector augmented-wave (PAW)[56] approach implemented in the Vienna *Ab initio* Simulation Package (VASP).[57] All total energy calculations were performed using

the Perdew-Burke-Ernzerhof (PBE) generalized-gradient approximation (GGA) functional.[58] The static DFT calculations were spin-polarized using the convergence parameters consistent with the *Materials Project*,[59] which have total energies converged to 1 meV per atom. The band gap calculations were performed using Heyd-Scuseria-Ernzerhof (HSE06) hybrid functional[60, 61, 104] with a single gamma point. The Born-effective-charge tensors[152, 153] were calculated based on the density functional perturbation theory (DFPT) implemented in VASP.[154] All calculations for the oxyhydrides were based on supercells with 3×3×1 unit cells and 18 formula units of A_2BX_4 (A = La, Sr; B = Li; X = H, O).

4.2.1. Site ordering of the oxyhydrides

$La_{2-x-y}Sr_{x+y}LiH_{1-x+y}O_{3-y}$ oxyhydrides have K_2NiF_4-type structures with La^{3+}/Sr^{2+} sharing A sites and H^-/O^{2-} sharing X sites (Fig. 4.1). In this study, we investigated representative compositions, i.e., La_2LiHO_3 in the orthorhombic phase with ordered structures, Sr_2LiH_3O and $LaSrLiH_2O_2$ in the tetragonal phases. The tetragonal phase of La_2LiHO_3 is also investigated for H^- diffusion as a comparison. The structures of $LaSrLiH_2O_2$ and Sr_2LiH_3O were selected with the lowest GGA energies from 30 configurations, which have minimal electrostatic energies[155] out of 1000 symmetrically distinctive structures generated using *pymatgen*.[33, 111] For compositions of $La_{2-x}Sr_xLiH_{1-x}O_3$ and $La_{1-x}Sr_{1+x}LiH_{2-x}O_2$ with H^- vacancies, the corresponding number of vacancies at H^- sites was created in supercells (Table B1 in the Appendix), and the model structures were obtained using the same approach. The

structures with the lowest GGA energies were identified as ground-state structures for further calculations.

In order to study the site preference of H^-, we generated different hypothetical H/O anion sublattices of La_2LiHO_3, $LaSrLiH_2O_2$ and Sr_2LiH_3O with different numbers of H^- at apical sites (Fig. 4.1). For each number of apical-site H^-, the average GGA energy of those five structures with minimal electrostatic energies was calculated. In the case of $LaSrLiH_2O_2$, the same A-site sublattice of Sr^{2+} and La^{3+} in the $LaSrLiH_2O_2$'s ground state configuration was used.

4.2.2. Diffusion

We investigated the H^- diffusivity and conductivity in the oxyhydrides using *ab initio* molecular dynamics (AIMD) simulations. A minimal Γ-centered 1×1×1 *k*-point mesh and a time step of 2 fs were adopted in all non-spin-polarized calculations. The relaxed ground state structures were assigned an initial temperature of 100 K according to a Boltzmann distribution, and then they were heated to desired temperatures of 1000 K to 1800 K by velocity scaling over 2 ps. The AIMD simulations were performed for 200 to 400 ps in the NVT ensemble with a Nose-Hoover thermostat[156, 157] until the diffusion coefficient was converged. For the perfect structure with no H^- vacancy, a single H^- vacancy was introduced as a carrier with a compensating background charge. The H^- self-diffusion coefficient D was calculated by the mean square displacement (MSD) over time as in previous studies.[8, 33, 42] The directional diffusivity is obtained by the fitting of MSD in the corresponding direction over time.[42] The error bar of diffusivity was derived from

our established scheme based on the total diffusional displacements and effective ion hops during AIMD simulations.[158] Activation energies E_a were determined from Arrhenius plots of the diffusivity. Ionic conductivities were calculated according to the Nernst-Einstein relationship.[33, 43, 158] Estimating ionic conductivity using the Nernst-Einstein relationship based on the self-diffusion coefficient D is applicable to dilute and isolated mobile carriers. For the materials with strong correlation among ion hoppings,[43, 158, 159] the application of the Nernst-Einstein relationship should take into account the correlation factor, such as Haven ratio. The error bounds of E_a and conductivities were obtained from the error analysis of linear regression.[33, 158] The climbing-image nudged-elastic-band (CI-NEB)[160, 161] calculations were performed to determine the energy barrier of H^- vacancy migration. The migration pathway was extracted from the AIMD simulations. The forces of CI-NEB were converged within 0.05 eV/Å.

4.2.3. Substitution prediction

In order to increase H^- ionic conductivity in Sr_2LiH_3O, we considered acceptors substitution for A-site Sr^{2+} to create H^- vacancies. Candidate dopants M^+ for Sr^{2+} were suggested by the ionic substitution probability determined from the earlier study.[162] Sr_2LiH_3O supercells with four M^+ dopants and four H^- vacancies (i.e., $Sr_{32}M_4Li_{18}H_{50}O_{18}$) were constructed, corresponding to a H^- vacancy concentration of approximately 0.2 per formula unit ($Sr_{1.8}M_{0.2}LiH_{2.8}O$). The atomic configurations of A-site and anion sublattices after substitution were determined using the same ordering method in section 2.1.

4.3. Results

4.3.1. Structure and phase stability of the oxyhydrides

Through the ordering calculations, the ground-state structures with the lowest GGA energy of La_2LiHO_3, $LaSrLiH_2O_2$ and Sr_2LiH_3O were identified. We found the ground-state configurations of A-site Sr/La sublattice in $LaSrLiH_2O_2$, and X-site H/O sublattice in Sr_2LiH_3O does not exhibit particular symmetric ordering, in consistent with the experimental structures (Fig. 4.1).[5] The calculated lattice parameters for all three compounds using GGA functional were in agreement with the experimental values (Table B2).[5] In addition, the band gaps calculated using HSE06 functional are 3.15, 3.19 and 3.79 eV, for La_2LiHO_3, $LaSrLiH_2O_2$ and Sr_2LiH_3O respectively, indicating the oxyhydrides as wide-bandgap materials with limited electronic conductivity (Figure B1). The analyses of Born effective charge[152, 153] and Bader charge[163, 164] confirm the valence states of H^- and O^{2-} anions in these materials (Table 4.1, B3, B4 and B5). The differences between Born effective charges of the elements and their nominal ionic charges indicate the covalent bonding characters in the oxyhydrides, especially for La_2LiHO_3 and $LaSrLiH_2O_2$. The hydride ions in all other compositions with H^- vacancies ($x > 0$) are also confirmed using Bader charge (Table B6) and Born effective charge (Table B7). These charge analyses confirm the robustness of the oxyhydride chemistry and structure in maintaining hydride ions across a wide range of compositions.

Table 4.1. Born-effective-charge tensor (diagonal part) and Bader charge of each element in La_2LiHO_3, $LaSrLiH_2O_2$ and Sr_2LiH_3O.

	Born-effective-charge tensor									Bader charge		
	La_2LiHO_3			$LaSrLiH_2O_2$			Sr_2LiH_3O					
	xx	*yy*	*zz*	*xx*	*yy*	*zz*	*xx*	*yy*	*zz*	La_2LiHO_3	$LaSrLiH_2O_2$	Sr_2LiH_3O
H	-0.55	-0.94	-1.08	-0.84	-0.80	-1.07	-0.95	-0.95	-0.97	-0.64	-0.71	-0.74
O	-2.82	-2.34	-2.92	-2.68	-2.63	-2.60	-2.42	-2.42	-2.44	-1.37	-1.40	-1.48
Li	0.89	0.85	0.98	0.82	0.81	0.92	0.84	0.84	0.88	0.83	0.83	0.83
La	4.09	3.66	4.50	3.96	3.63	3.89	--	--	--	1.96	1.91	--
Sr	--	--	--	2.35	2.47	2.51	2.21	2.21	2.23	--	1.48	1.44

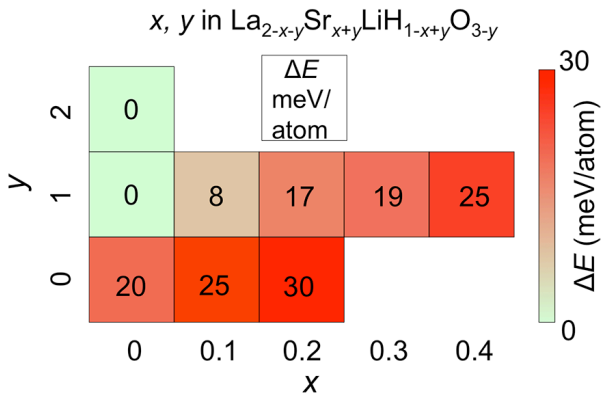

Figure 4.2. Energy above the hull ΔE of $La_{2-x-y}Sr_{x+y}LiH_{1-x+y}O_{3-y}$.

In addition, the phase stabilities described by the energy above the hull[165] ΔE of $La_{2-x-y}Sr_{x+y}LiH_{1-x+y}O_{3-y}$ composition were evaluated using the La-Sr-Li-H-O phase diagram based on GGA energies from the *Materials Project*[126] (Fig. 4.2). $LaSrLiH_2O_2$ and Sr_2LiH_3O are thermodynamically stable, and other oxyhydrides are slightly metastable at 0 K with small ΔE of ≤30 meV per atom. These small values of ΔE confirm the good phase stabilities of these $La_{2-x-y}Sr_{x+y}LiH_{1-x+y}O_{3-y}$ compositions in agreement with experiments.[5, 40] The thermodynamic phase equilibria of La_2LiHO_3 were calculated to be LiH and La_2O_3, which are the decomposed compounds

observed in the experiments.[5] A clear trend of the phase stability as a function of *x* and *y* in the compositions is observed. Increasing *y*, i.e., the mixing ratio of Sr_2LiH_3O over La_2LiHO_3, improves the phase stability while simultaneously increasing H^- content. Increasing *x*, i.e., increasing the H^- vacancy concentration via the Sr-to-La substitution, makes the structure less stable.

4.3.2. Site preference of H^- ions

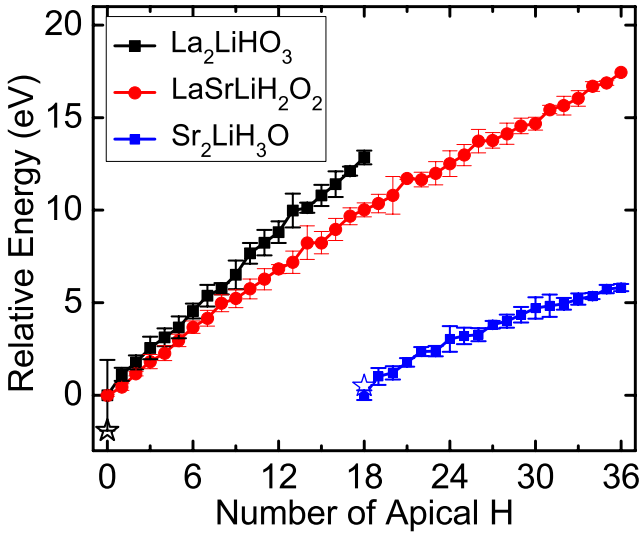

Figure 4.3. Relative energy of La_2LiHO_3, $LaSrLiH_2O_2$ and Sr_2LiH_3O with anion sublattice containing different numbers of H^- at apical sites, referenced to the minimum average energy. Each data point is an average GGA energy of five structures with the lowest Ewald energies, and the error bar refers to the maximum absolute deviation from the average GGA energy. The relative energy of ordered anion configuration of orthorhombic La_2LiHO_3 is shown in black star and is significantly lower than the minimum average energy. The relative energy of ordered

anion configuration (blue star) of Sr_2LiH_3O with alternating layers of apical-site O and H along the *c* axis is similar to the reference minimum average energy.

The K_2NiF_4 structure has two anion sites, i.e., the axial site and the apical site referenced to the BX_6 octahedra (Fig. 4.1). In $La_{2-x-y}Sr_{x+y}LiH_{1-x+y}O_{3-y}$, the anion sublattices of H^- and O^{2-} are tailored by the change of cation compositions *x* and *y*, and play a crucial role in H^- conduction. Our calculated ground state structures of La_2LiHO_3, $LaSrLiH_2O_2$ and Sr_2LiH_3O (section 4.3.1) show that H^- in the oxyhydrides preferably occupy axial sites than apical sites, in agreement with experimental characterizations.[40, 143] In order to reveal the origin of H^- site preference, we calculated energies of hypothetically generated structures of La_2LiHO_3, $LaSrLiH_2O_2$ and Sr_2LiH_3O with increased numbers of H^- at apical sites (section 4.2.1). The total energies of the structures increase with the number of H^- at apical sites, suggesting a strong energetic preference of H^- at axial sites in all three compositions. From the linear trend of relative energies on the number of apical-site H^- (Fig. 4.3), the average formation energies of activating an H^- from an axial site to an apical site are approximately 0.7, 0.5 and 0.3 eV in La_2LiHO_3, $LaSrLiH_2O_2$ and Sr_2LiH_3O, respectively. These high activation energies suggest limited formation of apical-site H^- ions due to thermally activation.

The high formation energies of apical-site H^- have electrostatic origin. The same trend is confirmed in the electrostatic energy from Ewald summation[155] of the entire lattice as a function of apical H^- numbers (Fig. B2). The Ewald energies show that swapping an apical-site H^- with an axial-site O^{2-} increases the electrostatic energy

of the lattice. In order to understand the origin of such site preference, we separate the electrostatic interactions into anion-anion interactions and cation-anion interactions. An axial anion is coordinated by eight nearest-neighbor anions within 3 Å, whereas an apical anion is surrounded by only four nearest-neighboring anions and four second nearest-neighboring anions from another BX_6 layer at > 3 Å (Fig. 4.1). For anion-anion interactions, anions with higher charges favor apical sites to avoid excessive anion-anion repulsion, thus having H^- at axial sites with higher anion-anion coordination number is energetically favorable than having O^{2-} at axial sites. For cation-anion interactions, both axial and apical anions are surrounded by six cations. The calculated Ewald energies from only cation sublattice show lower energy of axial-site anion than apical-site anion, i.e., favoring O^{2-} at axial sites (Table B8), which is opposite to the experimental structure and to the calculated trend from total electrostatic energies (Fig. B2). Therefore, the anion-anion electrostatic repulsion dominates the site energy differences, and the site preference of H^-/O^{2-} mainly comes from the electrostatic repulsion among anions. In section 4.3.3, we reveal the significant effect of the axial-site preferred H^- sublattice on H^- diffusion.

The energies of different anion configurations (Fig. 4.3) also explain the ordering tendency of the O/H anion sublattice in different compositions. The La_2LiHO_3 structure with ordered configuration of O/H anion sublattice (Fig. 4.1a) has significantly lower energy (black star in Fig. 4.3) than the average energy of five different anion configurations with lowest electrostatic energies, suggesting the ordered O/H anion lattice is energetically favorable in La_2LiHO_3. In Sr_2LiH_3O, the ordered O/H anion configuration (blue star in Fig. 4.3) with alternating layers of

apical-site O and H along the *c* axis has similar energy as the average energy of five different anion configurations with lowest electrostatic energies. Therefore, the ordered O/H anion configuration in Sr_2LiH_3O may not be energetically favorable, suggesting the tendency for anion disordering. These energetics from first principles calculations are in consistency with the ordered and disordered anion sublattice in La_2LiHO_3 and Sr_2LiH_3O, respectively.

4.3.3. Effects of cation substitution on H^- diffusion

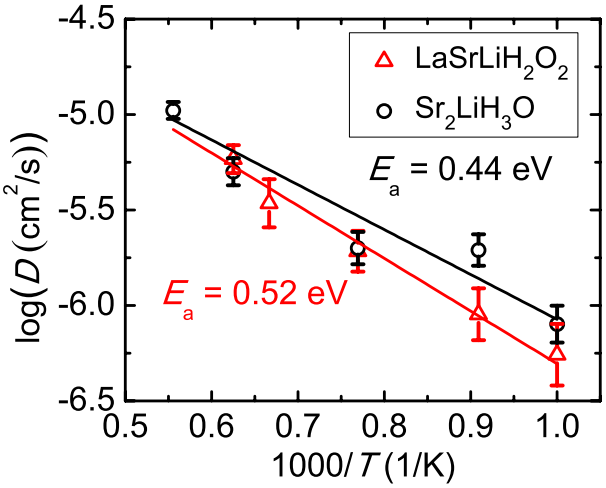

Figure 4.4. Arrhenius plot of H^- diffusion in $LaSrLiH_2O_2$ and Sr_2LiH_3O from AIMD simulations.

We performed AIMD simulations to study the H^- diffusion mechanism in La_2LiHO_3, $LaSrLiH_2O_2$ and Sr_2LiH_3O. Negligible H^- diffusion was observed in the absence of H^- vacancies for all three compositions. Fast H^- diffusion mediated by H^- vacancies is observed in $LaSrLiH_2O_2$ and Sr_2LiH_3O, but H^- diffusion in La_2LiHO_3 is too slow to be observed within the time scale of our AIMD simulations even up to

2300 K. H^- diffusion is observed in the tetragonal phase of La_2LiHO_3, but the H^- diffusion is too slow to obtain converged diffusivity even at 2000 K. $LaSrLiH_2O_2$ has an activation energy of 0.52 ± 0.04 eV, and an extrapolated H^- conductivity σ of 0.4 mS/cm (with an error bound of 0.2 to 0.9 mS/cm) at 573 K (Fig. 4.4). Sr_2LiH_3O has a slightly lower activation energy of 0.44 ± 0.08 eV and a higher conductivity σ of 2 mS/cm (with an error bound of 0.4 to 11 mS/cm) at 573 K. The calculated values of activation energies from AIMD simulations, though lower than experimental values of 0.76-0.79 eV, show the same relative trend as in experiments that Sr_2LiH_3O exhibit faster H^- diffusion than $LaSrLiH_2O_2$, and that La_2LiHO_3 shows the slowest H^- diffusion.[5]

Distinctive H^- diffusion mechanisms are observed in La_2LiHO_3, $LaSrLiH_2O_2$ and Sr_2LiH_3O in the AIMD simulations, as a result of different anion sublattices. Negligible H^- diffusion is observed in La_2LiHO_3, because the migration pathways between H^- sites are blocked by O^{2-} (Fig. 4.1). H^- migration in La_2LiHO_3 may happen through O vacancies or H^-/O^{2-} antisites, which may have high formation energies. Thanks to the connected H^- sublattice within the Li plane, $LaSrLiH_2O_2$ exhibits two-dimensional (2D) H^- diffusion migrating along the edges of LiH_4 squares in the *ab* plane (Fig. 4.5a). In all these materials, the migration of a single H^- ion mediated by H^- vacancy is observed as the dominant mechanism (Fig. B3), and the concerted migration of multiple H^- ions is rarely observed in contrast to many alkali-ion super-ionic conductors.[43] We performed CI-NEB calculations to investigate H^- vacancy migration along these pathways. The migration barriers range from 0.25 to 0.50 eV for different pathways with different local atomistic configurations, which are

denoted by the triangle of two A-site and one B-site ions (i.e., B-A-A with B as Li and A as La or Sr) that H^- passes through during migration (Fig. 4.5a). The Li-Sr-Sr pathway exhibits higher migration energies of 0.34 to 0.50 eV than those of Li-La-La and Li-Sr-La pathways (0.25 to 0.35 eV), and is likely the rate-limiting step for H^- diffusion in $LaSrLiH_2O_2$. Indeed, the migration barriers of Li-Sr-Sr pathways are in good agreement with the activation energy of 0.52 eV from AIMD simulations.

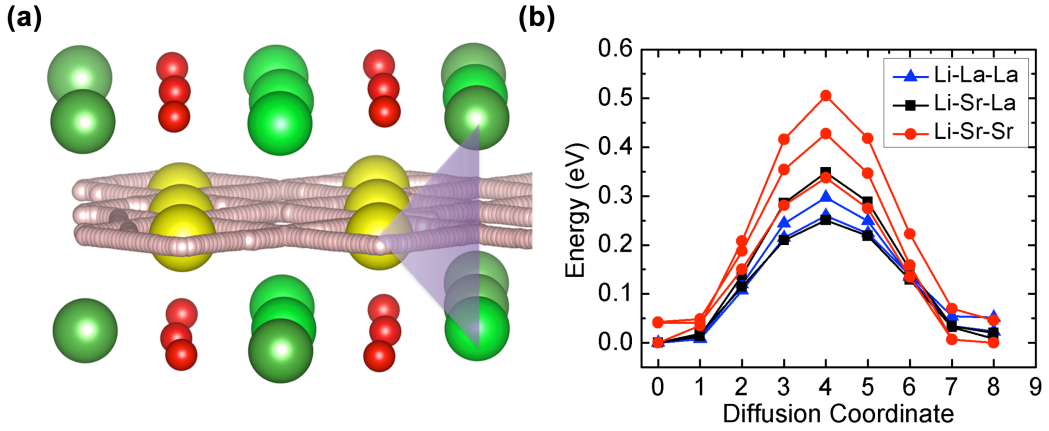

Figure 4.5. (a) The time-averaged trajectories of H^- ions in $LaSrLiH_2O_2$ from the AIMD simulations at 1600 K. The positions of mobile H^- (white spheres) are averaged over 2 ps and the initial positions of non-diffusing ions are shown. H^- migration pathway is through the purple triangle of B-A-A (B: Li; A: La or Sr) cations. (b) Energy profile of H^- migration along different pathways from CI-NEB calculations.

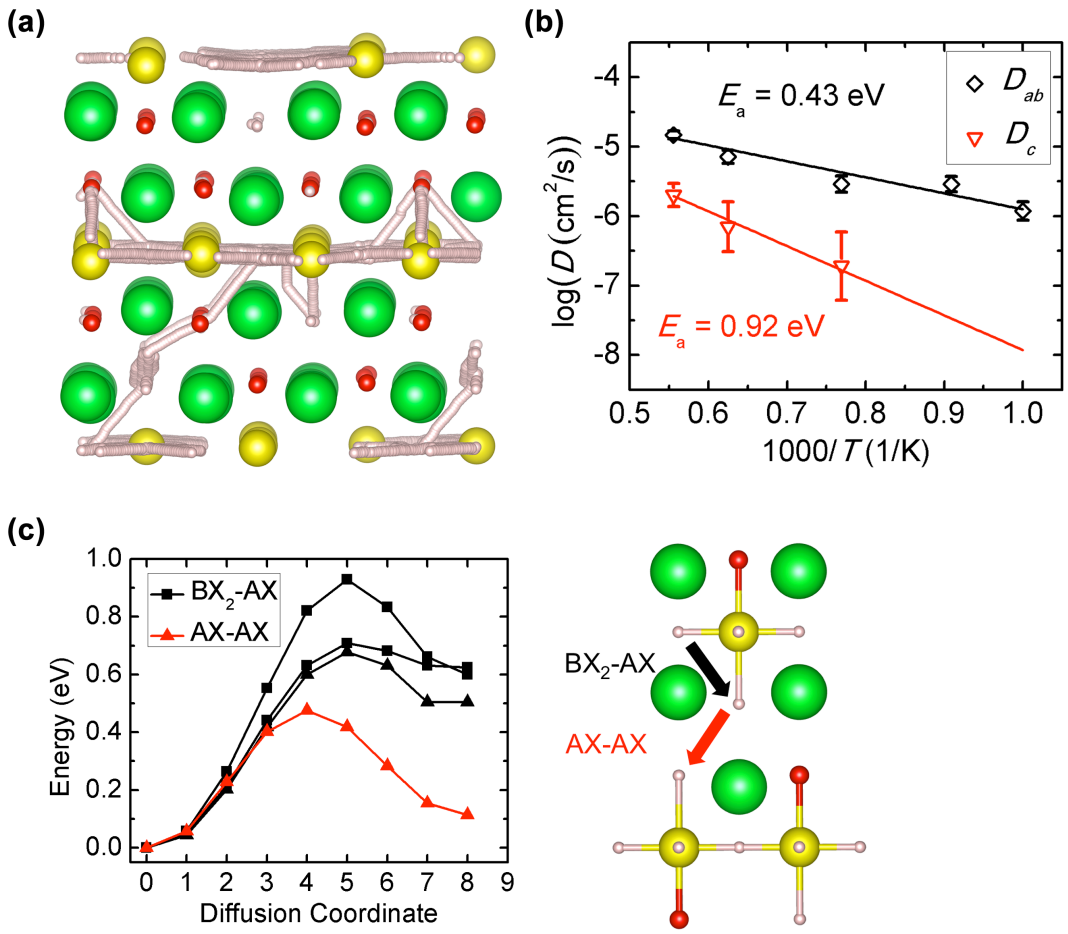

Figure 4.6. (a) The time-averaged trajectories of H^- in Sr_2LiH_3O from AIMD at 1300 K. The positions of mobile H^- (white spheres) are averaged over 2 ps and the initial positions of non-diffusing ions are shown. (b) Arrhenius plot of diffusivities along the *c* direction D_c and in the *ab* plane D_{ab}. (c) Inter-plane migration barriers for H^- vacancies along different pathways along the *c* direction, i.e., migrating between axial sites in the BX_2 plane and apical sites in the AX plane (BX_2-AX), and between apical sites in different AX planes (AX-AX). The structure in the subset shows two different inter-plane pathways.

Sr_2LiH_3O with higher H^- content than $LaSrLiH_2O_2$ exhibit 3D H^- diffusion (Fig. 4.6a). In addition to in-plane 2D diffusion similar to $LaSrLiH_2O_2$, inter-layer diffusion was observed between neighboring B-site Li layers. As quantified from AIMD simulations, the diffusivity D_{ab} in the *ab* plane is more than one order magnitude higher than D_c along the *c* direction (Fig. 4.6b). The H^- diffusion along the *c* direction has a significantly higher activation energy 0.93 ± 0.13 eV compared to 0.43 ± 0.08 eV in the *ab* plane. Therefore, H^- diffusion in Sr_2LiH_3O is anisotropic with facile in-plane diffusion and slower inter-plane diffusion.

The migration barriers calculated using CI-NEB methods (Fig. 4.6c) confirm the anisotropic H^- conduction in Sr_2LiH_3O, in agreement with AIMD simulations. The inter-layer diffusion consists of two consecutive hops, i.e., the BX_2-AX pathway from axial sites in the BX_2 plane to apical sites in the AX plane and AX-AX pathway between two apical sites in different AX planes (Fig. 4.6c). The BX_2-AX pathway has high migration energy barriers of 0.68 to 0.93 eV, and AX-AX pathway has the energy barrier of 0.48 eV. Therefore, the higher energy barrier of the BX_2-AX pathway causes slower H^- diffusion along *c* direction. This high migration barrier of BX_2-AX pathway is caused by the site preference of H^- at axial sites and by the higher site energy for H^- at apical sites. The CI-NEB calculations also confirm facile diffusion in the *ab* plane with migration energies ranging from 0.25 to 0.51 eV (Fig. B4). The migration energies of in-plane and inter-plane pathways calculated using CI-NEB methods are in good agreement with activation energies of D_{ab} and D_c from AIMD simulations.

The trend of activation energies and ionic conductivities for different compositions from our AIMD simulations is in good agreement with experiments,[5, 40] though the calculated ionic conductivity is higher than experimental measurements.[5, 40] This discrepancy may be attributed to the difference between ideal bulk-phase conductivity calculated in the AIMD simulations and the total conductivity measured from the experiments,[5, 40] which include contributions from both bulk phase and grain boundaries. The experiments reported that the activation energy decreases for the materials samples prepared under higher pressure with reduced grain boundaries.[5, 40] The bulk ionic conductivity is expected to be higher than the total conductivity. Another source of the discrepancy may be from the contribution of the formation energy of mobile H^- vacancies in these compounds (Fig. B5). Such formation energy may not be fully considered in the activation energies obtained from AIMD simulations, where H^- vacancies are pre-included into the model.

4.3.4. Effect of H^- vacancy concentration

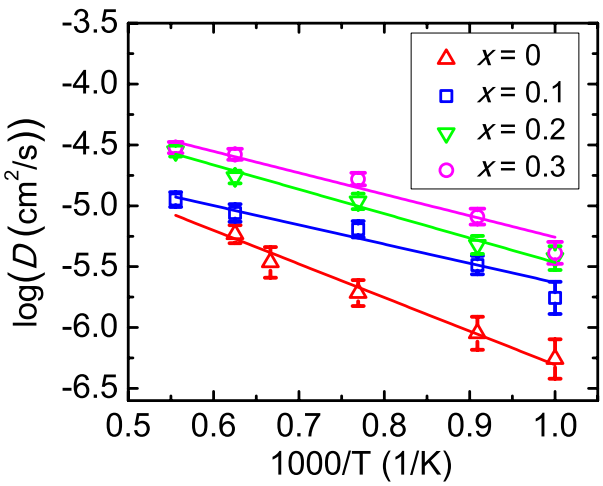

Figure 4.7. Arrhenius plot of H^- diffusivity in $La_{1-x}Sr_{1+x}LiH_{2-x}O_2$ (x = 0, 0.1, 0.2 and 0.3) from AIMD simulations.

Table 4.2. Diffusional properties of $La_{1-x}Sr_{1+x}LiH_{2-x}O_2$ (x = 0, 0.1, 0.2, 0.3).

Composition	E_a (eV)	σ at 573 K (mS/cm)	Error bound [σ_{min}, σ_{max}] (mS/cm)
$LaSrLiH_2O_2$ (x=0)	0.52 ± 0.04	0.4	[0.2, 0.9]
$La_{0.9}Sr_{1.1}H_{1.9}O_2$ (x=0.1)	0.34 ± 0.04	7	[3, 18]
$La_{0.8}Sr_{1.2}H_{1.8}O_2$ (x=0.2)	0.39 ± 0.03	8	[4, 14]
$La_{0.7}Sr_{1.3}H_{1.7}O_2$ (x=0.3)	0.38 ± 0.04	12	[4, 30]

Since H^- vacancies are mobile carriers in this class of oxyhydrides, H^- conductivity is increased by increasing the H^- vacancy concentration through the aliovalent substitution (Fig. 4.7 and Table 4.2). The AIMD simulations confirm the increase of H^- conductivities from 0.4 mS/cm to 12 mS/cm by increasing H^- vacancies from x = 0.0 to 0.3 in $La_{1-x}Sr_{1+x}LiH_{2-x}O_2$. The decrease of activation energy is also observed by increasing H^- vacancies. This trend of increasing conductivity with

respect to the concentration of H^- vacancies from our AIMD simulations is in agreement with the experiments.[5, 40] Therefore, high H^- vacancy concentration is a key for fast H^- conduction in these oxyhydrides.

4.3.5. New doped compositions for high H^- conductivity

Given the crucial role of H^- vacancies in H^- conduction, we predict new aliovalent doping to further increase H^- vacancies in Sr_2LiH_3O and to increase H^- conductivity. We tested the dopants M = Na^+, K^+, Rb^+, and Cs^+, for A-site Sr^{2+} substitution. The calculated energies above the hull ΔE of all doped compositions $Sr_{1.8}M_{0.2}LiH_{2.8}O$ (Table 4.3) show that aliovalent doping with increased vacancies destabilizes Sr_2LiH_3O, similar to the trend of Sr-to-La substitution (i.e., increasing H^- vacancies x) in La_2LiHO_3 and $LaSrLiH_2O_2$ (Fig. 4.2). Among these dopants, Na- and K-doped Sr_2LiH_3O have ΔE close to synthesized compounds (Table 4.3 and Fig. 4.2) and may probably be synthesized. In addition, our Born effective charge and Bader charge analyses confirm the valence state of H^- in these newly doped compounds (Table 4.3 and B9).

Table 4.3. Calculated properties of $Sr_{1.8}M_{0.2}LiH_{2.8}O$ (M = Na, K, Rb, Cs), compared with pure Sr_2LiH_3O.

Composition	Bader charge of H	ΔE (meV /atom)	E_a (eV)	σ at 573 K (mS/cm)	Error bound [σ_{min}, σ_{max}] (mS/cm)
Sr_2LiH_3O	-0.74	0	0.44 ± 0.08	2	[0.4, 11]
$Sr_{1.8}Na_{0.2}LiH_{2.8}O$	-0.75	24	0.34 ± 0.04	24	[11, 53]
$Sr_{1.8}K_{0.2}LiH_{2.8}O$	-0.74	23	0.37 ± 0.06	14	[3, 54]
$Sr_{1.8}Rb_{0.2}LiH_{2.8}O$	-0.75	31	0.39 ± 0.06	10	[3, 40]
$Sr_{1.8}Cs_{0.2}LiH_{2.8}O$	-0.75	41	0.46 ± 0.07	5	[1, 27]

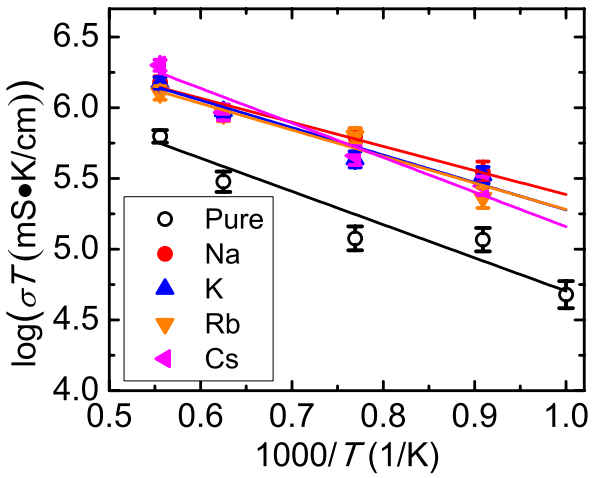

Figure 4.8. Arrhenius plot of $Sr_{1.8}M_{0.2}LiH_{2.8}O$ (M = Na, K, Rb, Cs) compared with Sr_2LiH_3O.

These predicted newly doped compounds were further studied for H^- diffusion via AIMD simulations (Table 4.3 and Fig. 4.8). We found all doped compounds exhibit higher ionic conductivities than that of pure Sr_2LiH_3O. Among all these doped compositions, $Sr_{1.8}Na_{0.2}LiH_{2.8}O$, $Sr_{1.8}K_{0.2}LiH_{2.8}O$ and $Sr_{1.8}Rb_{0.2}LiH_{2.8}O$ were

predicted to have significantly higher H^- conductivities and lower activation energies. In summary, A-site aliovalent doping, such as Na, K and Rb, for Sr_2LiH_3O is demonstrated as a viable strategy to increase H^- vacancy concentration and to increase H^- conductivity, though the ionic conductivity and activation energies predicted from the computation may not be quantitatively accurate due to the small supercell size, simplified cation-anion configurations, and high temperatures of the AIMD simulations.

4.4. Discussion

Our computation study confirms newly discovered H^- ion conductor based on the new $La_{2-x-y}Sr_{x+y}LiH_{1-x+y}O_{3-y}$ oxyhydride system and provides atomistic-scale understandings on the fast H^- conduction in this oxide anion conductor based on the K_2NiF_4-type structure. Through our computation insights, we reveal and highlight the origin of the K_2NiF_4-type structure in enabling its exceptional H^- conduction in oxides.

In the mixed anion system, the migration of non-O anion conduction is often blocked by O^{2-} sublattice.[146, 147] As observed in our AIMD simulations of La_2LiHO_3 and $LaSrLiH_2O_2$, O^{2-} ions sharing the same anion sites block H^- conduction in La_2LiHO_3, and impede the inter-layer 3D conduction in $LaSrLiH_2O_2$. As revealed in our computation, the H^- diffusion mechanism transitions from negligible H^- conduction, to 2D diffusion, and to 3D diffusion, as the anion sublattices are tuned through a wide range of compositions from La_2LiHO_3, $LaSrLiH_2O_2$ to Sr_2LiH_3O. In the K_2NiF_4-type structure, two types of anion sites have different local coordination,

leading to different site energies and the site preference of H^- at axial sites over O^{2-}. As a result, in $LaSrLiH_2O_2$ with decent H^- concentration, H^- percolates all axial sites and form 2D planar H^- sublattice in the *ab* plane forming 2D diffusion and excluding O^{2-} to separate planes. Therefore, this unique two-anion-site sublattice with strong site preferences resolve the common issue of O^{2-} blocking in mixed anion systems.

Another advantage of this K_2NiF_4 structure and $La_{2-x-y}Sr_{x+y}LiH_{1-x+y}O_{3-y}$ oxyhydride system is the robust and tunable sublattices, which are essential to induce high H^- content for high H^- conductivity. Our computation confirms the good stability and chemistry robustness of this highly tunable cation and anion lattice for a wide range of compositions from La_2LiHO_3 to Sr_2LiH_3O in the K_2NiF_4 structure. In addition to the use of highly positive cations to maintain H^- as anions across a wide range of compositions, two sets of anion sublattices in the K_2NiF_4 structure facilitate the highly tunable lattice with good stability to achieve high H^- content in many oxyhydrides such as $La_{2-x-y}Sr_{x+y}LiH_{1-x+y}O_{3-y}$ and $LaSrCoO_3H_{0.7}$.[143] Due to the existence of apical anion sublattice vs. axial anion sublattice with different local coordination and site energies, the structural framework allows high concentration of two anions, which occupy two sublattices respectively. This separation of anion sublattice helps the stability of the structures. In contrast, previously studied H^- conductors based on perovskite structure, such as $ATiO_{3-x}H_x$ (*A*: Ba, Sr, Ca) and $SrTi_{1-x}Fe_xO_{3-x}$, suffered low H^- concentrations[146, 147] ($x < 0.6$) due to limited structural stabilities. In the perovskite structure with only one anion sublattice, a high concentration of H^- substituting O^{2-} sublattice would cause significant distortion and energy penalty, leading to poor structural stability and limited H^- content.[146]

This K_2NiF_4 structure provides an exciting opportunity to enable oxide-based anion conductors. Therefore, the understanding of these unique features in K_2NiF_4 structure provides valuable guidance for the future selection of potential framework for oxide-based anion conductors. The unique two-anion-site features of the K_2NiF_4 structure framework can be generalized in designing and discovering new oxide anion conductors. The new structure with two sets of anion sites may have highly tunable lattices and may minimize the blocking effect of the other anion sublattice, allowing high carrier concentration and good diffusion network.

4.5. Conclusions

We studied H^- diffusion mechanism and its relationship with tunable lattice in $La_{2-x-y}Sr_{x+y}LiH_{1-x+y}O_{3-y}$ oxyhydrides using first principles calculations. Our computation study confirmed the good stability and chemistry robustness of the new oxyhydrides with K_2NiF_4 structure. The computation revealed the origin of different site energies and the site preference of H^- and O^{2-} in the structure, and identified the transition of H^- diffusion mechanism from negligible diffusion to 2D and to 3D diffusion as the composition changes from La_2LiHO_3 to $LaSrLiH_2O_2$ and to Sr_2LiH_3O. The fast H^- diffusion is mediated by H^- vacancies, and increasing H^- vacancies through aliovalent doping such as Na, K and Rb in Sr_2LiH_3O is computationally predicted to enhance H^- ionic conductivity while maintaining reasonable phase stability. Through our computation results, general understanding and design guideline for further research of novel promising anion conductors based on oxides are achieved.

Chapter 5: Effect of carrier defects on Li-ion diffusion in Li_6KTaO_6

5.1. Introduction

As introduced in the introduction section, all-solid-state Li-ion batteries (ASLIBs) using solid electrolytes (SEs) are regarded as promising alternatives to current Li-ion batteries using organic liquid electrolytes. Since the performance of ASLIBs can be further improved by using superionic conductors (SICs) as SEs, it is of scientific interest to design and discover novel SICs with high ionic conductivities. While some SICs (e.g., $Li_7P_3S_{11}$,[52] Li_3YCl_6 and Li_3YBr_6[53]) exhibit inherently high Li^+ conductivity at their perfect compositions, superionic conduction in many materials should be activated in specific Li-ion sublattice configuration by introducing extrinsic carrier defects (i.e., Li^+ vacancies or interstitials) through aliovalent doping. The vacancy promotion effect on ionic conductivity is attributed to the vacancy-mediated isolated ion hopping based on the classical diffusion model.[12, 68, 166] The introduction of vacancies mediates the hopping of individual ions among lattice sites through the interconnected diffusion channels.[68] In contrast to the isolated ion hopping induced by vacancies, inserting extra Li^+ to occupy interstitial sites of pristine materials leads to superionic conduction in many SICs (e.g., NASICON $Li_{1+x}Al_xTi_{2-x}(PO_4)_3$, $Li_{1+x}Ta_{1-x}Zr_xSiO_5$ and $Li_{1+x}Al_{1+x}Si_{1-x}O_4$) by activating the concerted migration of multiple Li^+ with low activation energies.[19, 68] Strong coulombic interactions induced by excess interstitials lead to the concerted migration

of multiple Li^+ with low migration barriers. Therefore, different extrinsic carrier defects can expedite Li^+ diffusion via distinctive mechanism.

In addition to distinctive diffusion mechanisms, the incorporation of vacancies or interstitials has different enhancement effects on Li^+ transport in one host material. For example, $LiZnPS_4$ with Li^+ excess as $Li_{1.7}Zn_{0.65}PS_4$ demonstrated an ionic conductivity of 0.13 mS/cm at room temperature (RT) in experiments, which is four order magnitudes higher than that of $LiZnPS_4$ with vacancies.[55, 167] Li^+ interstitials play a key role to activate the superionic conduction in $LiZnPS_4$. In contrast to $LiZnPS_4$, the introduction of Li^+ vacancies in Li_3OCl as $Li_{2.9}OCl_{0.9}$ exhibited the conductivity of 0.85 mS/cm at RT, which is higher than 2×10^{-4} mS/cm of $Li_{3.1}O_{1.1}Cl_{0.9}$ with interstitials.[12] Thus, the incorporation of different carrier defects leads to different Li^+ conductivity, which may originate from the different mechanisms they induced. Understanding why certain extrinsic carrier defects can activate superionic conduction in materials is important for the design of SICs. To understand the origin of the distinctive effects from vacancies or interstitials on Li^+ transport, it is necessary to elucidate and contrast the diffusion mechanisms induced by different extrinsic carriers defects in one host material. However, relevant studies to contrast effects of various carrier defects on ionic diffusion are rather limited. Uncovering roles of extrinsic carrier defects on ionic diffusion would provide a crucial insight for the optimization and design of novel SEs.

Herein, I theoretically investigated the mechanism of Li ionic conduction in Li_6KTaO_6, a new material structure which has not been studied for Li-ion diffusion. Li_6KTaO_6 was firstly synthesized and characterized by R. Hoppe *et al.* with a

rhombohedral structure (space group: $R\bar{3}m$).[168, 169] The structural framework of Li_6KTaO_6 consists of LiO_4 tetrahedra, which share edges with TaO_6 octahedra and faces with KO_{12} polyhedrons, respectively (Fig. 5.1a). The high Li^+ concentration and well-connected diffusional channels enable Li_6KTaO_6 as a potential SIC. To best of my knowledge, the Li^+ diffusion of Li_6KTaO_6 has never been studied.

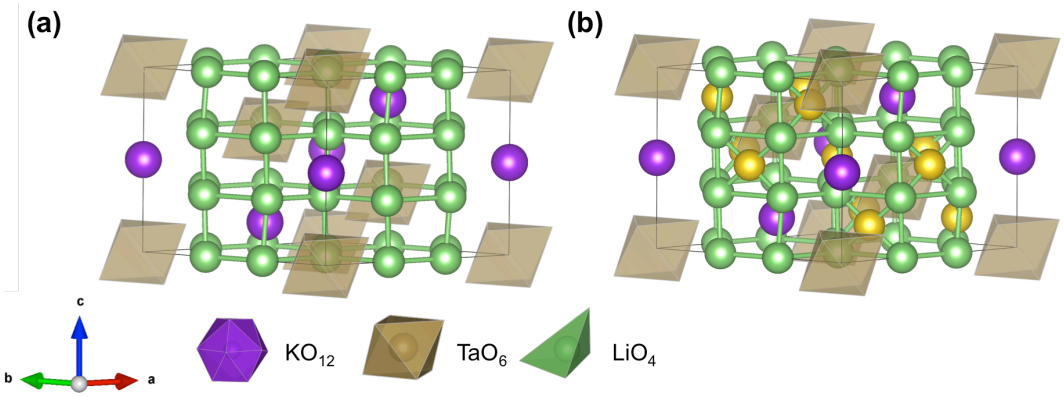

Figure 5.1. Crystal structure of (a) Li_6KTaO_6 and (b) $Li_{6+x}KTaO_6$ with computationally predicted interstitial sites (shown as yellow spheres) in a unit cell. Li_6KTaO_6 comprises TaO_6 octahedra (brown), KO_{12} polyhedrons (purple) and LiO_4 tetrahedra (green). Green bars represent the connection between Li sites.

In this chapter, I demonstrate Li_6KTaO_6 as a promising SE by investigating its crystal structure, stabilities, and ionic diffusion using first principles calculations. We first studied stabilities of Li_6KTaO_6 and quantified its electrochemical window. Then, we revealed distinctive diffusion mechanism in Li_6KTaO_6 when introducing different carrier defects, and found inserting Li^+ interstitials through doping enables Li_6KTaO_6 as a SIC with high conductivity > 1 mS/cm at 300 K. In addition, we performed high-throughput computational screening for a wide range of compositions in the

Li_6KTaO_6 structure, and predicted a group of new compositions in the material family of Li_6KTaO_6 as SICs. Our study highlights the role of extrinsic carrier defects on diffusion, and demonstrate the computational capability to predict completely novel SE systems.

5.2. Methods

All density function theory (DFT) calculations were performed using the projector augmented-wave (PAW)[56] approach used in the Vienna Ab initio Simulation Package (VASP).[57] Perdew-Burke-Ernzerhof (PBE) generalized-gradient approximation (GGA) function was used in all total energy calculations.[58] Parameters in spin-polarized static DFT calculations were consistent with the *Materials Project*,[59] which enable total energies converged to 1 meV per atom. The band gap calculations were performed using the standard Heyd-Scruseria-Ernzehof (HSE06)[60, 61] hybrid functional with a *k*-point mesh as 500 per atom. PBEsol[63] functional was adopted in calculating phonon dispersion and elastic tensor of Li_6KTaO_6, as PBE functional often overestimates lattice constants that affect vibrational frequencies and mechanical properties (Table C1 in the Appendix).[170] Phonon calculations were performed using a finite displacement approach implemented in Phonopy code.[62] Elastic constants of Li_6KTaO_6 were calculated by performing six finite distortions (0.015 Å) on the lattice implemented in VASP.[171]

5.2.1 Li site and structures

Topological analysis was applied to identity potential Li interstitial sites in Li_6KTaO_6 following the established methods using the Voronoi-Dirichlet partition algorithm implemented in Zeo++.[172, 173] A supercell model consisting of $\sqrt{2}\times\sqrt{2}\times2$ unit cells (12 formula unites) were used for doped compositions. Dopants, i.e., Ba^{2+} for K^+ and Zr^{4+} (or Sn^{4+}) for Ta^{5+}, were suggested by the ionic substitution probability determined from earlier studies.[162] Structures of doped compositions were selected with the lowest GGA energies out of 20 configurations, which have minimal electrostatic energies from 2000 symmetrically distinct structures ordered by *pymatgen*.[33] Those structures with the lowest energies were regarded as ground-state configurations for further analysis.

5.2.2 Diffusion

We performed ab initio molecular dynamics (AIMD) simulations to investigate Li^+ diffusion. We adopted a single Γ-centered *k*-point mesh and a time step of 2 fs in the nonspin-polarized calculations. An initial temperature of 100 K was assigned to relaxed structures, and we increased the temperature to a targeted value by velocity scaling for 2 ps. The AIMD simulations were performed from 100 to 500 ps in the NVT statistical ensemble[156, 157] until the diffusivity achieved convergence.[174] The ionic diffusivity, conductivity and activation energies were computed based on the established methods in previous studies.[4] Li^+ migration barriers were calculated by the climbing-image nudged (CI-NEB) methods.[160, 161] Li^+

diffusion pathways were extracted from AIMD simulations. The convergence criterion of CI-NEB calculations was 0.05 eV/ Å.

5.2.3 Substitution prediction for new compositions

In order to acquire more promising compounds with superionic conduction, we explored the new set of Li_6ABO_6 family by substituting Li_6KTaO_6. The most exhaustive method to generate candidate Li_6ABO_6 compounds is to consider all 89 elements as potential cations, which yields ~7000 possibilities. However, computing all possible structures is computationally expensive. We further select candidate compounds by satisfying the charge balance and the Pauling's radius ratio's rule,[175] which are regarded as criterion to construct stable structures. Cations at the A site coordinated with twelve O^{2-} or the B site with sixfold coordination are expected to be larger than 1.26 Å or 0.52 Å, respectively, with a radius of O^{2-} as 1.26 Å using the Shannon crystal ionic radius.[176] We then evaluated phase stabilities of those selected compounds. Stable compounds were further analyzed by AIMD simulations after Sn^{4+} doping at B sites. The atomic configurations of doped compounds were obtained using the same approach in section 5.2.1.

5.3. Results

5.3.1 Crystal structure of Li_6KTaO_6

Li_6KTaO_6 has a rhombohedral structure (space group: $R\bar{3}m$) comprising of connected LiO_4 tetrahedra (Fig. 5.1a). The hexagonal Li sublatice (Fig. 5.1a) provides a decent three-dimensional (3D) percolation network connected by nearest Li ions

with the distance of 2.4 Å. The calculated lattice parameters using GGA-PBE functionals are in agreement with experimental values (Table C1).[168] In addition, we employed topological analysis to find large space with suitable chemical environments to accommodate more Li^+ in the framework of Li_6KTaO_6. The topological analysis has reproduced the experimentally characterized Li tetrahedra site, validating our analysis scheme (Fig. 5.1b). The agreement demonstrates the intrinsic relationship between Li sublattice and crystal structural framework. In addition to the lattice site, an octahedral site, neighboring four Li lattice sites, is identified as a new potential Li interstitial site (Fig. 5.1b). It is noted that the interstitial sites are located at the face center of the planes formed by four Li lattice sites except for the planes facing K^+ (Fig. 5.1b), as K^+ with large ionic radius reduce the space to accommodate Li^+. The diagonal channels connected by alternating Li interstitial sites provide a new 3D diffusion network with a shortened nearest Li-Li distance as 1.8 Å.

5.3.2 Stability Properties

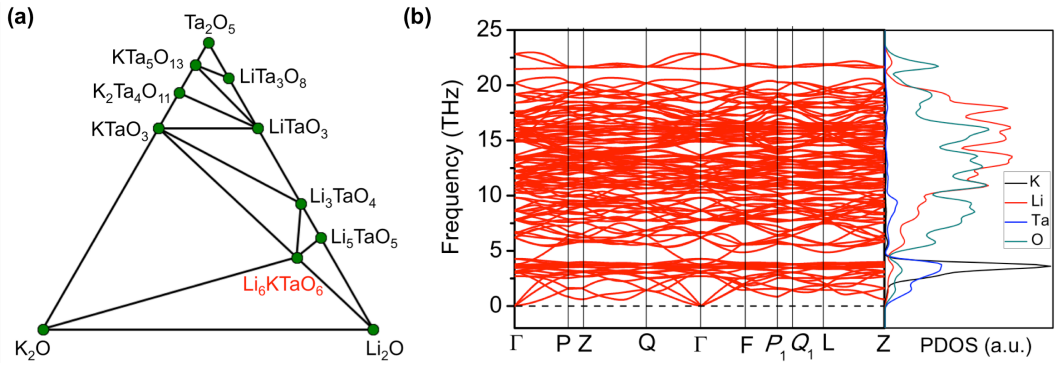

Figure 5.2. (a) Pseudoternary Ta_2O_5-K_2O-Li_2O phase diagram based on GGA energies at 0 K from the Li-K-Ta-O compositional space. (b) Phonon dispersion and corresponding partial density of states of Li_6KTaO_6 in a unit cell.

The stability of Li_6KTaO_6 was evaluated by investigating its thermodynamic and dynamic stabilities. Based on the calculated phase diagram at 0 K, Li_6KTaO_6 is thermodynamically stable (Fig. 5.2a), confirming the good synthesizability in experiments. The formation energy of Li_6KTaO_6 from K_2O, Li_2O and Ta_2O_5 is as low as -2.78 eV/f.u (Fig. 5.2a), corresponding well to the actual experimental synthesis that utilizes K_2O, Li_2O and Ta_2O_5 as reactants (Fig. 5.2a).[168] Moreover, the lack of imaginary modes in the vibrational spectrum indicate Li_6KTaO_6 is dynamically stable (Fig. 5.2b).

In addition to phase stability, mechanical properties can influence the fabrication and performance of SEs in ASLiBs. Therefore, we calculated the elastic tensors and other derived mechanical properties of Li_6KTaO_6 (Table 5.1 and Table C2). The elastic tensor of Li_6KTaO_6 satisfies the Born elastic stability criterion[177, 178] for rhombohedral structures, i.e.,

$$C_{11} > |C_{12}|, C_{44} > 0, C_{13}^2 < \frac{1}{2}C_{33}(C_{11} + C_{12}), C_{14}^2 < \frac{1}{2}C_{44}(C_{11} - C_{12}),$$

indicating the mechanical stability of Li_6KTaO_6. In addition, electrolyte materials should have good ductility to maintain the intimate contact between electrodes and electrolytes. While the bulk modulus *B* of a material associated with bond strength can represent the opposition to fracture, the shear modulus *G* can reflect the resistance to plastic deformation. Thus, Pugh proposed the ratio *B/G* as an indicator to evaluate the ductility of materials by summarizing experimental data, i.e., ductility of materials is associated with a large *B/G* value.[179] The *B*/*G* ratio of Li_6KTaO_6 (1.9) is higher

than those of $LiTi_2(PO_4)_3$ (NASICON) and Li-stuffed garnet (Table 5.1),[170] suggesting its good ductility as a SE.

Table 5.1. Calculated bulk modulus (*B*), shear modulus (*G*), Young's modulus (*E*) and the ratio of *B*/*G* of Li_6KTaO_6 compared with those of $LiTi_2(PO_4)_3$ (NASICON), t-$Li_7La_3Zr_2O_{12}$ and Li metal under the Voigt-Reuss-Hill approximation.[170, 180]

Material	*B* (GPa)	*G* (GPa)	*E* (GPa)	*B/G*
Li_6KTaO_6	100.3	51.8	132.3	1.9
$LiTi_2(PO_4)_3$	95.0	57.6	143.7	1.6
t-$Li_7La_3Zr_2O_{12}$	127.4	68.9	175.1	1.8
Li	13.7	4.6	12.4	3.0

5.3.3 Electrochemical stability of Li_6KTaO_6

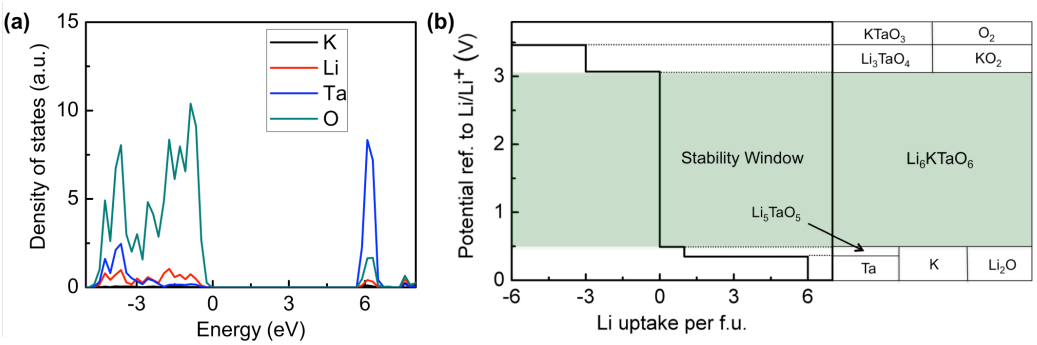

Figure 5.3. (a) Calculated electronic partial density of states of Li_6KTaO_6 using HSE06 functional. (b) Calculated voltage profile and corresponding phase equilibria of Li_6KTaO_6 with respect to the Li uptake and extraction processes.

We evaluated the electrochemical stability of Li_6KTaO_6 by calculating its bandgap and thermodynamic electrochemical window. The calculated bandgap of Li_6KTaO_6 using HSE06 functional is 5.74 eV (Fig. 5.3a), indicating its low electronic conductivity as an electrolyte. The large bandgap of Li_6KTaO_6 is comparable to those

of known SEs such as LLZO (6.4 eV),[181] Li_3OBr (5.84 eV)[53] and LGPS (3.6 eV),[42] and provides a high intrinsic upper limit for electrochemical stability window using inert electrodes.

Thermodynamic electrochemical stability of Li_6KTaO_6 was further evaluated by constructing the Li grand potential phase diagram (Fig. 5.3b). Li_6KTaO_6 exhibits a wide electrochemical stability window with 3.07 V as an anodic limit and 0.50 V as a cathodic limit referenced to Li/Li^+ (Fig. 5.3b), respectively. This electrochemical stability window is wider than those of many SEs, e.g., LGPS (1.72-2.29 V), Li_3PS_4 (1.71-2.32 V), and LIPON $Li_{2.98}PO_{3.3}N_{0.46}$ (0.69-1.07 V).[50, 182] In spite of the low cathodic limit of Li_6KTaO_6 (0.5 V), it is still unstable against Li metal with the phase equilibria as Ta, K and Li_2O at 0 V (Fig. 5.3b). However, the reaction energy of Li_6KTaO_6 against Li is smaller (-0.16 eV/atom) than those of many SEs, e.g., LLTO $Li_{0.33}La_{0.56}TiO_3$ (-0.34 eV/atom) LATP (-1.56 eV/atom), and LiPON (-0.62 eV/atom).[50, 182] The decomposition against Li metal anode can be reduced by utilizing Li-In alloy as anodes with a higher potential (~0.6 V),[183] or coating the interface with Li_2O. As for the oxidation stage, the final oxidation reaction of Li_6KTaO_6 involves the gas release with the phase equilibria as O_2 and $KTaO_3$ (Fig. 5.3b). The gas involving reactions were observed to exhibit sluggish kinetics in many oxides SEs, e.g., LLZO, LLTO and LATP.[50, 182] Thus, we expect the good stability of Li_6KTaO_6 against oxidation at high potentials due to the kinetic limitations in oxidation reaction involving oxygen gas evolution.

5.3.4 Effect of cation substitution on Li^+ diffusion

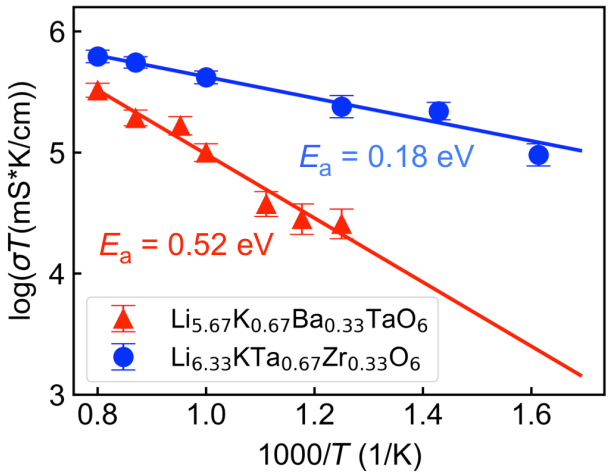

Figure 5.4. Arrhenius plots of Li^+ diffusion in $Li_{5.67}K_{0.67}Ba_{0.33}TaO_6$ and $Li_{6.33}KTa_{0.67}Zr_{0.33}O_6$ from AIMD simulations.

Exhibiting high ionic conductivity (> 0.1 mS/cm at 300 K) is a predominant requirement for SEs used in ASLIBs. We performed AIMD simulations to study Li^+ conductivity in Li_6KTaO_6. However, Li^+ diffusion in perfect Li_6KTaO_6 was too slow to obtain the converged diffusivity during the time scale of AIMD simulations. The negligible Li^+ transport in pristine Li_6KTaO_6 suggests the need of extrinsic Li^+ carriers to accelerate the Li^+ diffusion as needed by many SICs, e.g., $Li_{3-x}OCl_{1-x}$, LATP and $Li_{1+x}Ta_{1-x}Zr_xSiO_5$.[19, 68]

In order to elucidate roles of carrier defects on Li^+ diffusion in Li_6KTaO_6, we consider two types of Li point defects as carriers, i.e.,V'_{Li} and Li_i with low defect formation energies (Fig. C1). Then, we incorporated V'_{Li} and Li_i into Li_6KTaO_6 by doping the pristine composition to form $Li_{5.67}K_{0.67}Ba_{0.33}TaO_6$ and $Li_{6.33}KTa_{0.67}Zr_{0.33}O_6$, respectively. Both $Li_{5.67}K_{0.67}Ba_{0.33}TaO_6$ and $Li_{6.33}KTa_{0.67}Zr_{0.33}O_6$ have small energies above hull[64] ΔE of 16 and 18 meV per

atom, respectively, suggesting the good synthesizability in experiments. In contrast to the negligible diffusion in perfect Li_6KTaO_6, both $Li_{5.67}K_{0.67}Ba_{0.33}TaO_6$ and $Li_{6.33}KTa_{0.67}Zr_{0.33}O_6$ exhibit improved conductivities (Fig. 5.4). While $Li_{5.67}K_{0.67}Ba_{0.33}TaO_6$ has an activation energy of 0.52 ± 0.04 eV, and an extrapolated σ of 4×10^{-4} mS/cm (with an error range from 3.7×10^{-5} to 1.3×10^{-3} mS/cm) at 300 K (Fig. 5.4), $Li_{6.33}KTa_{0.67}Zr_{0.33}O_6$ exhibits a significantly reduced activation energy of 0.18 ± 0.02 eV, and a significantly larger σ of 12 mS/cm (with an error range from 6 to 26 mS/cm) at 300 K (Fig. 5.4). Introducing carrier defects (i.e., lithium vacancies or interstitials) to Li_6KTaO_6 results to distinct enhancement on ionic conduction. Li excess enables the superionic conduction in Li_6KTaO_6 with competitive ionic conductivities among current best oxide SEs, such as cubic LLZO (0.1-1 mS/cm) and LATP (~1 mS/cm).[43]

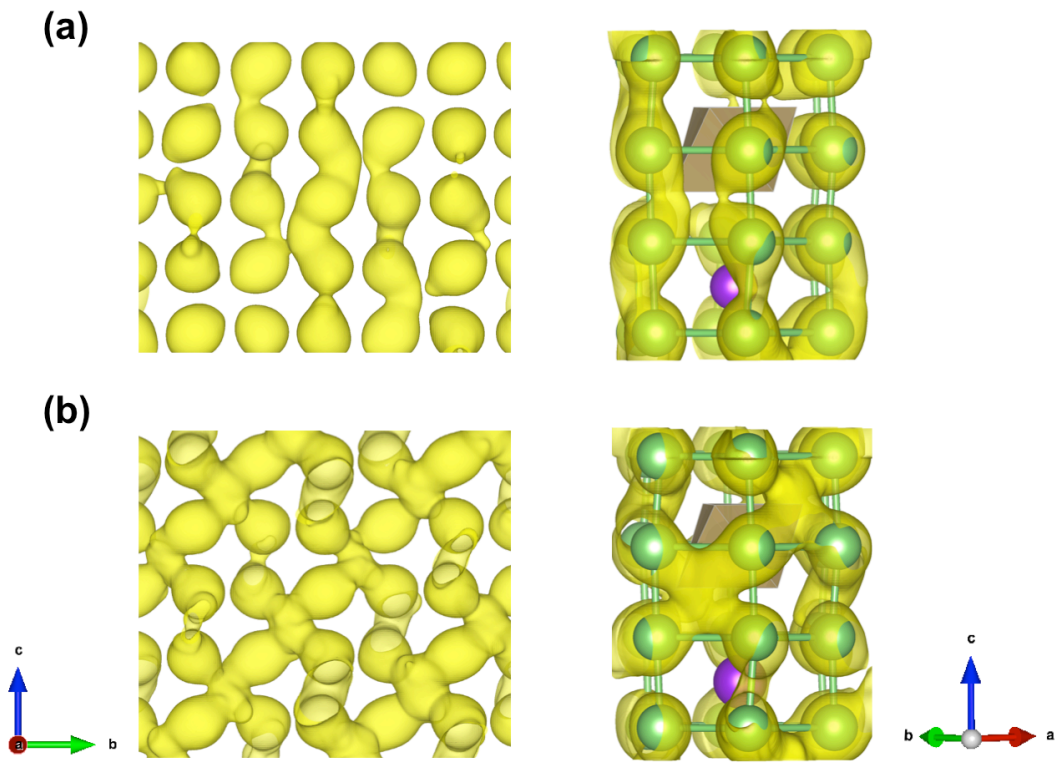

Figure 5.5. Li^+ probability densities of (a) $Li_{5.67}K_{0.67}Ba_{0.33}TaO_6$ and (b) $Li_{6.33}KTa_{0.67}Zr_{0.33}O_6$ viewed in supercells and the hexagonal Li sublatice from AIMD simulations at 800 K, respectively. The isosurface refers to $0.1\rho_0$, where ρ_0 indicates the average Li^+ density probability in each structure from entire AIMD simulations.

Li^+ transport induced by vacancies. Different carrier defects induced distinct Li^+ diffusion mechanisms in Li_6KTaO_6. The migration of single Li^+ mediated by vacancy was observed as the dominant mechanism in $Li_{5.67}K_{0.67}Ba_{0.33}TaO_6$, which can be confirmed by the van Hove correlation function and Li^+ dynamic analysis (Fig. C2). As quantified by directional diffusivities (Fig. C3), Li^+ diffusion in $Li_{5.67}K_{0.67}Ba_{0.33}TaO_6$ is anisotropic with the dominant *c*-axis diffusion channels (Fig. 5.5a), where single jumps often happen between nearest Li sites along the *c* direction (Fig. 5.5a). The lower diffusivity of Li^+ in *ab* plane results from the blocking of diffusion network in TaO_6 planes, which can be viewed from the Li^+ probability

density with lower isovalue in Fig. C4. Although Li^+ diffusion forms a honeycomb pattern around Ta sites in the *ab* plane, Li^+ cannot diffuse around K sites leading to a blocking of diffusion network in TaO_6 planes (Fig. C4). The long-range percolation of the *ab* plane needs the *c*-direction diffusion to bridge TaO_6 planes (Fig. 5.1).

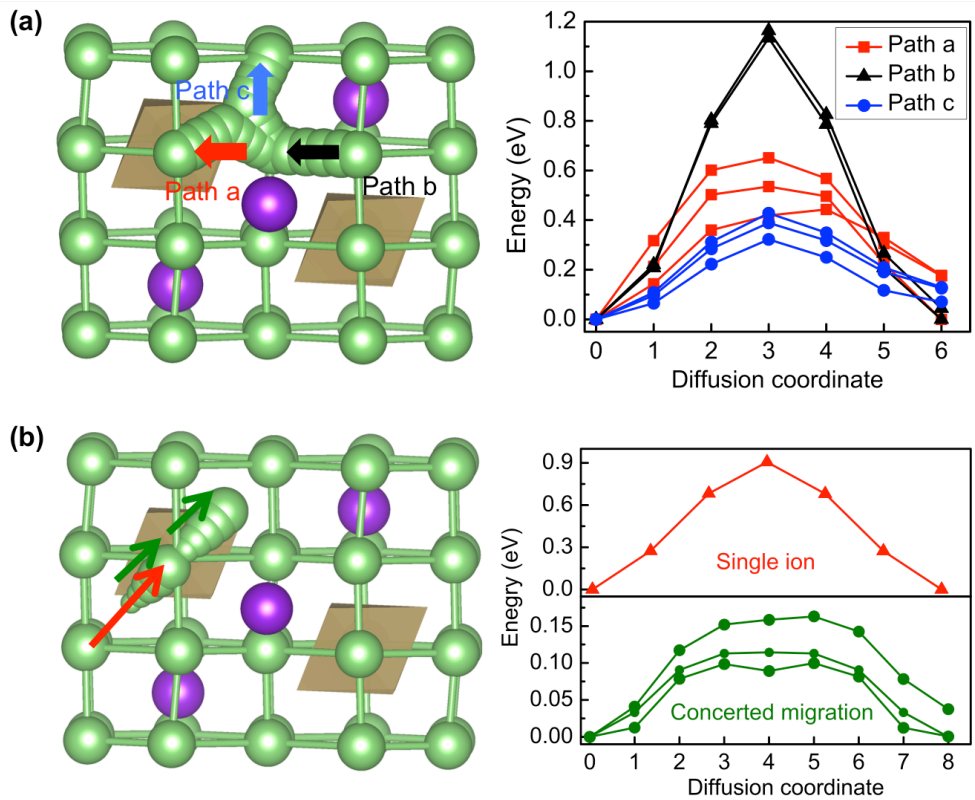

Figure 5.6. Li^+ migration trajectories and corresponding energy barriers from CI-NEB calculations in (a) $Li_{5.67}K_{0.67}Ba_{0.33}TaO_6$ along different pathways by single-ion hopping, and in (b) $Li_{6.33}KTa_{0.67}Zr_{0.33}O_6$ with concerted migration of two Li^+ hopping in pair, and the energy landscape from single Li^+ along the pathway.

The migration energies calculated by CI-NEB confirm the single-ion hopping mechanism in $Li_{5.67}K_{0.67}Ba_{0.33}TaO_6$ (Fig. 5.6a). Migration energies of pathways a, b and c are 0.42-0.65, 1.13-1.16 and 0.32-0.43 eV, respectively, confirming the

anisotropic diffusion induced by vacancies. CI-NEB calculations confirm the high diffusion barriers around K sites (path b), which lead to the blocking of diffusion in the TaO_6 plane observed in AIMD simulations (Fig. C4). The high migration barrier of path b has the structural origin, which can be revealed by the migration trajectory from CI-NEB calculations. While the geometry of the pathways a and c exhibit a curve towards the interstitial sites with large size void of atoms or bonds (Fig. 5.1b, 5.5a and 5.6a), Li^+ migrate straightly along the pathway b with high barriers due to the lack of interstitial sites.

Li^+ transport induced by interstitials. In contrast to the anisotropic diffusion in $Li_{5.67}K_{0.67}Ba_{0.33}TaO_6$, $Li_{6.33}KTa_{0.67}Zr_{0.33}O_6$ exhibits isotropic diffusion with high $\sigma_{300\ K}$ = 12 mS/cm (Fig. 5.5b and Fig. C3). The large region of Li^+ density at interstitial sites indicates ability of the large space to accommodate Li^+ (Fig. 5.5b), in agreement with our topological analysis. In contrast to the single-ion hopping induced by vacancies, Li^+ diffusion in $Li_{6.33}KTa_{0.67}Zr_{0.33}O_6$ exhibits concerted migration, involving two Li^+ jumping to their adjacent sites in pair within a few picoseconds (Fig. 5.6b and C2), as has been observed in many SICs, e.g., LLZO, LATP, and LGPS.[43] The strong time correlation of simultaneous hopping is also confirmed by the van Hove correlation function (Fig. C2).[184]

The energy barriers of the concerted migration from CI-NEB of 0.10-0.16 eV (Fig. 5.6b) are in agreement with the activation energy from AIMD simulations (0.18 eV), confirming the concerted migration as the key diffusion mechanism in $Li_{6.33}KTa_{0.67}Zr_{0.33}O_6$. The occupation of high-energy sites (0.9 eV) by Li insertion through doping activates the concerted migration of two Li^+ (Fig. 5.6b). One Li^+ at an

interstitial site with high energy migrates down would cancel out the energy barrier from adjacent Li at a lattice site climbing up (Fig. 5.6b).

3.5. New compositions with high Li^+ conductivity

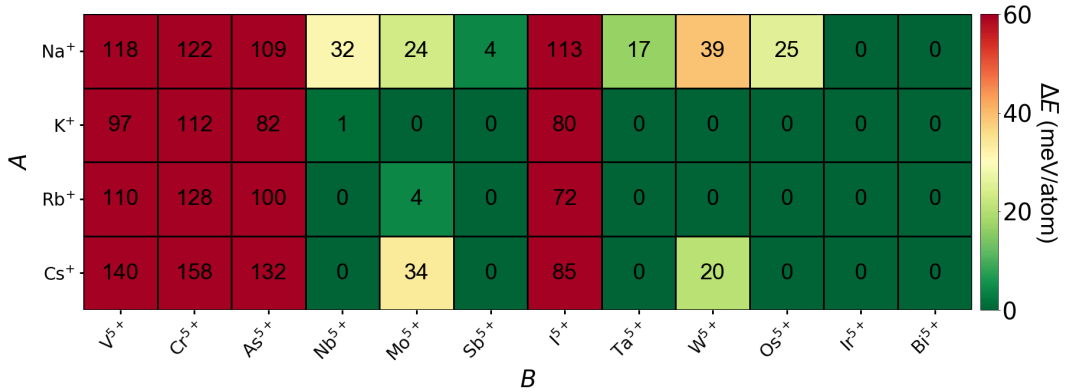

Figure 5.7. Calculated phase stabilities of Li_6ABO_6 with *A* at the twelve-coordinated site and *B* at the six-coordinated site.

Given the promising structural framework of Li_6KTaO_6 exhibiting superionic conduction, we designed new materials by substituting Li_6KTaO_6 to complement the family of Li_6ABO_6, with *A*, *B* referring to the twelve-coordinated site and six-coordinated site, respectively (Fig. 5.1). The charge-balance and geometry analysis (section 5.2.3) reduce the possible configurations of Li_6ABO_6 to 387. Then, we evaluated structural stabilities of those new compounds by calculating energy above hull ΔE (Fig. 5.7 and Fig. C6). All synthesized compounds belonging to Li_6ABO_6 family, i.e., Li_6KTaO_6, Li_6KBiO_6, Li_6KIrO_6 and Li_6RbBiO_6, were captured as stable materials in our compositional screening, validating our screening scheme.[169]

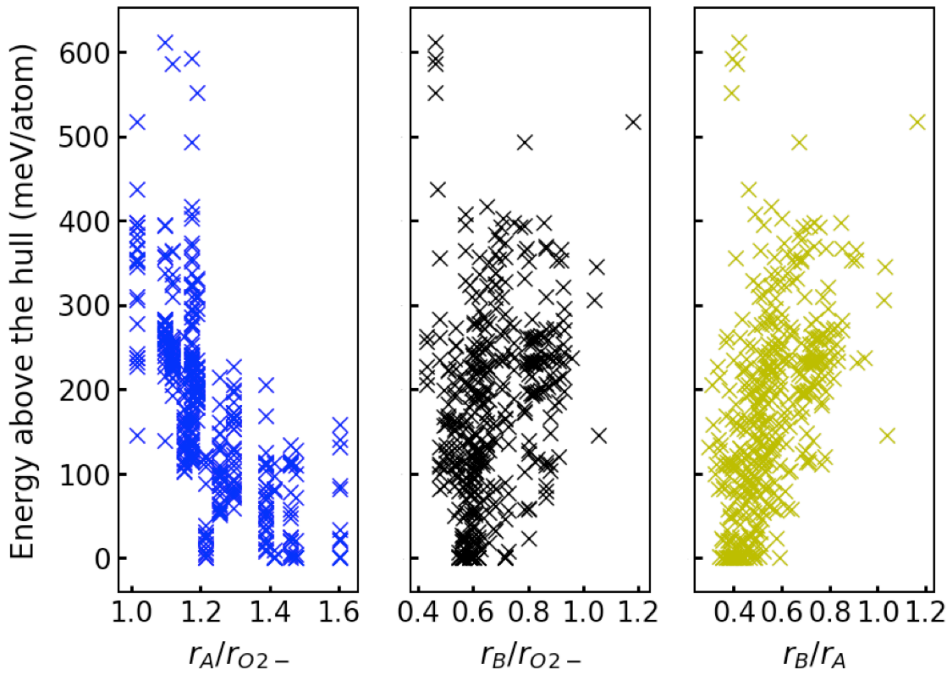

Figure 5.8. Phase stabilities of Li_6ABO_6 as a function of ratios of ionic radii for r_A/r_{O2-}, r_B/r_{O2-} and r_B/r_A, respectively. *A* refers to a cation at the twelve-coordinated site and *B* refers to a cation at the six-coordinated site.

By analyzing the relationship between phase stabilities and ionic radii of tested compounds (Fig. 5.8), we observed that Li_6ABO_6 tend to be stable with larger *A* ions satisfying $r_A/r_{O2-} > \sim 1.2$, and smaller *B* ions satisfying $\sim 0.5 < r_B/r_{O2-} < \sim 0.9$ and $0.2 < r_B/r_A < \sim 0.6$ (Fig. 5.8). Such tendency demonstrates the intrinsic correlation of ionic radii ratios to structural stability, and confirms the validity of our screening scheme in Li_6ABO_6.

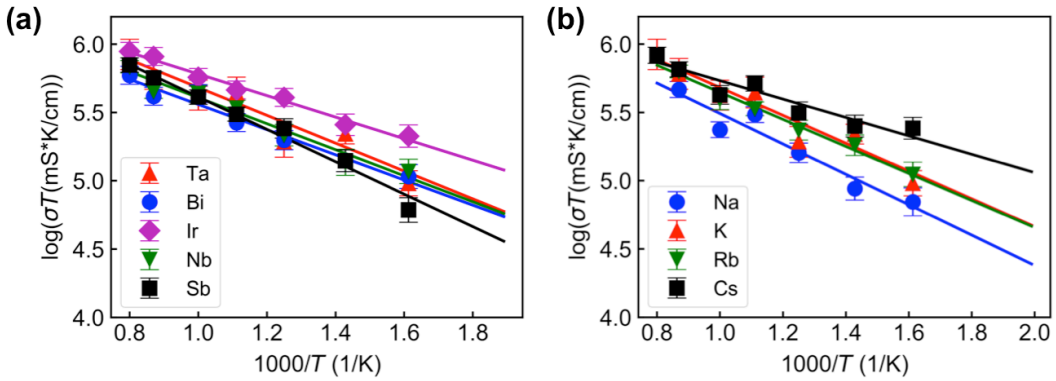

Figure 5.9. Arrhenius plots of (a) $Li_{6.33}KB_{0.67}Sn_{0.33}O_6$ (B = Ta, Bi, Ir, Nb and Sb) and (b) $Li_{6.33}ATa_{0.67}Sn_{0.33}O_6$ (A = Na, K, Rb, Cs).

Stable predictive compounds were further analyzed by evaluating their electrochemical properties and ionic conductivities after Sn^{4+} doping. We found all representative compounds with Li^+ interstitials were predicted to retain high ionic conductivities and low activation energies as those in prototype Li_6KTaO_6 (Fig. 5.9 and Table 5.2). In particular, Li_6KNbO_6, Li_6KSbO_6, Li_6NaTaO_6 and Li_6RbTaO_6 were predicted as suitable electrolytes with good electrochemical properties and ionic conductivities (Fig. 5.9 and Table 5.2). Thus, new cation combinations, e.g., Na, Rb at A sites and Nb, Sb at B sites, complement the family of SICs derived from the Li_6KTaO_6. In summary, the compositional screening of materials with a good structural framework based on simple but effective Pauling's rule can accelerate the design of SICs.

Table 5.2. Electrochemical stabilities in perfect Li_6ABO_6, and phase stabilities and diffusional properties of $Li_6AB_{0.67}Sn_{0.33}O_6$.

Li_6ABO_6	Bandgap (eV)	Electrochemical stability window ref. to Li/Li^+ (V)	ΔE of $Li_{6.33}AB_{0.67}Sn_{0.33}O_6$ (meV/atom)	E_a (eV)	$\sigma_{300\,K}$ (mS/cm)	Error bound (σ_{min}, σ_{max}) (mS/cm)
Li_6KBiO_6	2.73	[1.92, 3.29]	15	0.18±0.02	8.55	[3.66, 19.95]
Li_6KIrO_6	0.64	[2.02, 3.02]	14	0.16±0.02	29.07	[12.72, 66.44]
Li_6KNbO_6	4.57	[0.60, 2.91]	14	0.19±0.02	8.07	[3.68, 17.73]
Li_6KSbO_6	4.66	[1.32, 3.17]	12	0.24±0.02	2.34	[1.09, 5.03]
Li_6KTaO_6	5.70	[0.50, 3.07]	13	0.20±0.02	6.84	[2.28, 20.52]
Li_6NaTaO_6	4.84	[0.71, 2.88]	39	0.22±0.02	2.62	[0.94, 7.30]
Li_6RbTaO_6	5.51	[0.73, 3.01]	14	0.20±0.02	7.23	[2.97, 17.60]
Li_6CsTaO_6	5.50	[1.08, 2.68]	25	0.13±0.02	48.33	[22.12, 105.59]

5.4. Discussion

We predicted Li_6KTaO_6 as a promising SE for ASLiBs by systematically investigating its stability properties, the electrochemical window, and conductivities of doped Li_6KTaO_6 with different carrier defects. Our computational studies reveal the origin of superionic conduction in Li_6KTaO_6 by illustrating the roles of different carrier defects on Li^+ migration.

A notable feature in Li_6KTaO_6 is the dependence of Li^+ diffusion mechanism on different carrier defects, which originates from the structural framework of Li_6KTaO_6. Large space surrounded by six O^{2-} (Fig. 5.1b) in Li_6KTaO_6 can accommodate Li^+, forming interstitial sites with high site energies (~ 0.9 eV). The large energy difference between lattice and interstitial sites results to high energy barriers to prevents Li^+ migrating through interstitial sites, and enables Li^+ to hop among equivalent lattice sites instead. However, inserting Li^+ at interstitial sites

through doping can overcome the high site energy, and activate the concerted migration. Thus, introducing different carrier defects activate different Li^+ migration mechanism through different interconnected channels. The same phenomenon was also observed in $LiZnPS_4$ with the existence of vacant high-energy interstitial sites.[167] Adding extra Li^+ at those high-energy sites boosts ionic conduction through concerted migration, with the conductivity four magnitudes larger than that of $LiZnPS_4$ with vacancies. Therefore, the superionic conduction mechanisms activated through the incorporation of interstitial carrier defects has the structural origin of vacant high-energy sites.

While the occupation of high-energy sites serves as a key factor to activate the concerted migration of Li^+ to achieve superionic conduction, energy differences between high-energy and low-energy sites indicating the difficulty of occupation are different in various SICs. For materials with small energy differences between high-energy and low-energy sites, e.g., ~ 0.2 eV in $L_7P_3S_{11}$,[52, 68] their high-energy sites are accessible through thermal activation. Therefore, they can exhibit high ionic conductivity at perfect compositions. However, for materials with large energy differences between high-energy and low-energy sites (e.g., 0.6 eV in NASICON $LiTi_2(PO_4)_3$, 0.8 eV in $LiTaSiO_5$, 1.4 eV in $LiAlSiO_4$ and 0.9 eV in Li_6KTaO_6),[43] the occupation of high-energy sites should be realized by Li^+ insertion through aliovalent doping. Thus, the large value of energy difference between high-energy and low energy sites serves as an indicator for applying the Li insertion strategy to activate super-ionic conduction and to greatly boost conductivity.

Substituting original material to uncover new materials with better properties is an effective material design strategy, and has been successfully employed in many materials systems such as $Li_{10}MP_2O_{12}$ (M = Si, Ge, Sn) and Li_4MO_4 (M = Si, Ge).[41] Our compositional screening scheme is demonstrated to effectively and exhaustively discover new stable materials compositions, and also can reveal the intrinsic relationship between ionic radius and phase stabilities of structures. Thus, we demonstrated the first principles calculations in the discovery of new SICs, including the optimized Li_6KTaO_6, and the new compositions in the Li_6ABO_6 family. Our computational workflow is applicable in the design of other materials for other applications, and can accelerate the design of materials with promising properties.

5.5. Conclusions

Based on first principles calculations, we identified and designed Li_6KTaO_6 as a promising SE for ASLIBs through the comprehensive investigation of its stability properties, electrochemical windows and ionic conductivities. We found carrier defects (i.e., vacancies and interstitials) are necessary to enhance Li^+ diffusion in Li_6KTaO_6, and different carrier defects induce distinct Li^+ transport mechanism. While the incorporation of lithium vacancies can expedite single-ion hopping mediated by vacancy mechanism, Li^+ insertion through doping can activate concerted migration of multiple Li^+ to finally achieve superionic conduction in Li_6KTaO_6. Since Li_6KTaO_6 provides a promising structural framework for fast Li^+ conduction, we expanded the solid-state chemistry as new Li SICs in the Li_6KTaO_6 structure by high-throughput screening. Our study highlights critical roles of extrinsic carrier defect on

ionic diffusion, and provide a computational workflow for the design of SICs material family by compositional screening on promising structural framework.

Chapter 6: Conclusions and Future Work

6.1. Conclusions

The major conclusions of this dissertation are summarized below:

1) The first principles computation is demonstrated to systematically investigate the effect of ion substitution on electronic, anion and cation transport of solid materials. Furthermore, the computational prediction, design, and discovery of new materials were demonstrated for these properties in a range of materials.
2) Our study theoretically confirmed the polaron mechanism including polaron formation and migration as the key mechanism of electronic conductivity in perovskite proton-conductor materials. First principles computation illustrated that different dopants in $SrCeO_3$ exhibit different polaronic states and thus result in different electronic conductivity. Our computational study provides a general scheme to design materials with enhanced electronic conductivity through tailoring polarons.
3) Our study identified H^- diffusion in the $La_{2-x-y}Sr_{x+y}LiH_{1-x+y}O_{3-y}$ oxyhydrides is mediated by vacancy mechanism. We revealed that cation substitution in the oxyhydrides can modulate H^- diffusion mechanism from 2D to 3D diffusion pathways. We demonstrated the oxyhydrides with a K_2NiF_4 structure as a good structural framework for facile anion conduction. In addition, we predicted several novel dopants to increase hydride conductivity in Sr_2LiH_3O.
4) Our computational studies identified distinct Li^+ transport mechanisms induced by different carrier defects in Li_6KTaO_6. We found adding extra Li^+ to Li_6KTaO_6 can activate concerted migration of multiple Li^+ to achieve

superionic conduction in Li_6KTaO_6. Our study highlights critical roles of extrinsic carrier defect on ionic diffusion. We developed a computational workflow to predict a number of materials in a prototype structure. By employing the workflow, we predicted a group of Li superionic conductors with good stabilities by substituting the Li_6KTaO_6 structure.

6.2. Future work

This dissertation demonstrated the effect of ion substitution on electronic, anion and cation transport based on first principles calculations. In addition to topics we have studied, there are many remaining research problems. I list a few possible future directions below:

1) Since $SrCeO_3$ serves as permeation membranes to extract pure H_2 from mixed gas, it should have good chemical stability against mixed gas. However, $SrCeO_3$ exhibit poor chemical stability with CO_2, and decompose to $SrCO_3$ and CeO_2. Introducing dopants in $SrCeO_3$ can tune the reaction products and change reaction energies. Thus, I can investigate dopants' effect on chemical stability of $SrCeO_3$ against CO_2 and find promising dopants that can stabilize $SrCeO_3$.
2) While hydride ions are attractive charge carrier in electrochemical devices, hydride ion conductors are really rare in nature. Since chemical substitution was demonstrated as an effective way to discover novel compounds with excellent properties in chapter 5, substituting current oxyhydrides may accelerate the discovery of new hydride ion conductors. I can predict more

stable oxyhydrides by substituting current $La_{2-x-y}Sr_{x+y}LiH_{1-x+y}O_{3-y}$ using the same method demonstrated in chapter 5.

Publications, Patents, and Presentations

Publications

1) X. He[§], **Q. Bai**[§], Y. Liu, A.M. Nolan, Y. Mo, "Crystal Structural Framework of Lithium Super-ionic Conductors", ***Advanced Energy Materials*** (2019) 201902078, DOI: 10.1002/aenm.201902078. **([§] co-first author)**
2) **Q. Bai**, X. He. Y. Zhu, Y. Mo, "First-Principles Study of Oxyhydride H- Ion Conductors: Towards Facile Anion Conduction in Oxide-Based Materials", ***ACS Applied Energy Materials*** 1 (2018) (4) 1626.
3) **Q. Bai**, L. Yang, H. Chen, Y. Mo, "Computational Studies of Electrode Materials in Sodium-Ion Batteries", ***Advanced Energy Materials*** 8 (2018) (17) 1702998.
4) **Q. Bai**, Y. Zhu, X. He, E. Wachsman, Y. Mo, "First Principles Hybrid Functional Study of Small Polarons in Doped $SrCeO_3$ Perovskite: Towards Computational Design of Materials with Tailored Polaron", ***Ionics*** 24 (2018) (4) 1139.
5) K.H. Park[§], **Q. Bai**[§], D.H. Kim, D.Y. Oh, Y. Zhu, Y. Mo, Y.S. Jung, "Design Strategies, Practical Considerations, and New Solution Processes of Sulfide Electrolytes for All-Solid-State Batteries", ***Advanced Energy Materials*** 8 (2018) (18) 1800035. **([§] co-first author)**
6) **Q. Bai**, Y. Zhu, X. He, Y. Mo, "Accelerated Computational Design of Mixed Protonic and Electronic Conduction For H_2 Separation through Tailoring Polaron", ***ECS Transactions*** 80 (2017) (9) 175.

7) S. Wang, **Q. Bai**, A.M. Nolan, Y. Liu, S. Gong, Q. Sung, Y. Mo, "Lithium Chlorides and Bromides as Promising Solid-State Chemistries for Fast Ion Conductors with Good Electrochemical Stability", ***Angewandte Chemie International Edition*** 58 (2019) (24) 8039
8) Y. Liu, **Q. Bai**, A.M. Nolan, Y. Zhou, Y. Wang, Y. Mo, Y. Xia, "Lithium Ion Storage in Lithium Titanium Germanate", ***Nano Energy*** (2019) DOI: 10.1016/j.nanoen.2019.104094.
9) A.M. Nolan, Y. Zhu, X. He, **Q. Bai**, Y. Mo, "Computational-accelerated Design of Materials and Interfaces for All-solid-state Lithium-ion Batteries "***Joule*** 2 (2018) (10) 2016.
10) Y. Zhang, X. He, Z. Chen, **Q. Bai**, A.M. Nolan, C. Roberts, D. Banerjee, T. Matsunaga, Y. Mo, C. Ling, "Unsupervised Discovery of Solid-State Lithium Ion Conductors", ***Nature Communications*** (2019). (in press)

Patents in Application

1) "Novel Fluoride Compounds as Lithium Super-Ionic Conductors, Solid Electrolyte and Coating Layer for Lithium Metal Battery and Lithium Ion Battery", U.S. Non-provisional Patent Application **No. 16/114946**.
2) "Novel Lithium Metal Nitrides as Lithium Super-Ionic Conductors", U.S. Non-provisional Patent Application **No. 16/155,349**.
3) "Lithium Silicate Compounds as Lithium Super-Ionic Conductors, Solid Electrolyte and Coating Layer for Lithium Metal Battery and Lithium-Ion Battery", U.S. Non-provisional Patent Application **No. 16/264,294**.

4) "Novel Lithium Metal Sulfides as Lithium Super-Ionic Conductors, Solid Electrolyte and Coating Layer for Lithium Metal Battery and Lithium-Ion Battery", U.S. Non-provisional Patent Application **No. 16/264,499**.
5) "Lithium Phosphate Derivative Compounds as Lithium Super-Ionic Conductors, Solid Electrolyte and Coating Layer for Lithium Metal Battery and Lithium-Ion Battery", U.S. Non-provisional Patent Application **No. 16/264,445**.
6) "Novel Lithium Bismuth Oxide Compounds as Lithium Super-Ionic Conductors, Solid Electrolyte and Coating Layer for Lithium Metal Battery and Lithium-Ion Battery", U.S. Non-provisional Patent Application **No. 16/153,335**.
7) "Lithium Potassium Element Oxide Compounds as Li Super-Ionic Conductor, Solid Electrolyte and Coating Layer For Lithium Metal Battery and Lithium-ion Battery", U.S. Non-provisional Patent Application **No. 16/570,888**.
8) "Lithium Potassium Tantalate Oxides as Li Super-Ionic Conductor, Solid Electrolyte and Coating Layer For Lithium Metal Battery and Lithium-ion Battery", U.S. Non-provisional Patent Application **No. 16/570,811**.

Presentations

1) **Q. Bai**, Understanding and Designing Novel H^- Ionic Conductors Based on First Principles Calculations, Materials Research Society, Boston (2018).
2) **Q. Bai**, Understanding and Designing Novel H^- Ionic Conductors Based on First Principles Calculations, 232nd Electrochemical Society Meeting, National Harbor, Maryland (2017).

3) **Q. Bai**, Accelerated Computational Design of Mixed Protonic and Electronic Conductors for H_2 Separation through Tailoring Polaron, 232nd Electrochemical Society Meeting, National Harbor, Maryland (2017).

4) **Q. Bai**, Accelerated Computational Design of Mixed Protonic and Electronic Conductors for H_2 Separation, American Chemical Society, Washington, DC (2017).

5) **Q. Bai**, Accelerated Computational Design of Mixed Protonic and Electronic Conductors for H_2 Separation, Materials Research Society, Boston (2016).

Appendices

Appendix A

Appendix A provides supplementary materials for the chapter 3, including lattice parameters of the structure; Polarons induced by intrinsic defects; Polarons induced by other dopants; Transition levels of dopants; Migration barriers of other polarons.

Table A1. Calculated lattice parameters from the GGA and HSE06 methods compared with the experimental values [123].

	Expt.	GGA	HSE06
a (Å)	6.000	6.050	5.986
b (Å)	6.145	6.213	6.149
c (Å)	8.575	8.666	8.560

Polaron induced by intrinsic defects

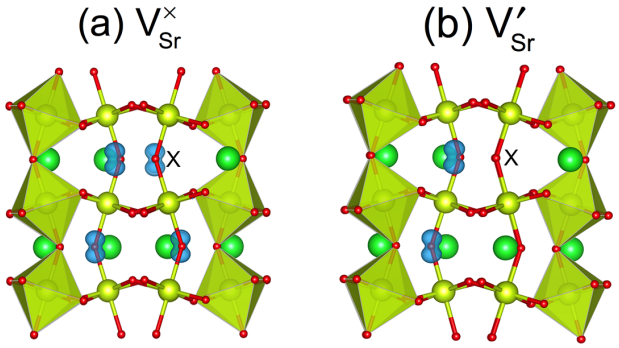

Figure A1. Hole polarons introduced by V_{Sr} as shown by spin densities of (a) $V_{Sr}^{\times}$ and (b) V'_{Sr}. The black crosses show the locations of V_{Sr}. The isosurfaces of the spin densities are 10% of the maximum.

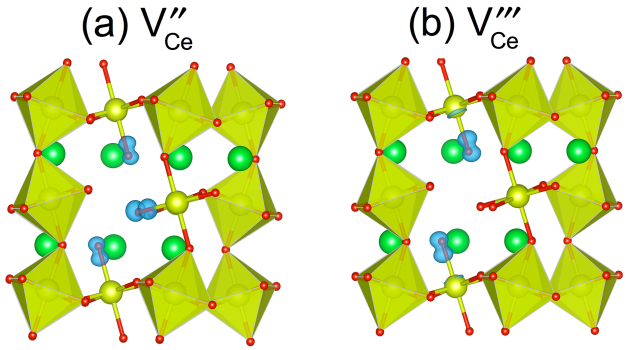

Figure A2. Hole polarons introduced by V_{Ce} as shown by spin densities of (a) V''_{Ce} and (b) V''''_{Ce}. The isosurfaces of the spin densities are 10% of the maximum.

Polaron in Y-doped $SrCeO_3$

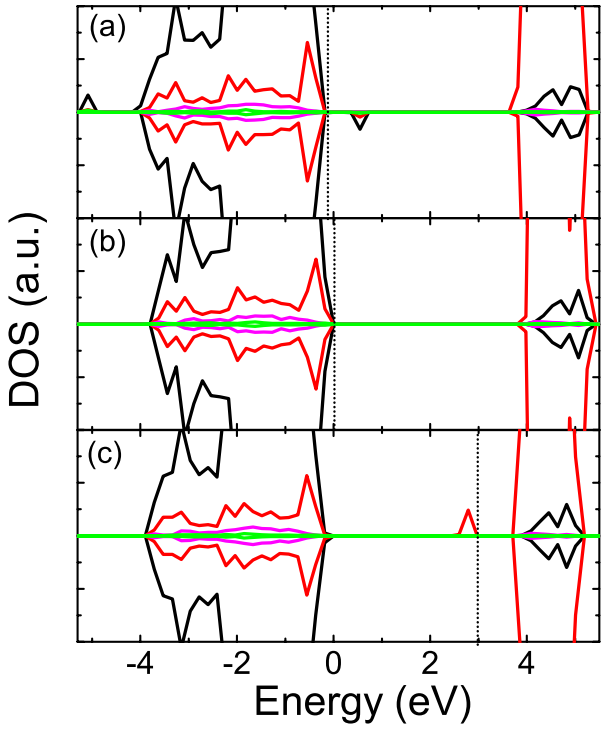

Figure A3. PDOS of Y-doped $SrCeO_3$ with (a) Y'_{Ce} with a hole polaron h_p localized on the YO_6 octahedron, (b) Y'_{Ce}, or (c) Y'_{Ce} with an electron polaron e_p localized on Ce. (Red: Ce; Black: O; Purple: Sr; Green: Y). Vertical dash lines represent the calculated Fermi energy at 0 K.

Polaron in Sc-doped $SrCeO_3$

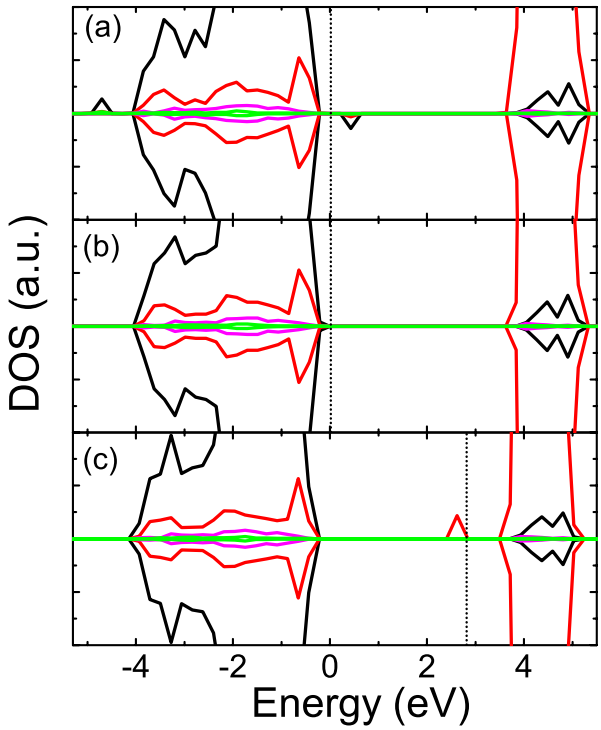

Figure A4. PDOS of Sc-doped $SrCeO_3$ with (a) Sc'_{Ce} with a hole polaron h_p localized on the ScO_6 octahedron, (b) Sc'_{Ce}, or (c) Sc'_{Ce} with an electron polaron e_p localized on Ce. (Red: Ce; Black: O; Purple: Sr; Green: Sc). Vertical dash lines represent the calculated Fermi energy at 0 K.

Polaron in Yb-doped $SrCeO_3$

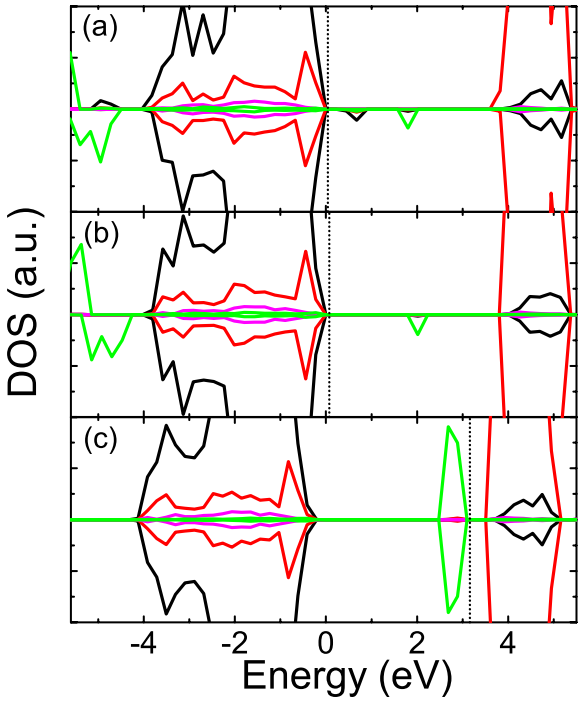

Figure A5. PDOS of Yb-doped $SrCeO_3$ with (a) Yb'_{Ce} with a hole polaron h_p on the YbO_6 octahedron, (b) Yb'_{Ce}, or (c) Yb''_{Ce}. (Red: Ce; Black: O; Purple: Sr; Green: Yb). Vertical dash lines represent the calculated Fermi energy at 0 K.

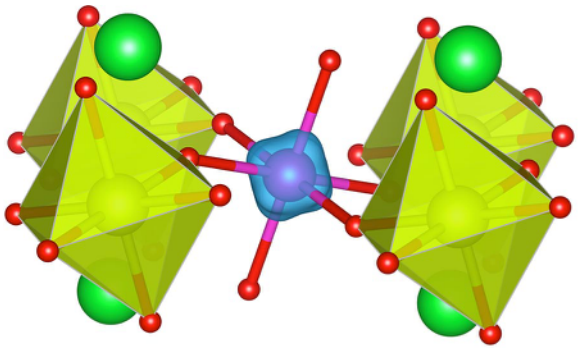

Figure A6. An electron polaron localized on the Yb site forming Yb''_{Ce} as shown by the differential spin density between Yb''_{Ce} and Yb'_{Ce}. The Yb dopant is shown in purple. The isosurfaces of the differential spin density in blue and yellow correspond to 10% of the maximum and minimum, respectively.

Polaron in Nd-doped $SrCeO_3$

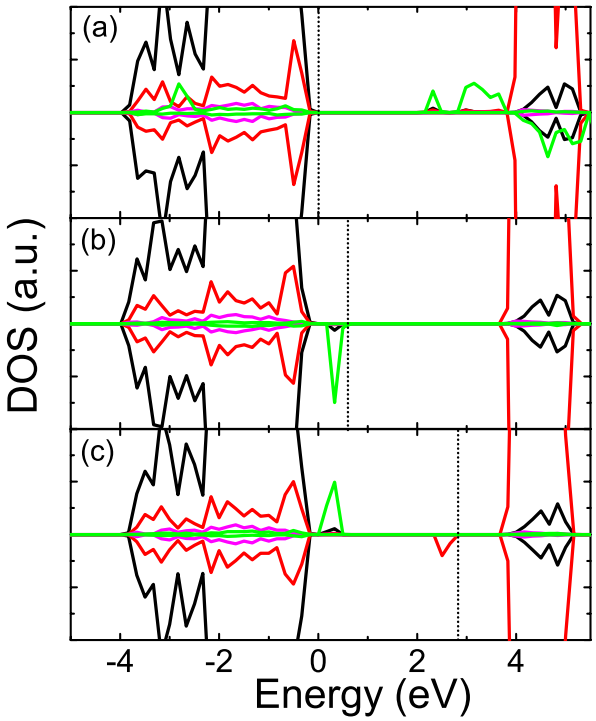

Figure A7. PDOS of Nd-doped $SrCeO_3$ with (a) $Nd_{Ce}^{\times}$, (b) Nd_{Ce}', or (c) Nd_{Ce}' with an electron polaron e_p localized on a Ce ion. (Red: Ce; Black: O; Purple: Sr; Green: Nd). Vertical dash lines represent the calculated Fermi energy at 0 K.

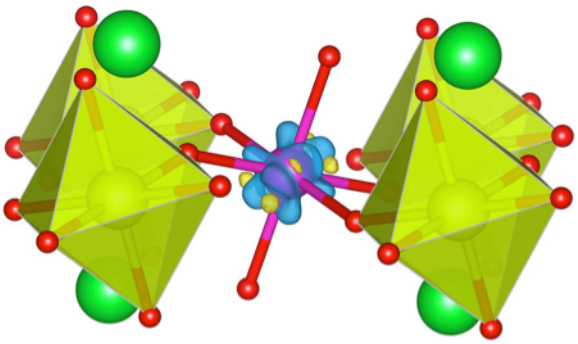

Figure A8. An electron polaron localized on the Nd site as shown by the differential spin density between Nd_{Ce}' and $Nd_{Ce}^{\times}$. The Nd dopant is shown in purple. The isosurfaces of the differential spin density in blue and yellow correspond to 30% of the maximum and minimum, respectively.

Table A2. Transition levels $\varepsilon(q/q')$ between charge states q/q' and valence states of various dopants in $SrCeO_3$.

defect	q/q' *	$\varepsilon(q/q')$ (eV)	valence state of the dopant
Ce_{Ce}	$0+h_p/0$	0.39	+4/+3
	0/-1	3.43	
Gd_{Ce}	$-1+h_p/-1$	0.45	+3
	$-1/-1+e_p$	3.25	
Y_{Ce}	$-1+h_p/-1$	0.32	+3
	$-1/-1+e_p$	3.24	
Sc_{Ce}	$-1+h_p/-1$	0.34	+3
	$-1/-1+e_p$	3.29	
Eu_{Ce}	$-1+h_p/-1$	0.50	+3/+2
	-1/-2	2.84	
Yb_{Ce}	$-1+h_p/-1$	0.30	+3/+2
	-1/-2	3.02	
Pr_{Ce}	0/-1	2.61	+4/+3
	$-1/-1+e_p$	3.33	
Nd_{Ce}	0/-1	1.35	+4/+3
	$-1/-1+e_p$	3.27	
Cr_{Ce}	0/-1	1.51	+4/+3/+2 **
	$-1/-1+e_p$	3.26	

* h_p is a hole polaron localized on the dopant centered oxygen octahedron or the CeO_6 octahedron, and e_p is an electron polaron on the Ce site.

** Cr''_{Ce} is energetically less favorable than the complex of Cr'_{Ce} and Ce'_{Ce}.

Table A3. Polaron migration energies among dopants in doped $SrCeO_3$

Migration path	Energy barriers (eV)
Yb-Yb*	0.32
Nd-Nd	0.37
Cr-Cr	0.58

* Energy barriers of Yb-Yb was calculated using the hybrid functional with $\alpha = 0.40$.

Appendix B

Appendix B provides supplementary materials for the chapter 4, including constructed supercells in computations; Calculated lattice parameters compared with experiments; Calculated density of states; Born-effective-charge tensor and Bader charge of each element in the oxyhydrides; Relative Ewald energies with different number of apical H^-; Migration events with different number of H^- hopping; Migration barriers for H^- diffusion in Sr_2LiH_3O; Defect formation energies of H^- vacancies in the oxyhydrides.

Table B1. Supercell models for different compositions of the oxyhydrides with various disorder sites.

Modeled Composition	Constructed supercell	Disorder sites
La_2LiHO_3	$La_{36}Li_{18}H_{18}O_{54}$	Ordered
$LaSrLiH_2O_2$	$La_{18}Sr_{18}Li_{18}H_{36}O_{36}$	La/Sr and H/O
Sr_2LiH_3O	$Sr_{36}Li_{18}H_{54}O_{18}$	H/O
$La_{1.9}Sr_{0.1}LiH_{0.9}O_3$	$La_{34}Sr_2Li_{18}H_{16}O_{54}$	La/Sr and H/O
$La_{1.8}Sr_{0.2}LiH_{0.8}O_3$	$La_{32}Sr_4Li_{18}H_{14}O_{54}$	La/Sr and H/O
$La_{0.9}Sr_{1.1}LiH_{1.9}O_2$	$La_{16}Sr_{20}Li_{18}H_{34}O_{36}$	La/Sr and H/O
$La_{0.8}Sr_{1.2}LiH_{1.8}O_2$	$La_{14}Sr_{22}Li_{18}H_{32}O_{36}$	La/Sr and H/O
$La_{0.7}Sr_{1.3}LiH_{1.7}O_2$	$La_{13}Sr_{23}Li_{18}H_{31}O_{36}$	La/Sr and H/O
$La_{0.6}Sr_{1.4}LiH_{1.6}O_2$	$La_{11}Sr_{25}Li_{18}H_{29}O_{36}$	La/Sr and H/O

Table B2. Calculated lattice parameters of La_2LiH_3O, $LaSrLiH_2O_2$ and Sr_2LiH_3O using GGA and HSE06 compared with experimental data.[5]

		a (Å)	*b* (Å)	*c* (Å)
La_2LiHO_3	GGA	3.58	3.79	12.98
	HSE06	3.56	3.77	12.84
	Expt.	3.58	3.76	12.97
$LaSrLiH_2O_2$*	GGA	3.65	3.65	13.26
	HSE06	3.62	3.62	13.20
	Expt.	3.65	3.65	13.30
Sr_2LiH_3O*	GGA	3.74	3.74	13.29
	HSE06	3.71	3.71	13.19
	Expt.	3.72	3.72	13.32

* Calculated lattice parameters of $LaSrLiH_2O_2$ and Sr_2LiH_3O were based on the ordered lowest energy structure obtained following the method in section 4.2.1, while the experimental values are based on the disordered structures.

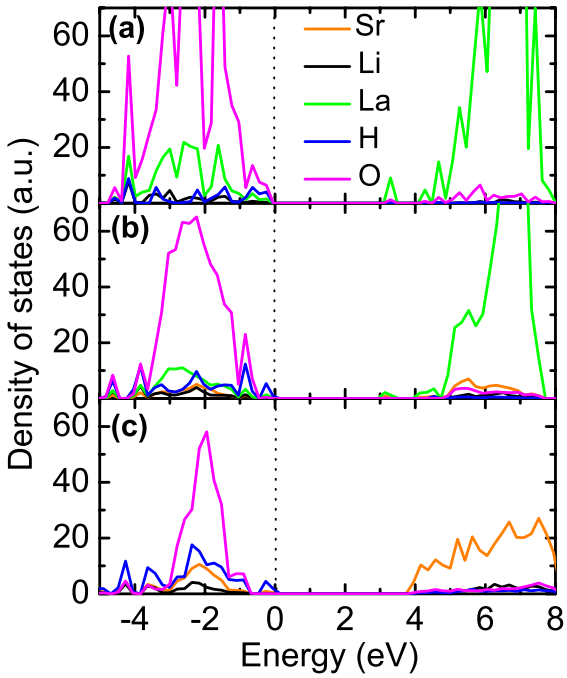

Figure B1. Calculated density of states of (a) La_2LiHO_3, (b) $LaSrLiH_2O_2$ and (c) Sr_2LiH_3O using HSE06.

Table B3. Calculated Born-effective-charge tensor (Z) of each element in La_2LiHO_3.

Element	Born effective charge								
	xx	*yy*	*zz*	*xy*	*xz*	*yx*	*yz*	*zx*	*zy*
H	-0.55	-0.94	-1.08	0.00	0.00	0.00	0.00	0.00	0.00
O	-2.82	-2.34	-2.92	0.00	0.00	0.00	0.00	0.00	0.00
Li	0.89	0.85	0.98	0.00	0.00	0.00	0.00	0.00	0.00
La	4.09	3.66	4.50	0.00	0.00	0.00	0.00	0.00	0.00

Table B4. Calculated Born-effective-charge tensor (Z) of each element in $LaSrLiH_2O_2$.

Element	Born effective charge								
	xx	*yy*	*zz*	*xy*	*xz*	*yx*	*yz*	*zx*	*zy*
H	-0.84	-0.80	-1.07	0.00	0.00	0.00	0.00	0.00	0.00
O	-2.68	-2.63	-2.60	-0.01	0.00	-0.01	0.00	0.00	0.00
Li	0.82	0.81	0.92	0.00	0.00	0.00	0.00	0.00	0.00
La	3.96	3.64	3.89	0.01	0.01	0.01	0.01	0.01	0.01
Sr	2.35	2.47	2.51	0.00	0.00	0.00	0.00	0.00	0.00

Table B5. Calculated Born-effective-charge tensor (Z) of each element in Sr_2LiH_3O.

Element	Born effective charge								
	xx	*yy*	*zz*	*xy*	*xz*	*yx*	*yz*	*zx*	*zy*
H	-0.95	-0.95	-0.97	0.00	0.00	0.00	0.00	0.00	0.00
O	-2.42	-2.42	-2.44	0.00	0.03	0.00	-0.01	0.02	-0.01
Li	0.84	0.84	0.88	0.00	0.00	0.00	0.00	0.00	0.00
Sr	2.21	2.21	2.23	0.00	-0.01	0.00	0.01	-0.01	0.01

Table B6. Bader charge of each element in $La_{2-x-y}Sr_{x+y}LiH_{1-x+y}O_{3-y}$.

Element	Bader charge					
	$y = 0$		$y = 1$			
	$x = 0.1$	$x = 0.2$	$x = 0.1$	$x = 0.2$	$x = 0.3$	$x = 0.4$
H	-0.65	-0.65	-0.71	-0.72	-0.72	-0.74
O	-1.37	-1.38	-1.41	-1.42	-1.42	-1.43
Li	0.83	0.83	0.83	0.83	0.83	0.83
Sr	1.50	1.50	1.48	1.48	1.48	1.48
La	1.96	1.96	1.90	1.90	1.90	1.91

Table B7. Calculated Born-effective-charge tensor (Z) of H in in $La_{2-x-y}Sr_{x+y}LiH_{1-x+y}O_{3-y}$.

Z	Born effective charge of H				
	$y = 0$		$y = 1$		
	$x = 0.1$	$x = 0.2$	$x = 0.1$	$x = 0.2$	$x = 0.3$
xx	-0.59	-0.58	-0.76	-0.86	-0.86
yy	-0.99	-1.03	-0.80	-0.87	-0.86
zz	-1.13	-1.13	-1.05	-1.04	-1.05
xy	0.00	0.00	0.00	0.00	0.00
xz	0.00	0.00	0.00	0.00	0.01
yx	0.00	0.00	0.00	0.00	0.00
yz	0.00	0.01	0.00	0.00	0.00
zx	0.00	0.00	0.00	0.00	0.01
zy	0.00	0.01	0.00	0.00	0.00

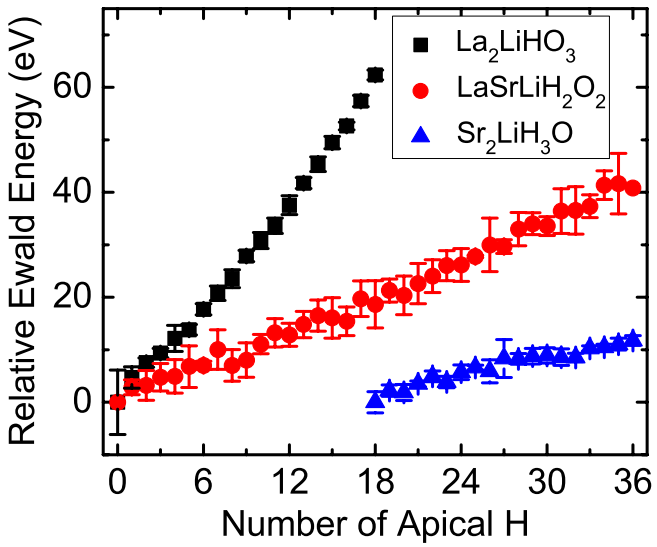

Figure B2. Relative Ewald energy of La_2LiHO_3, $LaSrLiH_2O_2$ and Sr_2LiH_3O with anion sublattice containing different numbers of H^- at apical sites, referenced to the lowest average Ewald energy. Each data point is an average Ewald energy of five representative structures (same as the configurations calculated in Fig. 4.3), where the error bar indicates the maximum deviation from the average Ewald energy.

Table B8. Site energy of H^- based on the Ewald summation[155] from cation sublattice is evaluated. The site energy of a single H^- ion on axial sites is referenced to that on apical sites. Negative values indicate the electro-state interactions from cation sublattice favors anions with more negative charge (e.g. O^{2-}) at axial sites.

Composition	Ewald site energy of axial site ref. to apical site (eV)
La_2LiH_3O	-2.46
$LaSrLiH_2O_2$	-0.83
Sr_2LiH_3O	-2.49

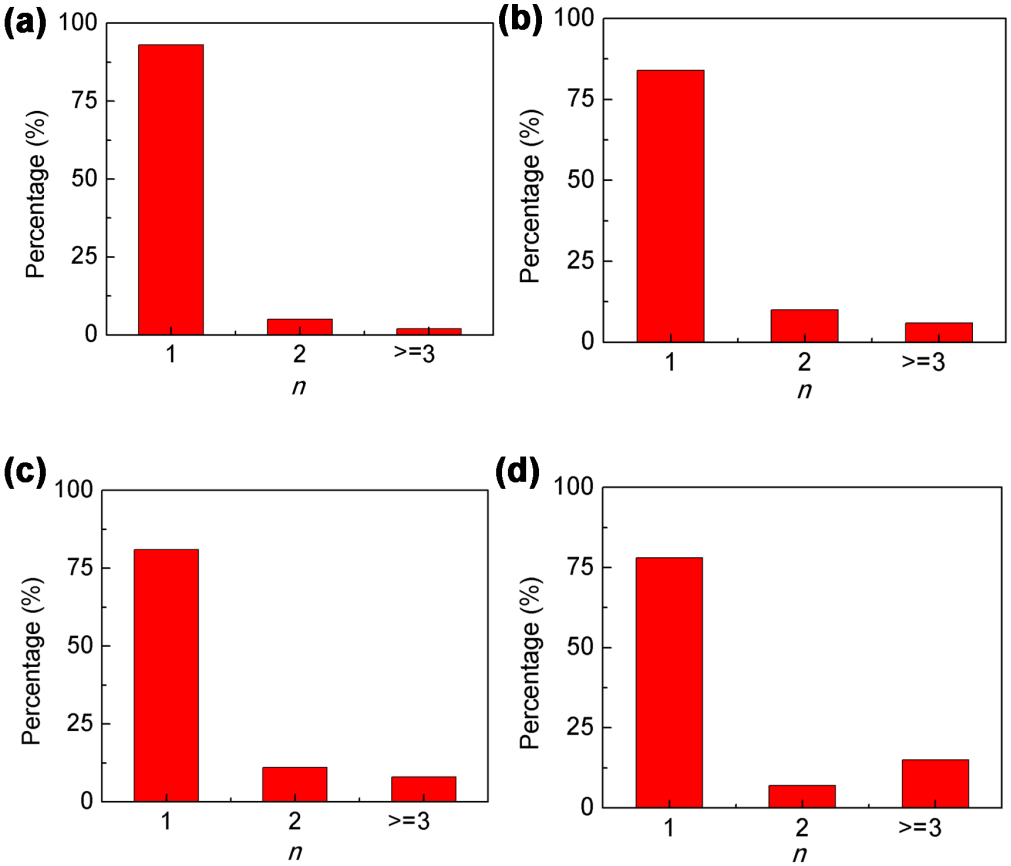

Figure B3. Percentage of migration events with different number *n* of H^- hopping observed during AIMD simulations for (a) $LaSrLiH_2O_2$, (b) Sr_2LiH_3O, (c) $La_{0.9}Sr_{1.1}H_{1.9}O_2$, and (d) $La_{0.8}Sr_{1.2}H_{1.8}O_2$ at 1000 K. H^- hoppings that happen within 1 ps were grouped as one migration event using the same method as the previous study.[43]

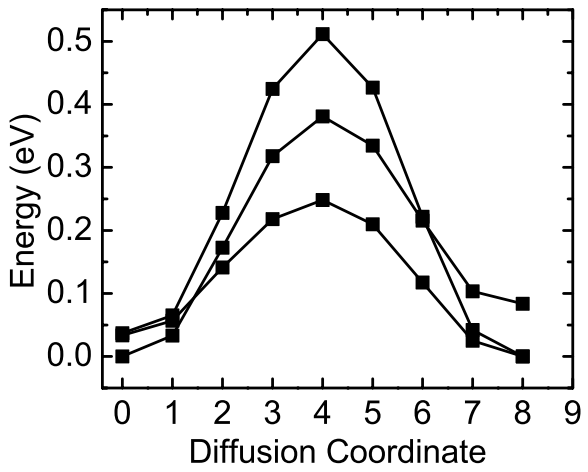

Figure B4. Migration barriers for in-plane H^- diffusion of Sr_2LiH_3O calculated by CI-NEB.

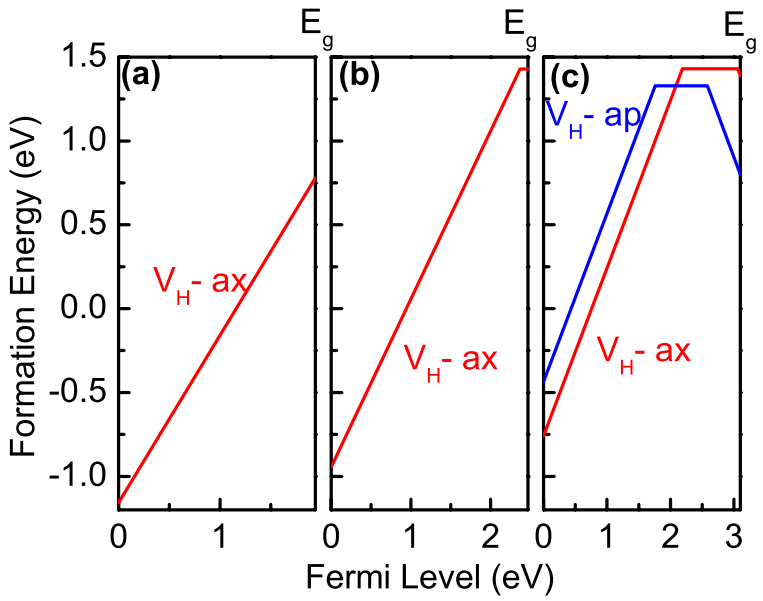

Figure B5. Defect formation energies of H^- vacancy V_H at the axial site (V_H-ax) or apical site (V_H-ap) were calculated following the standard defect computation scheme in the literature.[117, 185] (a) Defect formation energy of V_H-ax in La_2LiHO_3 as a function of the Fermi level under the hydrogen rich limit $\Delta\mu_H$ = -0.08 eV referenced

to H_2 gas at 298.15 K and 1atm. (b) Defect formation energy of V_H-ax in $LaSrLiH_2O_2$ as a function of the Fermi level under the hydrogen rich limit $\Delta\mu_H$ = -0.05 eV. (c) Defect formation energy of V_H-ax and V_H-ap in Sr_2LiH_3O as a function of the Fermi level under the hydrogen rich limit $\Delta\mu_H$ = -0.09 eV. For $LaSrLiH_2O_2$ and Sr_2LiH_3O with nonequivalent H sites, multiple configurations with single V_H were generated following the method in section 2.1, and the formation energies calculated from the ground-state configurations were shown here. The chemical potential limits of the hydrogen rich environment were obtained from *pymatgen*[111] by constructing the phase diagram and energy convex hull as in previous studies.[7, 33]

Table B9. Calculated Born-effective-charge tensor (Z) of H in $Sr_{1.8}M_{0.2}LiH_{2.8}O$.

Z	Born effective charge of H in $Sr_{1.8}M_{0.2}LiH_{2.8}O$			
	M = Na	K	Rb	Cs
xx	-0.93	-0.94	-0.94	-0.95
yy	-0.93	-0.93	-0.93	-0.95
zz	-0.97	-0.96	-0.97	-0.98
xy	0.00	0.00	0.00	0.00
xz	-0.01	-0.01	0.00	0.00
yx	0.00	0.00	0.00	0.00
yz	0.00	0.00	0.00	0.00
zx	-0.01	-0.01	0.00	0.00
zy	0.00	0.00	0.00	0.00

Appendix C

Appendix C provides supplementary materials for the chapter 5.

Table C1. Calculated lattice parameters of Li_6KTaO_6 using PBE and HSE06 compared with experimental data.[168]

	PBE	HSE06	Expt.
a (Å)	8.31	8.21	8.23
b (Å)	8.31	8.21	8.23
c (Å)	7.29	7.21	7.21
α (°)	90	90	90
β (°)	90	90	90
γ (°)	120	120	120

Table C2. Calculated elastic tensor (C_{ij}), and derived bulk modulus (*B*), shear modulus (*G*), Young's modulus (*E*), Poisson's ratio (*v*) and the ratio of *B*/*G* using the PBEsol function using the Voigt-Reuss-Hill approximation.[180]

C_{ij} (GPa)	*B* (GPa)	*G* (GPa)	*E* (GPa)	*v*	*B*/*G*
$\begin{bmatrix} 169.8 & 73.4 & 51.2 & 23.7 & 0 & 0 \\ 73.4 & 169.8 & 51.2 & -23.7 & 0 & 0 \\ 51.2 & 51.2 & 212.7 & 0 & 0 & 0 \\ 23.7 & -23.7 & 0 & 57.2 & 0 & 0 \\ 0 & 0 & 0 & 0 & 57.2 & 23.7 \\ 0 & 0 & 0 & 0 & 23.7 & 48.2 \end{bmatrix}$	100.3	51.8	132.3	0.3	1.9

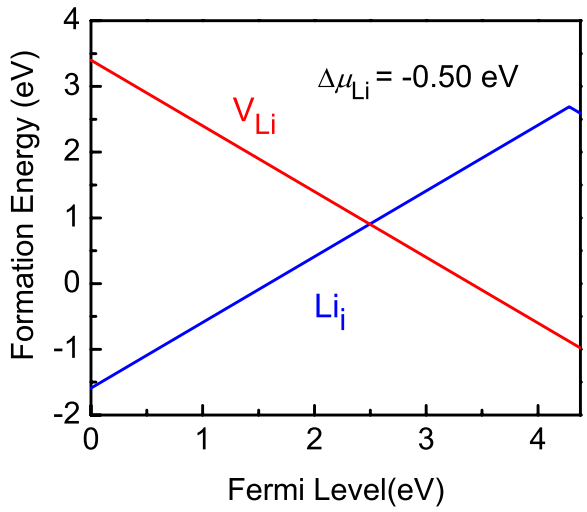

Figure C1. Defect formation energies of Li vacancy V_{Li} and interstitial Li_i calculated as a function of the Fermi level under the lithium rich limit $\Delta\mu_{Li}$ = -0.50 eV, following the standard defect computation scheme from the literature.[117]

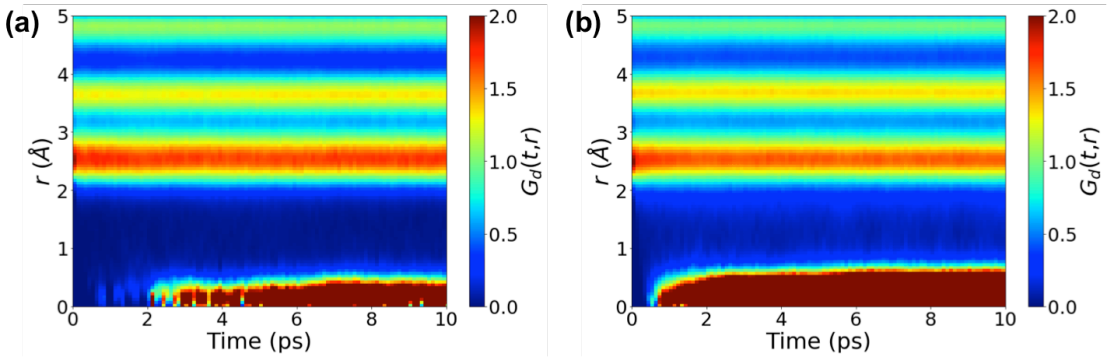

Figure C2. Van Hove correlation function of Li^+ dynamics on distinctive Li^+ during AIMD simulations of (a) $Li_{5.67}K_{0.67}Ba_{0.33}TaO_6$ and (b) $Li_{6.33}KTa_{0.67}Zr_{0.33}TaO_6$ at 800 K.

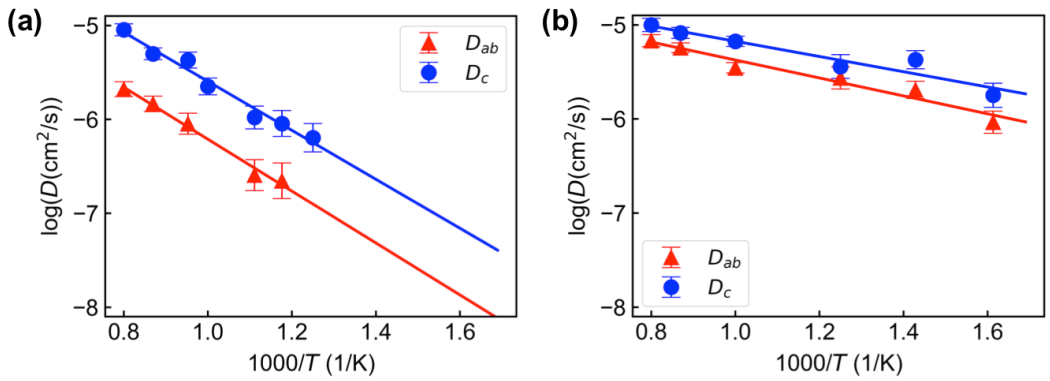

Figure C3. Arrhenius plots of diffusivities along the *c* direction D_c and in the *ab* plane D_{ab} of (a) $Li_{5.67}K_{0.67}Ba_{0.33}TaO_6$ and (b) $Li_{6.33}KTa_{0.67}Zr_{0.33}TaO_6$.

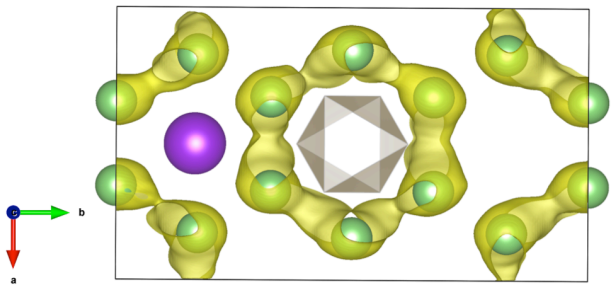

Figure C4. Li^+ probability density of $Li_{5.67}K_{0.67}Ba_{0.33}TaO_6$ viewed perpendicularly to the *ab* plane from AIMD simulations at 800 K. The isosurface refers to $0.002\rho_0$, and ρ_0 indicates the average Li^+ density probability in each structure from entire AIMD simulations.

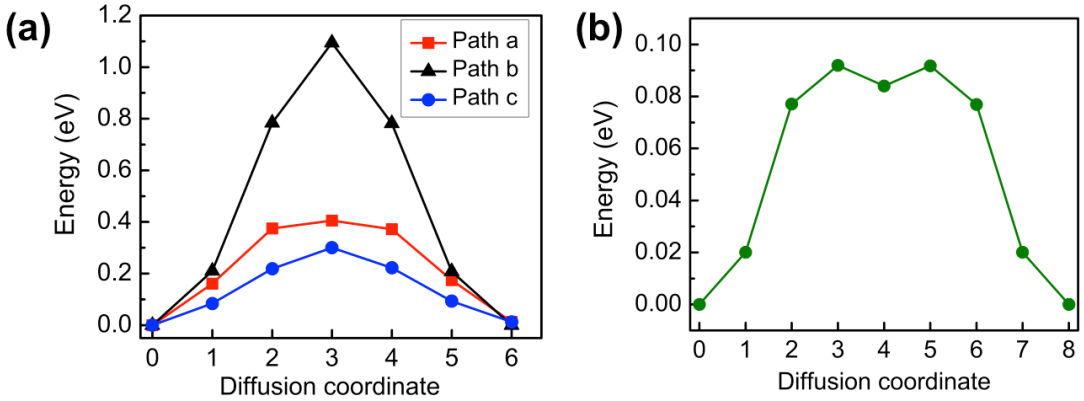

Figure C5. Li^+ migration energy barriers in undoped Li_6KTaO_6 from (a) single-ion hopping via vacancy mechanism, and from (b) two Li^+ hopping with one Li interstitial to the nearest sites in pair.

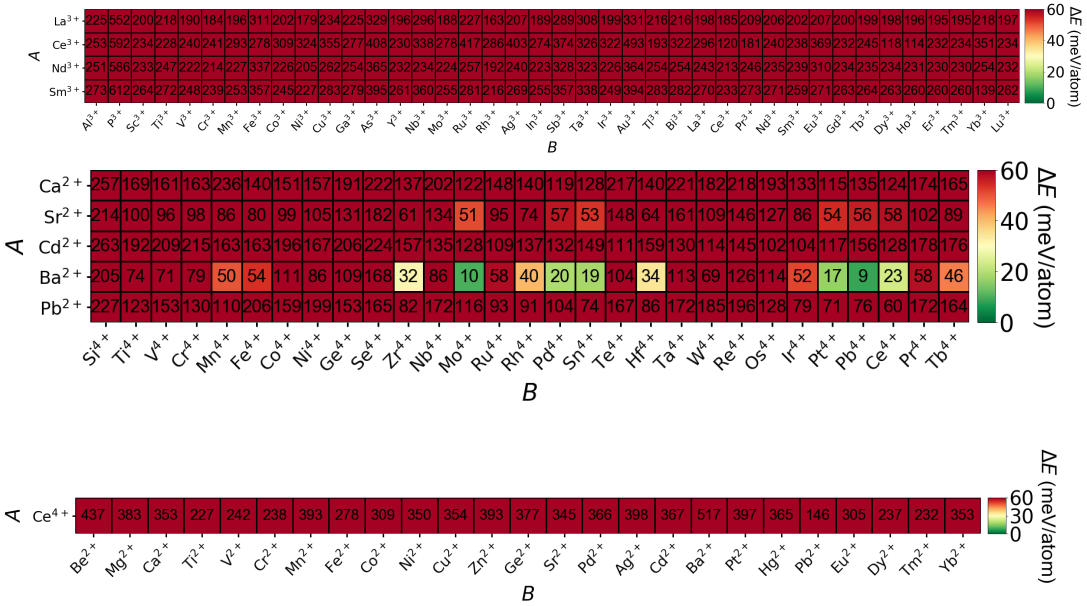

Figure C6. Calculated phase stabilities of Li_6ABO_6 with *A* at the twelve-coordinated site and *B* at the six-coordinated site.

Bibliography

[1] K. H. Park, Q. Bai, D. H. Kim, D. Y. Oh, Y. Zhu, Y. Mo, Y. S. Jung, *Advanced Energy Materials* **2018**, *8*, 1800035.

[2] Q. Bai, L. Yang, H. Chen, Y. Mo, *Advanced energy materials* **2018**, *8*, 1702998.

[3] A. R. West, *Journal of Materials Chemistry* **1991**, *1*, 157.

[4] Q. Bai, X. He, Y. Zhu, Y. Mo, *ACS Applied Energy Materials* **2018**, *1*, 1626.

[5] G. Kobayashi, Y. Hinuma, S. Matsuoka, A. Watanabe, M. Iqbal, M. Hirayama, M. Yonemura, T. Kamiyama, I. Tanaka, R. Kanno, *Science* **2016**, *351*, 1314.

[6] T. Norby, *Solid State Ionics* **1999**, *125*, 1.

[7] Q. Bai, Y. Zhu, X. He, E. Wachsman, Y. Mo, *Ionics* **2017**, 1.

[8] S. P. Ong, Y. Mo, W. D. Richards, L. Miara, H. S. Lee, G. Ceder, *Energy & Environmental Science* **2013**, *6*, 148.

[9] L. J. Miara, S. P. Ong, Y. Mo, W. D. Richards, Y. Park, J.-M. Lee, H. S. Lee, G. Ceder, *Chemistry of Materials* **2013**, *25*, 3048.

[10] X. Qi, Y. S. Lin, *Solid State Ionics* **2000**, *130*, 149.

[11] Z. Deng, B. Radhakrishnan, S. P. Ong, *Chemistry of Materials* **2015**, *27*, 3749.

[12] Z. Lu, C. Chen, Z. M. Baiyee, X. Chen, C. Niu, F. Ciucci, *Physical Chemistry Chemical Physics* **2015**, *17*, 32547.

[13] H. L. Tuller, S. R. Bishop, *Annual Review of Materials Research* **2011**, *41*, 369.

[14] H. J. Queisser, E. E. Haller, *Science* **1998**, *281*, 945.

[15] J. Li, H. Yoon, E. D. Wachsman, *Journal of Membrane Science* **2011**, *381*, 126.

[16] M. Swift, C. G. Van de Walle, *The Journal of Physical Chemistry C* **2016**, *120*, 9562.

[17] A. Urban, D.-H. Seo, G. Ceder, *npj Comput. Mater.* **2016**, *2*, 16002.

[18] A. Lakki, R. Herzog, M. Weller, H. Schubert, C. Reetz, O. Görke, M. Kilo, G. Borchardt, *Journal of the European Ceramic Society* **2000**, *20*, 285.

[19] S. Xiong, X. He, A. Han, Z. Liu, Z. Ren, B. McElhenny, A. M. Nolan, S. Chen, Y. Mo, H. Chen, *Advanced Energy Materials* **2019**, *9*, 1803821.

[20] J. Rogelj, M. Den Elzen, N. Höhne, T. Fransen, H. Fekete, H. Winkler, R. Schaeffer, F. Sha, K. Riahi, M. Meinshausen, *Nature* **2016**, *534*, 631.

[21] K.-D. Kreuer, *Annual Review of Materials Research* **2003**, *33*, 333.

[22] T.-k. Oh, H. Yoon, E. D. Wachsman, *Solid State Ionics* **2009**, *180*, 1233.

[23] S. J. Song, T. H. Lee, E. D. Wachsman, L. Chen, S. E. Dorris, U. Balachandran, *Journal of the Electrochemical Society* **2005**, *152*, J125.

[24] X. Qi, Y. S. Lin, *Solid State Ionics* **2000**, *130*, 149.

[25] S. J. Song, E. D. Wachsman, J. Rhodes, S. E. Dorris, U. Balachandran, *Solid State Ionics* **2003**, *164*, 107.

[26] S. J. Song, E. D. Wachsman, J. Rhodes, S. E. Dorris, U. Balachandran, *Solid State Ionics* **2004**, *167*, 99.

[27] S. J. Song, T. H. Lee, E. D. Wachsman, L. Chen, S. E. Dorris, U. Balachandran, *Journal of the Electrochemical Society* **2005**, *152*, J125.
[28] T. Oh, H. Yoon, E. D. Wachsman, *Solid State Ionics* **2009**, *180*, 1233.
[29] J. Li, H. Yoon, E. D. Wachsman, *Journal of Membrane Science* **2011**, *381*, 126.
[30] S. P. Ong, Y. Mo, G. Ceder, *Physical Review B* **2012**, *85*, 081105.
[31] A. Janotti, J. B. Varley, M. Choi, C. G. Van de Walle, *Physical Review B* **2014**, *90*, 085202.
[32] S. P. Ong, V. L. Chevrier, G. Ceder, *Physical Review B* **2011**, *83*, 075112.
[33] X. He, Y. Mo, *Physical Chemistry Chemical Physics* **2015**, *17*, 18035.
[34] A. S. Hallsworth, J. A. Weatherell, D. Deutsch, *Analytical chemistry* **1976**, *48*, 1660.
[35] F. W. Poulsen, *Solid State Ionics* **2001**, *145*, 387.
[36] A. F. Andresen, A. J. Maeland, D. Slotfeldt-Ellingsen, *Journal of Solid State Chemistry* **1977**, *20*, 93.
[37] M. C. Verbraeken, C. Cheung, E. Suard, J. T. S. Irvine, *Nature materials* **2015**, *14*, 95.
[38] M. A. Hayward, E. J. Cussen, J. B. Claridge, M. Bieringer, M. J. Rosseinsky, C. J. Kiely, S. J. Blundell, I. M. Marshall, F. L. Pratt, *Science* **2002**, *295*, 1882.
[39] X. Liu, T. S. Bjørheim, R. Haugsrud, *Journal of Materials Chemistry A* **2017**, *5*, 1050.
[40] A. Watanabe, G. Kobayashi, N. Matsui, M. Yonemura, A. Kubota, K. Suzuki, M. Hirayama, R. Kanno, *Electrochemistry* **2017**, *85*, 88.
[41] A. M. Nolan, Y. Zhu, X. He, Q. Bai, Y. Mo, *Joule* **2018**.
[42] Y. Mo, S. P. Ong, G. Ceder, *Chemistry of Materials* **2011**, *24*, 15.
[43] X. He, Y. Zhu, Y. Mo, *Nature communications* **2017**, *8*, 15893.
[44] Z. Xu, R. Chen, H. Zhu, *Journal of Materials Chemistry A* **2019**.
[45] Y. Seino, T. Ota, K. Takada, A. Hayashi, M. Tatsumisago, *Energy & Environmental Science* **2014**, *7*, 627.
[46] N. Kamaya, K. Homma, Y. Yamakawa, M. Hirayama, R. Kanno, M. Yonemura, T. Kamiyama, Y. Kato, S. Hama, K. Kawamoto, *Nature materials* **2011**, *10*, 682.
[47] V. Thangadurai, S. Narayanan, D. Pinzaru, *Chemical Society Reviews* **2014**, *43*, 4714.
[48] R. Murugan, V. Thangadurai, W. Weppner, *Angewandte Chemie International Edition* **2007**, *46*, 7778.
[49] H. Aono, E. Sugimoto, Y. Sadaoka, N. Imanaka, G.-y. Adachi, *Solid State Ionics* **1990**, *40*, 38.
[50] Y. Zhu, X. He, Y. Mo, *ACS applied materials & interfaces* **2015**, *7*, 23685.
[51] Y. Zhu, X. He, Y. Mo, *Advanced Science* **2017**, *4*, 1600517.
[52] D. Chang, K. Oh, S. J. Kim, K. Kang, *Chemistry of Materials* **2018**, *30*, 8764.
[53] S. Wang, Q. Bai, A. M. Nolan, Y. Liu, S. Gong, Q. Sun, Y. Mo, *Angewandte Chemie International Edition* **2019**.
[54] R. Kanno, Y. Takeda, O. Yamamoto, *Materials Research Bulletin* **1981**, *16*, 999.

[55] K. Kaup, F. Lalère, A. Huq, A. Shyamsunder, T. Adermann, P. Hartmann, L. F. Nazar, *Chemistry of Materials* **2018**, *30*, 592.
[56] P. E. Blöchl, *Physical review B* **1994**, *50*, 17953.
[57] G. Kresse, J. Furthmüller, *Physical review B* **1996**, *54*, 11169.
[58] J. P. Perdew, K. Burke, M. Ernzerhof, *Physical review letters* **1996**, *77*, 3865.
[59] A. Jain, G. Hautier, C. J. Moore, S. P. Ong, C. C. Fischer, T. Mueller, K. A. Persson, G. Ceder, *Computational Materials Science* **2011**, *50*, 2295.
[60] J. Heyd, G. E. Scuseria, M. Ernzerhof, *The Journal of chemical physics* **2003**, *118*, 8207.
[61] J. Paier, M. Marsman, K. Hummer, G. Kresse, I. C. Gerber, J. G. Ángyán, *The Journal of chemical physics* **2006**, *124*, 154709.
[62] A. Togo, I. Tanaka, *Scripta Materialia* **2015**, *108*, 1.
[63] J. P. Perdew, A. Ruzsinszky, G. I. Csonka, O. A. Vydrov, G. E. Scuseria, L. A. Constantin, X. Zhou, K. Burke, *Physical review letters* **2008**, *100*, 136406.
[64] S. P. Ong, L. Wang, B. Kang, G. Ceder, *Chemistry of Materials* **2008**, *20*, 1798.
[65] G. Mills, H. Jónsson, G. K. Schenter, *Surf. Sci.* **1995**, *324*, 305.
[66] Z. Deng, Y. Mo, S. P. Ong, *NPG Asia Mater.* **2016**, *8*, e254.
[67] G. Henkelman, B. P. Uberuaga, H. Jónsson, *J. Chem. Phys.* **2000**, *113*, 9901.
[68] X. He, Y. Zhu, Y. Mo, *Nat. Commun.* **2017**, *8*, 15893.
[69] A. Van der Ven, G. Ceder, M. Asta, P. D. Tepesch, ***Phys. Rev. B*** **2001**, *64*, 184307.
[70] Y. Mo, S. P. Ong, G. Ceder, *Chem. Mater.* **2014**, *26*, 5208.
[71] S. P. Ong, V. L. Chevrier, G. Hautier, A. Jain, C. Moore, S. Kim, X. Ma, G. Ceder, *Energy Environ. Sci.* **2011**, *4*, 3680.
[72] M. S. Islam, C. A. J. Fisher, *Chem. Soc. Rev.* **2014**, *43*, 185.
[73] R. Tripathi, S. M. Wood, M. S. Islam, L. F. Nazar, *Energy Environ. Sci.* **2013**, *6*, 2257.
[74] C. Zheng, B. Radhakrishnan, I.-H. Chu, Z. Wang, S. P. Ong, *Phys. Rev. Appl.* **2017**, *7*, 064003.
[75] Y. Mo, S. P. Ong, G. Ceder, *Chem. Mater.* **2011**, *24*, 15.
[76] S. P. Ong, Y. Mo, W. D. Richards, L. Miara, H. S. Lee, G. Ceder, *Energy Environ. Sci.* **2013**, *6*, 148.
[77] M. G. Schultz, T. Diehl, G. P. Brasseur, W. Zittel, *Science* **2003**, *302*, 624.
[78] N. Taniguchi, K. Hatoh, J. Niikura, T. Gamo, H. Iwahara, *Solid State Ionics* **1992**, *53*, 998.
[79] T. Schober, F. Krug, W. Schilling, *Solid State Ionics* **1997**, *97*, 369.
[80] T. Yajima, K. Koide, H. Takai, N. Fukatsu, H. Iwahara, *Solid State Ionics* **1995**, *79*, 333.
[81] S. Hamakawa, T. Hibino, H. Iwahara, *Journal of the Electrochemical Society* **1994**, *141*, 1720.
[82] G. Marnellos, O. Sanopoulou, A. Rizou, M. Stoukides, *Solid State Ionics* **1997**, *97*, 375.
[83] T. Norby, *Solid State Ionics* **1999**, *125*, 1.
[84] J. W. Phair, S. P. S. Badwal, *Ionics* **2006**, *12*, 103.
[85] K. D. Kreuer, *Annual Review of Materials Research* **2003**, *33*, 333.

[86] E. Fabbri, D. Pergolesi, E. Traversa, *Chemical Society Reviews* **2010**, *39*, 4355.
[87] S.-J. Song, H.-S. Park, *Journal of Materials Science* **2007**, *42*, 6177.
[88] S. Shin, H. H. Huang, M. Ishigame, H. Iwahara, *Solid State Ionics* **1990**, *40*, 910.
[89] H. Iwahara, T. Esaka, H. Uchida, N. Maeda, *Solid State Ionics* **1981**, *3*, 359.
[90] C. Wagner, *Progress in Solid State Chemistry* **1975**, *10*, 3.
[91] I. Kosacki, H. L. Tuller, *Solid State Ionics* **1995**, *80*, 223.
[92] S. J. Song, E. D. Wachsman, S. E. Dorris, U. Balachandran, *Journal of the Electrochemical Society* **2003**, *150*, A1484.
[93] T. Maxisch, F. Zhou, G. Ceder, *Physical Review B* **2006**, *73*, 104301.
[94] J. P. Holdren, *National Science and Technology Council OSTP. Washington, USA* **2011**.
[95] D. Morgan, G. Ceder, S. Curtarolo, *Measurement Science and Technology* **2004**, *16*, 296.
[96] S. Curtarolo, G. L. W. Hart, M. B. Nardelli, N. Mingo, S. Sanvito, O. Levy, *Nature Materials* **2013**, *12*, 191.
[97] S. P. Ong, Y. Mo, W. D. Richards, L. Miara, H. S. Lee, G. Ceder, *Energy & Environmental Science* **2013**, *6*, 148.
[98] X. He, Y. Mo, *Physical Chemistry Chemical Physics* **2015**, *17*, 18035.
[99] Z. Wang, I.-H. Chu, F. Zhou, S. P. Ong, *Chemistry of Materials* **2016**, *28*, 4024.
[100] C. Pupp, K. A. Gingerich, *The Journal of Chemical Physics* **1971**, *54*, 3380.
[101] K. Sekizawa, M. Kitagawa, Y. Takano, *Journal of Magnetism and Magnetic Materials* **1998**, *177*, 541.
[102] K. Makita, O. Yamashita, *Applied Physics Letters* **1999**, *74*, 2056.
[103] S. Primdahl, J. R. Hansen, L. Grahl-Madsen, P. H. Larsen, *Journal of the Electrochemical Society* **2001**, *148*, A74.
[104] J. Heyd, G. E. Scuseria, M. Ernzerhof, *The Journal of Chemical Physics* **2006**, *124*, 219906.
[105] A. I. Liechtenstein, V. I. Anisimov, J. Zaanen, *Physical Review B* **1995**, *52*, R5467.
[106] V. L. Chevrier, S. P. Ong, R. Armiento, M. K. Y. Chan, G. Ceder, *Physical Review B* **2010**, *82*, 075122.
[107] D.-H. Seo, J. Lee, A. Urban, R. Malik, S. Kang, G. Ceder, *Nature Chemistry* **2016**, *8*, 692.
[108] D. A. Kitchaev, H. Peng, Y. Liu, J. Sun, J. P. Perdew, G. Ceder, *Physical Review B* **2016**, *93*, 045132.
[109] S. P. Ong, V. L. Chevrier, G. Ceder, *Physical Review B* **2011**, *83*, 075112.
[110] M. Swift, A. Janotti, C. G. Van de Walle, *Physical Review B* **2015**, *92*, 214114.
[111] S. P. Ong, W. D. Richards, A. Jain, G. Hautier, M. Kocher, S. Cholia, D. Gunter, V. L. Chevrier, K. A. Persson, G. Ceder, *Computational Materials Science* **2013**, *68*, 314.
[112] D. M. Ramo, A. L. Shluger, J. L. Gavartin, G. Bersuker, *Physical Review Letters* **2007**, *99*, 155504.

[113] B. J. Morgan, D. O. Scanlon, G. W. Watson, *Journal of Materials Chemistry* **2009**, *19*, 5175.
[114] K. Biswas, M.-H. Du, *Physical Review B* **2012**, *86*, 014102.
[115] A. Janotti, J. B. Varley, M. Choi, C. G. Van de Walle, *Physical Review B* **2014**, *90*, 085202.
[116] J. Hermet, F. Bottin, G. Dezanneau, G. Geneste, *Physical Review B* **2012**, *85*, 205137.
[117] C. Freysoldt, B. Grabowski, T. Hickel, J. Neugebauer, G. Kresse, A. Janotti, C. G. Van de Walle, *Reviews of Modern Physics* **2014**, *86*, 253.
[118] H.-P. Komsa, T. T. Rantala, A. Pasquarello, *Physical Review B* **2012**, *86*, 045112.
[119] G. C. Mather, S. García-Martín, D. Benne, C. Ritter, U. Amador, *Journal of Materials Chemistry* **2011**, *21*, 5764.
[120] A. F. Kohan, G. Ceder, D. Morgan, C. G. Van de Walle, *Physical Review B* **2000**, *61*, 15019.
[121] A. Janotti, C. G. Van de Walle, *Physical Review B* **2007**, *76*, 165202.
[122] M. D. Radin, D. J. Siegel, *Energy & Environmental Science* **2013**, *6*, 2370.
[123] J. Ranløv, K. Nielsen, *Journal of Materials Chemistry* **1994**, *4*, 867.
[124] F. Goubin, X. Rocquefelte, M. H. Whangbo, Y. Montardi, R. Brec, S. Jobic, *Chemistry of Materials* **2004**, *16*, 662.
[125] N. Sata, H. Yugami, Y. Akiyama, T. Hattori, S. Yamaguchi, M. Ishigame, *Solid State Ionics* **1999**, *121*, 321.
[126] A. Jain, S. P. Ong, G. Hautier, W. Chen, W. D. Richards, S. Dacek, S. Cholia, D. Gunter, D. Skinner, G. Ceder, *APL Materials* **2013**, *1*, 011002.
[127] S. P. Ong, L. Wang, B. Kang, G. Ceder, *Chemistry of Materials* **2008**, *20*, 1798.
[128] H. Uchida, N. Maeda, H. Iwahara, *Solid State Ionics* **1983**, *11*, 117.
[129] E. Possenriede, B. Hellermann, O. F. Schirmer, *Solid State Communications* **1988**, *65*, 31.
[130] A. L. Shluger, A. M. Stoneham, *Journal of Physics: Condensed Matter* **1993**, *5*, 3049.
[131] E. A. Kotomin, R. I. Eglitis, A. V. Postnikov, G. Borstel, N. E. Christensen, *Physical Review B* **1999**, *60*, 1.
[132] X. Liang, in *Chemical Engineering*, Vol. M.S., University of Maryland, College Park, Ann Arbor 2015, 111.
[133] C. Chakkaravarthy, A. K. A. Waheed, H. V. K. Udupa, *Journal of Power sources* **1981**, *6*, 203.
[134] X. Zhao, L. Ma, X. Shen, *Journal of Materials Chemistry* **2012**, *22*, 277.
[135] V. Palomares, P. Serras, I. Villaluenga, K. B. Hueso, J. Carretero-González, T. Rojo, *Energy & Environmental Science* **2012**, *5*, 5884.
[136] Ø. S. Fjellvåg, J. Armstrong, W. A. Sławiński, A. O. Sjåstad, *Inorganic chemistry* **2017**, *56*, 11123.
[137] F. W. Poulsen, *Solid State Ionics* **2001**, *145*, 387.
[138] H. Iwahara, H. Uchida, K. Ono, K. Ogaki, *Journal of the Electrochemical Society* **1988**, *135*, 529.
[139] T. Norby, Y. Larring, *Solid State Ionics* **2000**, *136*, 139.

[140] M. C. Verbraeken, C. Cheung, E. Suard, J. T. S. Irvine, *Nature materials* **2015**, *14*, 95.
[141] Y. Zhang, M. C. Verbraeken, C. Tassel, H. Kageyama, in *Handbook of Solid State Chemistry*, (Eds: R. Dronskowski, S. Kikkawa, A. Stein), Wiley-VCH, German 2017, 477.
[142] B. Malaman, J. F. Brice, *Journal of Solid State Chemistry* **1984**, *53*, 44.
[143] C. A. Bridges, F. Fernandez‐Alonso, J. P. Goff, M. J. Rosseinsky, *Advanced materials* **2006**, *18*, 3304.
[144] T. Sakaguchi, Y. Kobayashi, T. Yajima, M. Ohkura, C. d. Tassel, F. Takeiri, S. Mitsuoka, H. Ohkubo, T. Yamamoto, J. e. Kim, *Inorganic chemistry* **2012**, *51*, 11371.
[145] X. Liu, T. S. Bjørheim, R. Haugsrud, *RSC Advances* **2016**, *6*, 9822.
[146] X. Liu, T. S. Bjørheim, R. Haugsrud, *Journal of Materials Chemistry A* **2017**.
[147] Y. Kobayashi, O. J. Hernandez, T. Sakaguchi, T. Yajima, T. Roisnel, Y. Tsujimoto, M. Morita, Y. Noda, Y. Mogami, A. Kitada, *Nature materials* **2012**, *11*, 507.
[148] S. Steinsvik, Y. Larring, T. Norby, *Solid State Ionics* **2001**, *143*, 103.
[149] T. Yajima, A. Kitada, Y. Kobayashi, T. Sakaguchi, G. Bouilly, S. Kasahara, T. Terashima, M. Takano, H. Kageyama, *Journal of the American Chemical Society* **2012**, *134*, 8782.
[150] J. Zhang, G. Gou, B. Pan, *The Journal of Physical Chemistry C* **2014**, *118*, 17254.
[151] G. Bouilly, T. Yajima, T. Terashima, W. Yoshimune, K. Nakano, C. d. Tassel, Y. Kususe, K. Fujita, K. Tanaka, T. Yamamoto, *Chemistry of Materials* **2015**, *27*, 6354.
[152] X. Gonze, D. C. Allan, M. P. Teter, *Physical Review Letters* **1992**, *68*, 3603.
[153] R. Resta, *Ferroelectrics* **1992**, *136*, 51.
[154] K. Refson, P. R. Tulip, S. J. Clark, *Physical Review B* **2006**, *73*, 155114.
[155] P. P. Ewald, *Annalen der Physik* **1921**, *369*, 253.
[156] S. Nosé, *The Journal of chemical physics* **1984**, *81*, 511.
[157] W. G. Hoover, *Physical review A* **1985**, *31*, 1695.
[158] X. He, Y. Zhu, A. Epstein, Y. Mo, *NPJ Computational Materials* **2018**, Accepted.
[159] A. Marcolongo, N. Marzari, *Physical Review Materials* **2017**, *1*, 025402.
[160] G. Henkelman, H. Jónsson, *The Journal of chemical physics* **2000**, *113*, 9978.
[161] G. Henkelman, B. P. Uberuaga, H. Jónsson, *The Journal of chemical physics* **2000**, *113*, 9901.
[162] G. Hautier, C. Fischer, V. Ehrlacher, A. Jain, G. Ceder, *Inorganic chemistry* **2010**, *50*, 656.
[163] G. Henkelman, A. Arnaldsson, H. Jónsson, *Computational Materials Science* **2006**, *36*, 354.
[164] W. Tang, E. Sanville, G. Henkelman, *Journal of Physics: Condensed Matter* **2009**, *21*, 084204.
[165] S. Ping Ong, L. Wang, B. Kang, G. Ceder, *Chemistry of Materials* **2008**, *20*, 1798.

[166] Y. Wang, W. D. Richards, S. P. Ong, L. J. Miara, J. C. Kim, Y. Mo, G. Ceder, *Nature materials* **2015**, *14*, 1026.
[167] W. D. Richards, Y. Wang, L. J. Miara, J. C. Kim, G. Ceder, *Energy & Environmental Science* **2016**, *9*, 3272.
[168] W. Scheld, G. Wehrum, R. Hoppe, *Zeitschrift fuer anorganische und allgemeine Chemie* **1993**, *619*, 337.
[169] V. A. Carlson, A. M. Stacy, *Journal of Solid State Chemistry* **1992**, *96*, 332.
[170] Z. Deng, Z. Wang, I.-H. Chu, J. Luo, S. P. Ong, *Journal of The Electrochemical Society* **2016**, *163*, A67.
[171] Y. Le Page, P. Saxe, *Physical Review B* **2002**, *65*, 104104.
[172] T. F. Willems, C. H. Rycroft, M. Kazi, J. C. Meza, M. Haranczyk, *Microporous and Mesoporous Materials* **2012**, *149*, 134.
[173] R. L. Martin, B. Smit, M. Haranczyk, *Journal of chemical information and modeling* **2011**, *52*, 308.
[174] X. He, Y. Zhu, A. Epstein, Y. Mo, *npj Computational Materials* **2018**, *4*, 18.
[175] L. Pauling, *Journal of the american chemical society* **1929**, *51*, 1010.
[176] R. D. Shannon, *Acta crystallographica section A: crystal physics, diffraction, theoretical and general crystallography* **1976**, *32*, 751.
[177] M. Born, "On the stability of crystal lattices. I", presented at *Mathematical Proceedings of the Cambridge Philosophical Society*, 1940.
[178] F. Mouhat, F.-X. Coudert, *Physical review B* **2014**, *90*, 224104.
[179] S. F. Pugh, *The London, Edinburgh, and Dublin Philosophical Magazine and Journal of Science* **1954**, *45*, 823.
[180] R. Hill, *Proceedings of the Physical Society. Section A* **1952**, *65*, 349.
[181] T. Thompson, S. Yu, L. Williams, R. D. Schmidt, R. Garcia-Mendez, J. Wolfenstine, J. L. Allen, E. Kioupakis, D. J. Siegel, J. Sakamoto, *ACS Energy Letters* **2017**, *2*, 462.
[182] Y. Zhu, X. He, Y. Mo, *Journal of Materials Chemistry A* **2016**, *4*, 3253.
[183] T. Asano, A. Sakai, S. Ouchi, M. Sakaida, A. Miyazaki, S. Hasegawa, *Advanced Materials* **2018**, *30*, 1803075.
[184] L. Van Hove, *Physical Review* **1954**, *95*, 249.
[185] J.-L. Zhao, W. Zhang, X.-M. Li, J.-W. Feng, X. Shi, *Journal of Physics: Condensed Matter* **2006**, *18*, 1495.